

SURFACE LOCAL FIELD POTENTIALS FOR
BRAIN-COMPUTER INTERFACES

by

Spencer Sterling Kellis

A dissertation submitted to the faculty of
The University of Utah
in partial fulfillment of the requirements for the degree of

Doctor of Philosophy

Department of Electrical and Computer Engineering
The University of Utah

May 2012

Copyright © Spencer Sterling Kellis 2012

All Rights Reserved

ABSTRACT

This dissertation describes the use of cortical surface potentials, recorded with dense grids of microelectrodes, for brain-computer interfaces (BCIs). The work presented herein is an in-depth treatment of a broad and interdisciplinary topic, covering issues from electronics to electrodes, signals, and applications.

Within the scope of this dissertation are several significant contributions. First, this work was the first to demonstrate that speech and arm movements could be decoded from surface local field potentials (LFPs) recorded in human subjects. Using surface LFPs recorded over face-motor cortex and Wernicke's area, 150 trials comprising vocalized articulations of ten different words were classified on a trial-by-trial basis with 86% accuracy. Surface LFPs recorded over the hand and arm area of motor cortex were used to decode continuous hand movements, with correlation of 0.54 between the actual and predicted position over 70 seconds of movement.

Second, this work is the first to make a detailed comparison of cortical field potentials recorded intracortically with microelectrodes and at the cortical surface with both micro- and macroelectrodes. Whereas coherence in macroelectrocorticography (ECoG) decayed to half its maximum at 5.1 mm separation in high frequencies, spatial constants of micro-ECoG signals were 530-700 μm —much closer to the 110-160 μm calculated for intracortical field potentials than to the macro-ECoG. These findings confirm that cortical surface potentials contain millimeter-scale dynamics. Moreover, these fine spatiotemporal features were important for the performance of speech and arm movement decoding.

In addition to contributions in the areas of signals and applications, this dissertation includes a full characterization of the microelectrodes as well as collaborative work in which

a custom, low-power microcontroller, with features optimized for biomedical implants, was taped out, fabricated in 65 nm CMOS technology, and tested. A new instruction was implemented in this microcontroller which reduced energy consumption when moving large amounts of data into memory by as much as 44%.

This dissertation represents a comprehensive investigation of surface LFPs as an interfacing medium between man and machine. The nature of this work, in both the breadth of topics and depth of interdisciplinary effort, demonstrates an important and developing branch of engineering.

To my wife, Emily, and to parents, family, friends, mentors,
and colleagues who have been with me all along the way.

TABLE OF CONTENTS

ABSTRACT	iii
LIST OF TABLES	viii
LIST OF FIGURES	ix
ACKNOWLEDGMENTS	xii
Chapters	
1 INTRODUCTION	1
Electronics for BCIs	2
Overview of signals for BCIs	5
Surface potentials for BCIs	8
Conclusion	9
References.....	11
2 SELECTED TECHNIQUES FOR LOW-POWER DIGITAL VLSI	20
WIMS microcontroller	21
Block transfer instructions	22
Characterizing energy use	23
Methods.....	24
Results.....	28
Discussion.....	33
Conclusion.....	34
References.....	35
3 CORTICAL FIELD POTENTIALS	37
Signals and dynamics	38
Electrodes	40
Methods.....	42
Results.....	49
Discussion.....	71
Conclusion.....	76
References.....	77

4	CHARACTERIZATION OF MICRO-ECOG ELECTRODES	82
	Methods.....	82
	Results.....	85
	Discussion.....	88
	Conclusion.....	92
	References.....	92
5	DECODING MOTOR ACTIVITY USING LOCAL FIELD POTENTIALS RECORDED FROM THE CORTICAL SURFACE	94
	Methods.....	95
	Results.....	103
	Discussion.....	116
	Conclusion.....	118
	References.....	118
6	DECODING SPOKEN WORDS USING LOCAL FIELD POTENTIALS RECORDED FROM THE CORTICAL SURFACE	120
	Methods.....	121
	Results.....	127
	Discussion.....	135
	Conclusion.....	142
	References.....	142
7	CONCLUSION	146
	Challenges and future work: subjects and data	148
	Challenges and future work: electronics	149
	Challenges and future work: electrodes	151
	Challenges and future work: signal processing	151
	Conclusion	153
	References	154

LIST OF TABLES

Table		Page
1.1	Comparison of VLSI implementations of BCIs	4
2.1	Energy of each WIMS instruction group	30
3.1	Listing of subjects and grid types	43
3.2	Finite-duration at half maximum (FDHM)	52
3.3	Comparing the initial slope of correlation versus distance with and without common average re-referencing	68
4.1	Model parameters fit to measured EIS data	87
5.1	Level of chance for all kinematic variables, for each patient	111
6.1	Listing of words used and numbers of recorded and stereotyped trials	123

LIST OF FIGURES

Figure	Page
2.1	Sample program loop in assembly code26
2.2	WIMS microcontroller photograph, layout, and power consumption28
2.3	Comparison of energy used by block-transfer and load/store instructions32
3.1	The devices used to record neural activity for this study41
3.2	Locations of the electrode grids44
3.3	Correlation functions estimated for each grid type50
3.4	Correlation over space and time for SM2, SM3, SM4, and UA251
3.5	Behavior of FDHM over time and space53
3.6	Behavior of FDHM over time and space54
3.7	Correlation vs. distance for each grid type56
3.8	Correlations between electrodes shown spatially58
3.9	Correlations between electrodes shown spatially59
3.10	Correlation vs. distance for channels along angled axes62
3.11	Coherence functions estimated for each grid type63
3.12	Coherence over space and frequency for SM2, SM3, SM4, and UA2 grids65
3.13	Half-height decay (HHD) of the coherence (in millimeters)67
3.14	Coherence between each channel and all other channels in the same grid68
3.15	Correlation vs. distance for data re-referenced to the common average69
3.16	Coherence for UA1 and UA2 compared for raw and CAR data70
4.1	Nonpenetrating microwire devices83
4.2	Equivalent circuit used to fit the measured EIS results84

4.3	Resistor mesh modeling electrode and cortical tissue	85
4.4	Measured electrochemical impedance spectroscopy results	86
4.5	Correlations calculated for simulated data	88
5.1	Implant pictures from Patients 1 and 2	95
5.2	Trial detection and filtering for a portion of recorded motor tasks including continuous movement, velocity profiles, and filtering of horizontal and vertical components	97
5.3	Gamma band (30–80 Hz) pairwise cross-correlations between each nonpenetrating microwire and all other microwires within an array.....	104
5.4	Spectrograms from a single nonpenetrating microwire for each patient demonstrating increased power in the gamma band during the planning phase for movement in the contralateral versus the ipsilateral direction	106
5.5	Spectrograms from all nonpenetrating microwires in P1 demonstrating increased power in the gamma band during the planning phase for movement in the contralateral versus the ipsilateral direction	107
5.6	Spectrograms from all nonpenetrating microwires in P2 demonstrating increased power in the gamma band during the planning phase for movement in the contralateral versus the ipsilateral direction	108
5.7	Plots showing, for each nonpenetrating microwire channel in each patient, the percent change in average gamma-band power during planning for movement in the contralateral direction over movement in the ipsilateral direction	110
5.8	Sample output of the Kalman filter for patients P1 and P2	112
5.9	Summary of performance of the Kalman filter for both P1 and P2	113
5.10	Performance of Kalman filter as a function of frequency for P1 and P2	115
6.1	The micro-ECoG grids and surgical placement	122
6.2	Using frequency-domain structure to decode simultaneously from multiple channels	124
6.3	Using time- and frequency-domain structure to decode simultaneously from multiple channels	126
6.4	Raw data, spectrogram, and mean power during conversation and task	128

6.5	Raw data, spectrogram, and mean power during conversation and task on day 2	129
6.6	Raw data, spectrogram, and mean power during conversation and task on day 3	130
6.7	Raw data, spectrogram, and mean power during conversation and task on day 4	131
6.8	Classification accuracy for combinations of two through ten words	132
6.9	Decodability matrices for FMC and Wernicke's area	133
6.10	Topography of performance by individual electrode and word	134
6.11	Comparing frequency and voltage as features in the classification	135
6.12	Performance of the speech classification as a function of frequency	136
6.13	Performance of the speech classification as a function of time index	137

ACKNOWLEDGMENTS

I pause here to reflect on the many kind and good people who have shaped my path. These include teachers from grade school and college like B. Good, D. Taczanowsky, H. Fischer, D. Monson, and A. Hawkins, each of whom gave me much more than simple information: a deep appreciation for the beauty in their realm of knowledge, whether music, English, calculus, or engineering, and for the process of learning and growing.

In graduate school, V. J. Mathews challenged me substantially then followed through to teach me as I made the effort to learn. The concepts he taught me are a foundation of my research. P. House contributed significantly to my first journal paper, an inflection point in my career, and has been a source of thoughtful and valuable guidance. B. Greger gave me his unbending trust and confidence, and inspired me toward excellence. He has become a wonderful friend whose mentoring, support, and encouragement made all the difference.

I have found great joy in friendships with fellow students and colleagues: Nathaniel, Bennion, Amlan, Rob, Jeff, Elliot, Sara, Tyler, Josh, Kai, Larry and others.

To my advisor, Richard Brown, whom I hold in the highest regard for his integrity and kindness: I will always be grateful that you found me, gave me wide latitude to pursue my interests, and mentored me with grace and wisdom. You perhaps understand even better than I the significance of what you've done for me. Thank you.

To my wife Emily: thank you for your support and love. Even on your most difficult days, you put me first. To my parents: thank you for our heritage and for valuing education.

Though I have listed only a few names, many have played roles large and small. In a sense, I represent the summed contributions of all these people; and so this dissertation and the degree it represents are evidence of the value, substance, and truth in their gifts.

CHAPTER 1

INTRODUCTION

Brain-computer interfaces (BCI) blend neuroscience and engineering to physically interface with brain tissue, process acquired brain activity, and control an external device. These topics comprise a rapidly expanding field of research as technological advances, particularly in the areas of electrodes and electronics, have brought contemporary research efforts ever closer to a chronic, practically useful, fully implantable BCI. Yet, significant challenges remain as engineering and neuroscience continue to evolve, and deep collaborations between these traditionally separate fields are more important now than ever before. Thus, it is in both breadth (electronics, electrodes, and signals) and depth (strong interdisciplinary collaborations) that this dissertation represents a comprehensive treatment of BCI topics. The significant contribution of this work is that it is the first in-depth investigation of cortical surface potentials recorded at the millimeter scale by nonpenetrating microwires for BCI applications. No less significant, however, is that the breadth of the work and the close collaborations represented herein demonstrate an important and developing branch of engineering applied to innovate in new fields.

Among the many choices which must be made in the design of BCI systems, selecting the appropriate signal to acquire represents perhaps the most central choice, and governs all other aspects of the system design. Within the spectrum of signal choices, electrical potentials recorded at the cortical surface (intracranially, but epicortically) are attractive because they may be recorded without penetrating the cortex but still demonstrate good signal fidelity due to their close approximation to the underlying neural sources.

Small, dense grids of nonpenetrating microwires were conceived in an effort to capture more detailed information from the cortical surface for applications like BCIs. It is these nonpenetrating microelectrodes, and the surface local field potentials (LFPs) they record, that form the foundation of this dissertation. Several chapters will be dedicated to exploring fundamental properties of surface LFPs, characterizing the microelectrodes used to record surface LFPs, and developing signal processing algorithms to classify and decode activity from surface LFPs.

An additional and important aspect of BCI research is the design of integrated circuits which will make possible chronically implantable, wireless BCI systems. Several techniques for low-power, high-bandwidth digital processing were explored in this dissertation in the context of the Wireless Integrated Microsystems (WIMS) microcontroller, a custom 16-bit system with three pipeline stages, 24-bit address space, 32KB of on-chip SRAM, and a variety of external interfaces. The WIMS microcontroller is a complex digital system well tested in both simulation and implementation, similar to the type of controller that may be needed in an embedded BCI for system-level coordination or low-level computation. One chapter of this dissertation will be dedicated to these techniques for digital electronics.

The remainder of this chapter will describe relevant concepts and prior work in the field of BCI research, and briefly introduce the work which will be described comprehensively in later chapters. Because the topics in electronics which are addressed in this dissertation are somewhat disjoint to the remainder of the work, they will be discussed separately and first. Afterward, electrodes, signals, and algorithms for BCI systems will be discussed. The subsequent chapters of this dissertation will be laid out in a similar order.

Electronics for BCIs

Typical BCI research systems directly tether intracranial recording electrodes to a suite of electronics for amplification and digitization, effectively confining the patient to

a hospital bed in an intensive care unit. These systems perform the function of a BCI but they are physically large, consume large amounts of power, and leave patients vulnerable to infection. A practically useful BCI should be adaptable to personal transportation and therefore small and power efficient. Safe, chronic operation precludes the use of a physical transcutaneous link between electrodes and external hardware to mitigate the inherent risk of infection in such connections. The advantages of VLSI technology could help to overcome many of these limitations, since a single, physically small, power efficient system could be designed to perform digitization, signal analysis, and wireless transmission.

BCIs are an example of a low-power embedded system designed to sense an environment. This class of systems (e.g., [1-4]) often employs a microcontroller with an analog front end to digitize and process data from a connected sensor, and typically includes capability of periodically transferring processed information to another system. Minimizing power under application-specific performance constraints is fundamental to extending the battery life, and therefore the utility, of these systems. System-level power management in digital systems has been the subject of considerable research [5-10], particularly as the progress of CMOS technology has driven system integration and mobility.

A number of systems incorporating VLSI technology have been designed to record and communicate neural data (Table 1.1) [11-24]. A related class of systems has demonstrated using off-the-shelf components for the same purpose [25-27]. The functional goals of most of these systems are to enable freedom of movement and to avoid permanent transcutaneous wiring in order to reduce the risk of infection during chronic implantation. Practically, most of these systems attempt to record and communicate as many channels of data as possible for as little power as possible. These concurrent design goals are contradictory and lead to a wide variety of system configurations.

Because wireless operation can consume large amounts of power, many systems attempt to reduce the sensed data, either by compression or analysis, to reduce the power consumed during communication. Systems in Table 1.1 which include processing of

Table 1.1 Comparison of VLSI implementations of BCIs. Fields with N/A indicate the data were not available.

First Author	Year	Wireless	Channels	ADC resolution (bits)	Power (mW)	Sampling rate (kS/sec)	Data rate (Mbps)	Power/channel (mW)
Mohseni	2005	Yes	4	N/A	2.2	17.5	N/A	0.55
Olsson	2005	Yes	32	5	5.4	20	0.1	0.17
Aziz	2006	No	256	N/A	6.0	20	N/A	0.02
Cheney	2007	Yes	16	12	143	20	0.25	8.9
Harrison	2007	Yes	100	10	13.5	N/A	0.33	0.14
Perelman	2007	No	12	10	40	40	10.5	3.3
Borton	2009	Yes	16	N/A	12.3	N/A	N/A	0.76
Moo Sung	2009	Yes	128	9	6.0	40	90	0.05
Sodagar	2009	Yes	1	8	14.4	N/A	N/A	14.4
Yeager	2009	Yes	1	10	0.04	N/A	N/A	0.04
Miranda	2010	Yes	32	12	142	30	24	4.44
Greenwald	2011	Yes	16	10	15.84	1	1	0.99
Szuts	2011	Yes	64	6	645	20	N/A	10.1

recorded data have focused exclusively on extracting action potential features from the recorded data. The work of this dissertation diverges fundamentally from the approach of these systems to focus instead on the development of methods for analyzing the continuous field potential data. A few systems have been presented in the literature which take this approach in related fields (see, e.g., [28] for a system for analyzing continuous ECG data).

The electronics of a full BCI system will require mixed-signal design with tight integration from amplification, filtering, and digitization in an analog front end, to digital processing and off-chip communication in the backend. While there are many research opportunities in developing VLSI components for BCIs, the relevant portion of this dissertation has focused on a few specific ideas which could be integrated in future VLSI implementations of neural interfaces. These topics include a set of instructions which more efficiently load and store large amounts of data and a method for characterizing the energy profile of a microcontroller. On their own, these methods are not intended to represent a comprehensive investigation of electronics for BCI systems. However, they are representative of the kinds of studies which will need to be incorporated collectively, with further innovations in mixed-signal circuit designs, to create a system which can process substantial amounts of data within the power budget of a medically implantable device.

Overview of signals for BCIs

Electronics are an important element in BCI systems, but their relevance depends on acquiring useful signals to process. Brain signals may be recorded at a variety of spatiotemporal resolutions, from action potentials of single units to the summed activity of large neuronal populations. Each of these recording scales offers a unique balance of invasiveness and signal fidelity. Because the neural signal at each recording scale is different, information-bearing features and corresponding methods of analysis also differ.

Single-unit action potentials (APs) are discrete events with information encoded in rate, timing, and population statistics. APs constitute a fundamental mechanism of

communication among neurons and therefore represent perhaps the most direct method of observing cortical information processing. These events must be recorded by microelectrodes which penetrate the cortex to rest close to neurons. Firing rates of neurons have been shown to encode direction of arm movement [29-31] and hand trajectories [32], and have been used to perform rapid decoding of continuous motor movements [33-35]. Because of the risks associated with implantation in language centers, few studies have explored the use of penetrating electrodes for speech BCIs. One such study used a glass electrode filled with a neurotrophic growth factor to encourage axonal growth into the electrode [36]. Neural signal recorded from this unique electrode has been used to control a cursor on a computer screen for indirect communication [37], as well as to directly decode the formant frequencies of speech from neuronal activity in the left ventral premotor cortex [38, 39].

In contrast to the almost digital nature of single unit activity, the continuous, aggregate electrical activity of the brain may also be recorded with a variety of invasive and noninvasive methods. The earliest studies of BCIs used noninvasive electroencephalographic (EEG) electrodes to target several specific paradigms of neural signals, including slow cortical potentials (SCP), sensorimotor rhythms (SMR), and the P300 wave [40-46], although the SMR has been reported to be more easily learned than the P300 or SCP [47]. More recently, a two-dimensional movement trajectory decode using SMR was performed to control a cursor in a multitarget selection task, with similar timing, accuracy, and precision as have been previously obtained using depth electrodes [48].

Similar continuous field potentials may be recorded more invasively with electrocorticography (ECoG), which refers to the electrical activity of the brain recorded at the cortical surface. ECoG has been used in the discrimination of finger movements [49-52] and arm movements [53-56], two-dimensional movement trajectories [57, 58], and other motor tasks [59, 60]. Researchers investigating speech BCIs with ECoG electrodes have shown that cortical surface potentials could be used to discriminate between motor and

speech tasks [60] and different phonemes [61]. In particular, event-related spectral power increases in the gamma band (30-80 Hz) [62], more temporally and spatially discrete than desynchronization seen in lower oscillatory bands, may provide spatiotemporal features well correlated to the production of speech [63-65].

Continuous fields may also be recorded from within the cortex by the same electrodes used to capture single unit activity. These signals have been called LFPs because smaller volumes of tissue contribute to the potential formed at the microelectrodes, particularly in comparison to ECoG and EEG electrodes. Many of the findings in ECoG, for example, that gamma-band spectral power increases during motor activity, apply equally to intracortically recorded LFP. In terms of motor-based BCI systems, LFPs have been used in studies of movement intentions [66], reaching and grasping [67-70], and finger movements [71]. LFPs are a widely observed brain signal and have been further studied in the context of many other activities which might have BCI application, such as vision [72, 73], audition [74, 75], attention [76], and pathology [77, 78].

While each of these recording technologies has been used successfully in a brain-computer interface (BCI), invasiveness and performance requirements should drive the selection of the best electrode and neural signal for a particular application. In general, invasiveness should be minimized to the extent that the corresponding signal provides adequate information content for the application. While most BCIs have traditionally used either scalp electrodes or penetrating electrodes, ECoG electrodes have attracted more attention in the last decade for their intermediate balance of signal fidelity and limited invasiveness. Due to their size and spacing, nonpenetrating microelectrodes may provide even better signal fidelity for cortical surface potentials. These new electrodes could provide an even better balance of information content while minimizing invasiveness.

Surface potentials for BCIs

ECoG-based BCIs exploit the proximity of the intracranial electrodes to the cortical surface to provide higher signal-to-noise ratio and improved spatial resolution than their extracranial EEG counterparts [79, 80]. These properties have allowed more in-depth analysis of high gamma modulations during motor tasks, a neural source that has become a foundational element of modern BCI research. However, millimeter-scale electrodes and centimeter-scale interelectrode spacing may be too coarse for neural prosthetic applications [60, 81, 82]. The root of this limitation lies in the size and spacing of clinical ECoG electrodes relative to the underlying cortical structure for information processing. One study of ECoG in human motor-sensory and temporal regions found that correlated gamma modulation was limited to areas covered by only a few (i.e., two) macroelectrodes [82]; similar findings have been noted in at least one other independent study [60]. The local nature of these modulations implies the presence of neuronal assemblies working synchronously to process related types of information needed to generate complex outputs [83-85]. Multiple subpopulations of neurons, possibly engaged in processing distinct stimuli, may contribute to the signal recorded by a single millimeter-scale electrode. Consequently, the rhythmic activity of any one focal area may be obscured in the activity of the several assemblies contributing to the voltage recorded by a single electrode.

Evidence of the spatial discrepancy between macroelectrodes and microscale cortical processing was unavailable prior to the design of the clinical ECoG electrode, and largely irrelevant to the design of electrodes for localizing epileptic foci. However, nonpenetrating microelectrodes terminated at regular, millimeter-scale intervals have been designed to record cortical surface field potentials at a higher spatiotemporal resolution. The tight interelectrode spacing of these microelectrodes closely approximates the local scale of modulations previously shown to correlate with motor activity [56, 81, 82, 86-89]. Similar microelectrode arrays have been shown to support high temporal- and spatial-resolution recordings for BCI-like applications [56, 86].

The signal recorded at the cortical surface consists of the summed contributions of many neuronal sources located in the underlying region of cortex. Synchrony in and among neuronal populations is thought to bind the processing of incoming stimuli [90], representing at least one aspect of the brain's information processing mechanism and causing modulation of power in oscillatory bands. This neural activity may be viewed from a variety of perspectives; for example, spatially localized activity may correspond to distinct populations of neurons processing similar types of information. Modulation of power in distinct frequency bands may correspond to the actual processing of stimuli. Temporally varying features may represent the dynamic response of the cortex to time-varying inputs and outputs. BCIs should consider the most pertinent information encoded in each of these domains to properly interpret the dynamics of cortical activity.

A variety of methods for classifying or decoding movement from surface field potentials have been demonstrated successfully using human and nonhuman primate neural activity [50-53, 55, 57, 58, 61, 91-95]. Elaborate algorithms have been employed to select features from neural data, including statistical methods [53, 91], wavelet decomposition [92], principal component analysis [50], the genetic algorithm [92, 93, 95], system identification using adaptive filtering [55], and linear and nonlinear regressions [93-95]. Various classifiers including support vector machines (SVM) [94, 95], Kalman filters [53], statistical significance in difference between features [92], and linear classifiers [51, 93] have been used. While complex and sophisticated methods may offer slightly improved results, they often function as a black box, providing little insight into the underlying data.

Conclusion

As outlined previously, the significant contribution of this dissertation is to demonstrate that cortical surface potentials can be usefully recorded at the millimeter scale by dense grids of microelectrodes. Thus, the focus of the work was to explore signals

and algorithms in order to better understand the observable mechanisms of the human neocortex as, for example, speech is articulated, or an arm is extended to grasp an object.

Data for this work were acquired from human subjects in collaboration with the Department of Neurosurgery and with the approval of the Institutional Review Board. Several tasks were designed which engage patients while their neural activity is sensed by nonpenetrating microelectrodes. For example, a motor task required a patient to move a mouse on a computer tablet, and a speech task required a patient to repeat articulations of a single word. While patients performed these tasks, their neural activity was recorded from surface microelectrodes for later analysis.

Field potentials are typically analyzed in the frequency domain; however, one of the findings of this work has been that patterns in space and time are at least as important as those in the frequency domain. Relationships among these dimensions were explored in some depth in order to understand the nature of the signals as well as the best features to use for BCI applications. Classification methods were developed using straightforward clustering techniques on the leading principal components of feature matrices. The Kalman filter was also explored for proportional decodes.

Although the microelectrodes used in this work are approved by the FDA for use in human patients, they had not been well characterized previously. The microelectrode grids were manufactured using the same materials as clinical ECoG electrodes, only with much smaller interelectrode spacing and exposed metal areas. Electrochemical impedance spectroscopy (EIS) was performed on the nonpenetrating microelectrodes to evaluate the complex impedance response. Correlation and coherence were used to explore spatiotemporal linear relationships of the recorded signals.

The work described in this dissertation represents tightly integrated collaboration between neuroscience, neurosurgery, and engineering to explore nonpenetrating microelectrodes for BCI applications. Techniques for processing high-bandwidth sensor data in low-power digital VLSI systems will contribute to the viable design of a low-

power, implantable BCI system. Investigation of novel, nonpenetrating microelectrodes will contribute to capabilities for recording high spatiotemporal resolution surface local field potentials. Demonstration of classification algorithms for these novel surface LFP signals will contribute to a better understanding of how the brain's processing mechanisms are represented in cortical surface field potentials.

While some novelty is inherent a new and exciting domain of research, this dissertation also includes significant first-time achievements: for example, the first published work to classify discrete words from brain activity recorded by nonpenetrating microelectrodes over motor and speech areas of the cortex. This work also represents the forefront of exploring the scale of information processing features in the spatiotemporal dynamics of cortical activity at the cortical surface. In sum, this work represents important advances in scientific and engineering knowledge to enable interfaces between machines and the human cortex through high-density nonpenetrating microelectrode grids.

References

- [1] J. P. Lynch and K. J. Loh, "A summary review of wireless sensors and sensor networks for structural health monitoring," *Shock and Vibration Digest*, vol. 38, p. 91, 2006.
- [2] N. Wang, N. Zhang, and M. Wang, "Wireless sensors in agriculture and food industry--recent development and future perspective," *Comput. Electron. Agricult.*, vol. 50, pp. 1-14, 2006.
- [3] K. D. Wise, "Integrated sensors, MEMS, and microsystems: reflections on a fantastic voyage," *Sensors and Actuators A: Physical*, vol. 136, pp. 39-50, 2007.
- [4] K. D. Wise, D. J. Anderson, J. F. Hetke, D. R. Kipke, and K. Najafi, "Wireless implantable microsystems: high-density electronic interfaces to the nervous system," *Proc. IEEE*, vol. 92, pp. 76-97, 2004.
- [5] E. J. Duarte-Melo and M. Liu, "Analysis of energy consumption and lifetime of heterogeneous wireless sensor networks," in *IEEE Global Communications Conf.*, 2002.
- [6] M. Horowitz, T. Indermaur, and R. Gonzalez, "Low-power digital design," in *Proc. Symp. Low Power Electronics*, 1994, pp. 8-11.

- [7] B. Brock and K. Rajamani, "Dynamic power management for embedded systems [SOC design]," in *Proc. IEEE Int. System-on-Chip Conf.*, 2003, pp. 416-419.
- [8] T. Simunic, L. Benini, P. Glynn, and G. De Micheli, "Event-driven power management," *IEEE Trans. Comput.-Aided Des. Integr. Circuits Syst.*, vol. 20, pp. 840-857, 2001.
- [9] Y. Wu, S. Fahmy, and N. B. Shroff, "Sleep/wake scheduling for multi-hop sensor networks: non-convexity and approximation algorithm," *Ad Hoc Networks*, vol. 8, pp. 681-693, 2010.
- [10] L. Benini, A. Bogliolo, and G. De Micheli, "A survey of design techniques for system-level dynamic power management," *IEEE Trans. Very Large Scale Integr. (VLSI) Syst.*, vol. 8, pp. 299-316, 2000.
- [11] Y. Perelman and R. Ginosar, "An integrated system for multichannel neuronal recording with spike/LFP separation, integrated A/D conversion and threshold detection," *IEEE Trans. Biomed. Eng.*, vol. 54, pp. 130-137, 2007.
- [12] D. A. Borton, S. Yoon-Kyu, W. R. Patterson, C. W. Bull, P. Sunmee, F. Laiwalla, J. P. Donoghue, and A. V. Nurmikko, "Wireless, high-bandwidth recordings from non-human primate motor cortex using a scalable 16-Ch implantable microsystem," in *Proc. IEEE Engineering in Medicine and Biology Conf.*, 2009, pp. 5531-5534.
- [13] R. R. Harrison, P. T. Watkins, R. J. Kier, R. O. Lovejoy, D. J. Black, B. Greger, and F. Solzbacher, "A low-power integrated circuit for a wireless 100-electrode neural recording system," *IEEE J. Solid-State Circuits*, vol. 42, pp. 123-133, 2007.
- [14] C. Moo Sung, Y. Zhi, M. R. Yuce, H. Linh, and W. Liu, "A 128-Channel 6 mW wireless neural recording IC with spike feature extraction and UWB transmitter," *IEEE Trans. Neural Syst. Rehabil. Eng.*, vol. 17, pp. 312-321, 2009.
- [15] M. Roham, D. P. Covey, D. P. Daberkow, E. S. Ramsson, C. D. Howard, B. A. Heidenreich, P. A. Garris, and P. Mohseni, "A wireless IC for time-share chemical and electrical neural recording," *IEEE J. Solid-State Circuits*, vol. 44, pp. 3645-3658, 2009.
- [16] A. M. Sodagar, G. E. Perlin, Y. Ying, K. Najafi, and K. D. Wise, "An implantable 64-channel wireless microsystem for single-unit neural recording," *IEEE J. Solid-State Circuits*, vol. 44, pp. 2591-2604, 2009.
- [17] J. N. Y. Aziz, R. Genov, B. R. Bardakjian, M. Derchansky, and P. L. Carlen, "256-channel integrated neural interface and spatio-temporal signal processor," in *Proc. IEEE Int. Symp. Circuits and Systems*, 2006, pp. 5075-5078.
- [18] M. Mollazadeh, K. Murari, G. Cauwenberghs, and N. Thakor, "Micropower CMOS integrated low-noise amplification, filtering, and digitization of multimodal neuropotentials," *IEEE Trans. Biomed. Circuits Syst.*, vol. 3, pp. 1-10, 2009.

- [19] H. Miranda, V. Gilja, C. A. Chestek, K. V. Shenoy, and T. H. Meng, "HermesD: a high-rate long-range wireless transmission system for simultaneous multichannel neural recording applications," *IEEE Trans. Biomed. Circuits Syst.*, vol. 4, pp. 181-191, 2010.
- [20] P. Mohseni, K. Najafi, S. J. Eliades, and W. Xiaojin, "Wireless multichannel biopotential recording using an integrated FM telemetry circuit," *IEEE Trans. Neural Syst. Rehabil. Eng.*, vol. 13, pp. 263-271, 2005.
- [21] R. H. Olsson, III and K. D. Wise, "A three-dimensional neural recording microsystem with implantable data compression circuitry," *IEEE J. Solid-State Circuits*, vol. 40, pp. 2796-2804, 2005.
- [22] D. J. Yeager, J. Holleman, R. Prasad, J. R. Smith, and B. P. Otis, "NeuralWISP: a wirelessly powered neural interface with 1-m range," *IEEE Trans. Biomed. Circuits Syst.*, vol. 3, pp. 379-387, 2009.
- [23] T. A. Szuts, V. Fadeyev, S. Kachiguine, A. Sher, M. V. Grivich, M. Agrochao, P. Hottowy, W. Dabrowski, E. V. Lubenov, A. G. Siapas, N. Uchida, A. M. Litke, and M. Meister, "A wireless multi-channel neural amplifier for freely moving animals," *Nat. Neurosci.*, vol. 14, pp. 263-269, 2011.
- [24] E. Greenwald, M. Mollazadeh, C. Hu, T. Wei, E. Culurciello, and V. Thakor, "A VLSI neural monitoring system with ultra-wideband telemetry for awake behaving subjects," *IEEE Trans. Biomed. Circuits Syst.*, vol. 5, pp. 112-119, 2011.
- [25] J. Mavoori, A. Jackson, C. Diorio, and E. Fetz, "An autonomous implantable computer for neural recording and stimulation in unrestrained primates," *J. Neurosci. Meth.*, vol. 148, pp. 71-77, Oct. 2005.
- [26] S. Farshchi, A. Pesterev, P. Nuyujukian, E. Guenterberg, I. Mody, and J. W. Judy, "Embedded neural recording with TinyOS-based wireless-enabled processor modules," *IEEE Trans. Neural Syst. Rehabil. Eng.*, vol. 18, pp. 134-141, 2010.
- [27] D. Cheney, G. Aik, X. Jie, K. Gugel, J. G. Harris, J. C. Sanchez, and J. C. Principe, "Wireless, in vivo neural recording using a custom integrated bioamplifier and the Pico system," in *Proc. IEEE/EMBS Int. Conf. Neural Eng.*, 2007, pp. 19-22.
- [28] R. F. Yazicioglu, S. Kim, T. Torfs, H. Kim, and C. Van Hoof, "A 30 uW analog signal processor ASIC for portable biopotential signal monitoring," *IEEE J. Solid-State Circuits*, vol. 46, pp. 209-223, 2011.
- [29] A. P. Georgopoulos, R. E. Kettner, and A. B. Schwartz, "Primate motor cortex and free arm movements to visual targets in three-dimensional space. II. Coding of the direction of movement by a neuronal population," *J. Neurosci.*, vol. 8, pp. 2928-2937, Aug. 1988.

- [30] R. E. Kettner, A. B. Schwartz, and A. P. Georgopoulos, "Primate motor cortex and free arm movements to visual targets in three-dimensional space. III. Positional gradients and population coding of movement direction from various movement origins," *J. Neurosci.*, vol. 8, pp. 2938-2947, Aug. 1988.
- [31] A. B. Schwartz, R. E. Kettner, and A. P. Georgopoulos, "Primate motor cortex and free arm movements to visual targets in three-dimensional space. I. Relations between single cell discharge and direction of movement," *J. Neurosci.*, vol. 8, pp. 2913-2927, Aug. 1988.
- [32] J. Wessberg, C. R. Stambaugh, J. D. Kralik, P. D. Beck, M. Laubach, J. K. Chapin, J. Kim, S. J. Biggs, M. A. Srinivasan, and M. A. Nicolelis, "Real-time prediction of hand trajectory by ensembles of cortical neurons in primates," *Nature*, vol. 408, pp. 361-365, Nov. 2000.
- [33] L. R. Hochberg, M. D. Serruya, G. M. Friehs, J. A. Mukand, M. Saleh, A. H. Caplan, A. Branner, D. Chen, R. D. Penn, and J. P. Donoghue, "Neuronal ensemble control of prosthetic devices by a human with tetraplegia," *Nature*, vol. 442, pp. 164-171, Jul. 2006.
- [34] M. D. Serruya, N. G. Hatsopoulos, L. Paninski, M. R. Fellows, and J. P. Donoghue, "Instant neural control of a movement signal," *Nature*, vol. 416, pp. 141-142, Mar. 2002.
- [35] D. M. Taylor, S. I. Tillery, and A. B. Schwartz, "Direct cortical control of 3D neuroprosthetic devices," *Science*, vol. 296, pp. 1829-1832, Jun. 2002.
- [36] J. Bartels, D. Andreasen, P. Ehirim, H. Mao, S. Seibert, E. J. Wright, and P. R. Kennedy, "Neurotrophic electrode: method of assembly and implantation into human motor speech cortex," *J. Neurosci. Meth.*, vol. 174, pp. 168-176, 2008.
- [37] P. R. Kennedy, R. A. Bakay, M. M. Moore, K. Adams, and J. Goldwithe, "Direct control of a computer from the human central nervous system," *IEEE Trans. Rehabil. Eng.*, vol. 8, pp. 198-202, 2000.
- [38] F. H. Guenther, J. S. Brumberg, E. J. Wright, A. Nieto-Castanon, J. A. Tourville, M. Panko, R. Law, S. A. Siebert, J. L. Bartels, D. S. Andreasen, P. Ehirim, H. Mao, and P. R. Kennedy, "A wireless brain-machine interface for real-time speech synthesis," *PloS one*, vol. 4, p. e8218, 2009.
- [39] F. H. Guenther, S. S. Ghosh, and J. A. Tourville, "Neural modeling and imaging of the cortical interactions underlying syllable production," *Brain and Lang.*, vol. 96, pp. 280-301, 2006.
- [40] N. Birbaumer, N. Ghanayim, T. Hinterberger, I. Iversen, B. Kotchoubey, A. Kübler, J. Perelmouter, E. Taub, and H. Flor, "A spelling device for the paralysed," *Nature*, vol. 398, pp. 297-298, 1999.

- [41] J. J. Daly and J. R. Wolpaw, "Brain-computer interfaces in neurological rehabilitation," *Lancet Neurol.*, vol. 7, pp. 1032-1043, Nov. 2008.
- [42] E. Donchin, K. M. Spencer, and R. Wijesinghe, "The mental prosthesis: assessing the speed of a P300-based brain-computer interface," *IEEE Trans. Rehabil. Eng.*, vol. 8, pp. 174-179, Jun. 2000.
- [43] L. A. Farwell and E. Donchin, "Talking off the top of your head: toward a mental prosthesis utilizing event-related brain potentials," *Electroencephalogr. Clin. Neurophysiol.*, vol. 70, pp. 510-523, Dec. 1988.
- [44] A. Kübler, B. Kotchoubey, T. Hinterberger, N. Ghanayim, J. Perelmouter, M. Schauer, C. Fritsch, E. Taub, and N. Birbaumer, "The thought translation device: a neurophysiological approach to communication in total motor paralysis," *Exp. Brain Res.*, vol. 124, pp. 223-232, 1999.
- [45] F. Nijboer, E. W. Sellers, J. Mellinger, M. A. Jordan, T. Matuz, A. Furdea, S. Halder, U. Mochty, D. J. Krusienski, T. M. Vaughan, J. R. Wolpaw, N. Birbaumer, and A. Kubler, "A P300-based brain-computer interface for people with amyotrophic lateral sclerosis," *Clin. Neurophysiol.*, vol. 119, pp. 1909-1916, Aug. 2008.
- [46] J. R. Wolpaw and D. J. McFarland, "Multichannel EEG-based brain-computer communication," *Electroencephalogr. Clin. Neurophysiol.*, vol. 90, pp. 444-449, Jun. 1994.
- [47] N. Birbaumer, "Breaking the silence: brain-computer interfaces (BCI) for communication and motor control," *Psychophysiol.*, vol. 43, pp. 517-532, Nov. 2006.
- [48] D. J. McFarland, D. J. Krusienski, W. A. Sarnacki, and J. R. Wolpaw, "Emulation of computer mouse control with a noninvasive brain-computer interface," *J. Neural Eng.*, vol. 5, pp. 101-110, Jun. 2008.
- [49] S. Zanos, K. J. Miller, and J. G. Ojemann, "Electrocorticographic spectral changes associated with ipsilateral individual finger and whole hand movement," in *Proc. IEEE Engineering in Medicine and Biology Conf.*, 2008, pp. 5939-5942.
- [50] K. J. Miller, S. Zanos, E. E. Fetz, M. den Nijs, and J. G. Ojemann, "Decoupling the cortical power spectrum reveals real-time representation of individual finger movements in humans," *J. Neurosci.*, vol. 29, pp. 3132-3137, 2009.
- [51] R. Scherer, S. P. Zanos, K. J. Miller, R. P. N. Rao, and J. G. Ojemann, "Classification of contralateral and ipsilateral finger movements for electrocorticographic brain-computer interfaces," *Neurosurg. Focus*, vol. 27, p. E12, 2009.
- [52] L. Bougrain and N. Liang, "Band-specific features improve finger flexion prediction from ECoG," *Jornadas Argentinas sobre Interfaces Cerebro Computadora*, vol. 2009, pp. 1-4, 2009.

- [53] T. Pistohl, T. Ball, A. Schulze-Bonhage, A. Aertsen, and C. Mehring, "Prediction of arm movement trajectories from ECoG-recordings in humans," *J. Neurosci. Meth.*, vol. 167, pp. 105-114, 2008.
- [54] T. Yanagisawa, M. Hirata, Y. Saitoh, A. Kato, D. Shibuya, Y. Kamitani, and T. Yoshimine, "Neural decoding using gyral and intrasulcal electrocorticograms," *Neuroimage*, vol. 45, pp. 1099-1106, May 2009.
- [55] J. C. Sanchez, A. Gunduz, P. R. Carney, and J. C. Principe, "Extraction and localization of mesoscopic motor control signals for human ECoG neuroprosthetics," *J. Neurosci. Meth.*, vol. 167, pp. 63-81, 2008.
- [56] S. S. Kellis, P. A. House, K. E. Thomson, R. Brown, and B. Greger, "Human neocortical electrical activity recorded on nonpenetrating microwire arrays: applicability for neuroprostheses," *Neurosurg. Focus*, vol. 27, p. E9, 2009.
- [57] G. Schalk, J. Kubanek, K. J. Miller, N. R. Anderson, E. C. Leuthardt, J. G. Ojemann, D. Limbrick, D. Moran, L. A. Gerhardt, and J. R. Wolpaw, "Decoding two-dimensional movement trajectories using electrocorticographic signals in humans," *J. Neural Eng.*, vol. 4, pp. 264-275, Sep. 2007.
- [58] G. Schalk, K. J. Miller, N. R. Anderson, J. A. Wilson, M. D. Smyth, J. G. Ojemann, D. W. Moran, J. R. Wolpaw, and E. C. Leuthardt, "Two-dimensional movement control using electrocorticographic signals in humans," *J. Neural Eng.*, vol. 5, pp. 75-84, Mar. 2008.
- [59] T. N. Lal, T. Hinterberger, G. Widman, M. Schroeder, J. Hill, W. Rosenstiel, C. Elger, B. Schölkopf, and N. Birbaumer, *Methods towards invasive human brain computer interfaces*, 2005.
- [60] E. C. Leuthardt, G. Schalk, J. R. Wolpaw, J. G. Ojemann, and D. W. Moran, "A brain-computer interface using electrocorticographic signals in humans," *J. Neural Eng.*, vol. 1, pp. 63-71, 2004.
- [61] T. Blakely, K. J. Miller, R. P. Rao, M. D. Holmes, and J. G. Ojemann, "Localization and classification of phonemes using high spatial resolution electrocorticography (ECoG) grids," in *Proc. IEEE Engineering in Medicine and Biology Conf.*, 2008, pp. 4964-4967.
- [62] N. Crone, D. Miglioretti, B. Gordon, and R. Lesser, "Functional mapping of human sensorimotor cortex with electrocorticographic spectral analysis. II. Event-related synchronization in the gamma band," *Brain*, vol. 121, pp. 2301-2315, 1998.
- [63] N. E. Crone, L. Hao, J. Hart, Jr., D. Boatman, R. P. Lesser, R. Irizarry, and B. Gordon, "Electrocorticographic gamma activity during word production in spoken and sign language," *Neurol.*, vol. 57, pp. 2045-2053, Dec. 2001.

- [64] E. Edwards, S. S. Nagarajan, S. S. Dalal, R. T. Canolty, H. E. Kirsch, N. M. Barbaro, and R. T. Knight, "Spatiotemporal imaging of cortical activation during verb generation and picture naming," *Neuroimage*, vol. 50, pp. 291-301, Mar. 2010.
- [65] V. L. Towle, H.-A. Yoon, M. Castelle, J. C. Edgar, N. M. Biassou, D. M. Frim, J.-P. Spire, and M. H. Kohrman, "ECoG gamma activity during a language task: differentiating expressive and receptive speech areas," *Brain*, vol. 131, pp. 2013-2027, 2008.
- [66] H. Scherberger, M. R. Jarvis, and R. A. Andersen, "Cortical local field potential encodes movement intentions in the posterior parietal cortex," *Neuron*, vol. 46, pp. 347-354, 2005.
- [67] A. K. Bansal, C. E. Vargas-Irwin, W. Truccolo, and J. P. Donoghue, "Relationships among low-frequency local field potentials, spiking activity, and three-dimensional reach and grasp kinematics in primary motor and ventral premotor cortices," *J. Neurophysiol.*, vol. 105, pp. 1603-1619, Apr. 2011.
- [68] Z. Jun, W. Truccolo, C. Vargas-Irwin, and J. P. Donoghue, "Decoding 3-D reach and grasp kinematics from high-frequency local field potentials in primate primary motor cortex," *IEEE Trans. Biomed. Eng.*, vol. 57, pp. 1774-1784, 2010.
- [69] M. Mollazadeh, V. Aggarwal, A. G. Davidson, A. J. Law, N. V. Thakor, and M. H. Schieber, "Spatiotemporal variation of multiple neurophysiological signals in the primary motor cortex during dexterous reach-to-grasp movements," *J. Neurosci.*, vol. 31, pp. 15531-15543, Oct. 2011.
- [70] J. Rickert, S. C. de Oliveira, E. Vaadia, A. Aertsen, S. Rotter, and C. Mehring, "Encoding of movement direction in different frequency ranges of motor cortical local field potentials," *J. Neurosci.*, vol. 25, pp. 8815-8824, Sept. 2005.
- [71] J. Baker, W. Bishop, S. Kellis, T. Levy, P. House, and B. Greger, "Multi-scale recordings for neuroprosthetic control of finger movements," in *Proc. IEEE Engineering in Medicine and Biology Conf.*, 2009, pp. 4573-4577.
- [72] S. Katzner, I. Nauhaus, A. Benucci, V. Bonin, D. L. Ringach, and M. Carandini, "Local origin of field potentials in visual cortex," *Neuron*, vol. 61, pp. 35-41, 2009.
- [73] R. A. Normann, E. M. Maynard, P. J. Rousche, and D. J. Warren, "A neural interface for a cortical vision prosthesis," *Vision Res.*, vol. 39, pp. 2577-2587, 1999.
- [74] R. Mukamel, H. Gelbard, A. Arieli, U. Hasson, I. Fried, and R. Malach, "Coupling between neuronal firing, field potentials, and fMRI in human auditory cortex," *Science*, vol. 309, pp. 951-954, Aug. 2005.
- [75] P. Lakatos, A. S. Shah, K. H. Knuth, I. Ulbert, G. Karmos, and C. E. Schroeder, "An oscillatory hierarchy controlling neuronal excitability and stimulus processing in the auditory cortex," *J. Neurophysiol.*, vol. 94, pp. 1904-1911, Sep. 2005.

- [76] V. N. Murthy and E. E. Fetz, "Oscillatory activity in sensorimotor cortex of awake monkeys: synchronization of local field potentials and relation to behavior," *J. Neurophysiol.*, vol. 76, pp. 3949-3967, Dec. 1996.
- [77] J. Sarnthein, A. Morel, A. von Stein, and D. Jeanmonod, "Thalamic theta field potentials and EEG: high thalamocortical coherence in patients with neurogenic pain, epilepsy and movement disorders," *Thalamus Related Syst.*, vol. 2, pp. 231-238, 2003.
- [78] C. A. Schevon, S. K. Ng, J. Cappell, R. R. Goodman, G. J. McKhann, A. Waziri, A. Branner, A. Sosunov, C. E. Schroeder, and R. G. Emerson, "Microphysiology of epileptiform activity in human neocortex," *J. Clin. Neurophysiol.*, vol. 25, pp. 321-330, 2008.
- [79] R. Cooper, A. L. Winter, H. J. Crow, and W. G. Walter, "Comparison of subcortical, cortical and scalp activity using chronically indwelling electrodes in man," *Electroencephalogr. Clin. Neurophysiol.*, vol. 18, pp. 217-228, Feb. 1965.
- [80] G. Pfurtscheller and R. Cooper, "Frequency dependence of the transmission of the EEG from cortex to scalp," *Electroencephalogr. Clin. Neurophysiol.*, vol. 38, pp. 93-96, Jan. 1975.
- [81] N. E. Crone, A. Sinai, and A. Korzeniewska, "High-frequency gamma oscillations and human brain mapping with electrocorticography," *Prog. Brain Res.*, vol. 159, pp. 275-295, 2006.
- [82] V. Menon, W. J. Freeman, B. A. Cuttillo, J. E. Desmond, M. F. Ward, S. L. Bressler, K. D. Laxer, N. Barbaro, and A. S. Gevins, "Spatio-temporal correlations in human gamma band electrocorticograms," *Electroencephalogr. Clin. Neurophysiol.*, vol. 98, pp. 89-102, 1996.
- [83] G. Buzsaki and J. J. Chrobak, "Temporal structure in spatially organized neuronal ensembles: a role for interneuronal networks," *Curr. Opin. Neurobiol.*, vol. 5, pp. 504-510, Aug. 1995.
- [84] W. Singer, "Synchronization of cortical activity and its putative role in information processing and learning," *Annu. Rev. Physiol.*, vol. 55, pp. 349-374, 1993.
- [85] T. Womelsdorf, J. M. Schoffelen, R. Oostenveld, W. Singer, R. Desimone, A. K. Engel, and P. Fries, "Modulation of neuronal interactions through neuronal synchronization," *Science*, vol. 316, pp. 1609-1612, Jun. 2007.
- [86] E. C. Leuthardt, Z. Freudenberg, D. Bundy, and J. Roland, "Microscale recording from human motor cortex: implications for minimally invasive electrocorticographic brain-computer interfaces," *Neurosurg. Focus*, vol. 27, p. E10, 2009.

- [87] K. J. Miller, E. C. Leuthardt, G. Schalk, R. P. N. Rao, N. R. Anderson, D. W. Moran, J. W. Miller, and J. G. Ojemann, "Spectral changes in cortical surface potentials during motor movement," *J. Neurosci.*, vol. 27, pp. 2424-2432, 2007.
- [88] S. Ohara, A. Ikeda, T. Kunieda, S. Yazawa, K. Baba, T. Nagamine, W. Taki, N. Hashimoto, T. Mihara, and H. Shibasaki, "Movement-related change of electrocorticographic activity in human supplementary motor area proper," *Brain*, vol. 123, pp. 1203-1215, Jun. 2000.
- [89] G. Pfurtscheller, B. Graimann, J. E. Huggins, S. P. Levine, and L. A. Schuh, "Spatiotemporal patterns of beta desynchronization and gamma synchronization in corticographic data during self-paced movement," *Clin. Neurophysiol.*, vol. 114, pp. 1226-1236, 2003.
- [90] W. Singer and C. M. Gray, "Visual feature integration and the temporal correlation hypothesis," *Annu. Rev. Neurosci.*, vol. 18, pp. 555-586, 1995.
- [91] T. H. Dat, L. Shue, and C. Guan, "Electrocorticographic signal classification based on time-frequency decomposition and nonparametric statistical modeling," in *Proc. IEEE Engineering in Medicine and Biology Conf.*, 2006, pp. 2292-2295.
- [92] B. Graimann, J. E. Huggins, S. P. Levine, and G. Pfurtscheller, "Toward a direct brain interface based on human subdural recordings and wavelet-packet analysis," *IEEE Trans. Biomed. Eng.*, vol. 51, pp. 954-962, 2004.
- [93] B. Graimann, J. E. Huggins, A. Schlogl, S. P. Levine, and G. Pfurtscheller, "Detection of movement-related patterns in ongoing single-channel electrocorticogram," *IEEE Trans. Neural Syst. Rehabil. Eng.*, vol. 11, pp. 276-281, 2003.
- [94] N. J. Hill, T. N. Lal, M. Schroder, T. Hinterberger, B. Wilhelm, F. Nijboer, U. Mochty, G. Widman, C. Elger, B. Scholkopf, A. Kubler, and N. Birbaumer, "Classifying EEG and ECoG signals without subject training for fast BCI implementation: comparison of nonparalyzed and completely paralyzed subjects," *IEEE Trans. Neural Syst. Rehabil. Eng.*, vol. 14, pp. 183-186, 2006.
- [95] W. Qingguo, G. Xiaorong, and G. Shangkai, "Feature Extraction and Subset Selection for Classifying Single-Trial ECoG during Motor Imagery," in *Proc. IEEE Engineering in Medicine and Biology Conf.*, 2006, pp. 1589-1592.

CHAPTER 2

SELECTED TECHNIQUES FOR LOW-POWER DIGITAL VLSI

Modern VLSI technology enables integration of entire systems in a single chip, thereby enabling or expanding many applications for research. Among the most compelling of these opportunities are embedded systems for neural prosthetics. In these systems, sensors record neural activity that is interpreted on-chip to direct actuation of a prosthetic device. Chronic in vivo operation in the unique context of a neural interface precludes the use of large batteries or tethered power supplies; additionally, excessive heat dissipation could damage surrounding tissue. For these reasons, the components of an embedded neural interface must be designed and characterized to operate on a limited energy supply in a heat-sensitive environment. The WIMS microcontroller was designed as a control element for implantable biosensor systems and has been shown to operate efficiently in previous CMOS implementations [1, 2]. It is used in this work to explore methods which could allow more efficient processing of high-bandwidth data in a power-limited environment.

Managing the power requirements of VLSI circuits has been an area of significant research (e.g., [3, 4]). For many years, CMOS process scaling provided inherent improvements, as power decreased with the square of supply voltage (which was lowered with each new process) while increasing only linearly with operating frequency. However, the increasing contribution of leakage to total system power consumption in submicron processes has required substantial effort to continue to improve performance while managing power [5]. Advances have been made at the physical or electrical level such as high-K dielectrics [6], tri-gate devices [7], and body biasing [8, 9]. Other advances have

been made at the architectural level, for example, clock gating [10], dynamic voltage and frequency scaling [11], and parallel execution [12]. Still others have looked at software level optimizations [13]. As the broad spectrum of topics represented in these studies illustrates, power optimization is a holistic problem encompassing all aspects of a system from silicon to software. This work has explored an architectural method for improving power efficiency, and a CAD analysis technique to aid in power-related design decisions.

WIMS microcontroller

The WIMS acronym stands for Wireless Integrated Microsystems, and refers to an NSF-funded Engineering Research Center whose goal was to develop microsystems capable of sensing, processing, and communicating in a fully integrated platform. The WIMS microcontroller architecture was developed in the context of the WIMS research effort by students at the University of Michigan, with specific contributions acknowledged by references in the text of this chapter. Development of the microcontroller continued at the University of Utah as the program evolved. The scope of work required to design and implement a pipelined microcontroller in a submicron CMOS process necessitates that it be a collaborative effort. Contributions of this thesis, as described in this chapter, include assisting in the implementation of the third generation of the WIMS microcontroller, and making evolutionary changes to the architecture [14]. Previous students and current peers, whose collaborative efforts made these contributions possible, are gratefully acknowledged.

The WIMS load-store instruction set architecture (ISA) contains 89 instructions supporting eight addressing modes and single- and multiword arithmetic, shift, logical, and control-flow operations. Instructions in the custom ISA were carefully chosen to minimize decode complexity and power without sacrificing functionality. One level of interrupt and subroutine support is available in hardware with more available through software control of the hardware stack.

A three-stage pipeline provides adequate performance with minimal pipeline hardware overhead. The pipeline utilizes sixteen 16-bit general purpose registers and fourteen 24-bit address registers, divided evenly over two windows. The windowing scheme reduces the register encoding field to enable 16-bit instructions while providing additional registers for temporary storage. When properly utilized, windowing corresponds to as much as 19% reduction in power consumption and 30% improvement in performance compared to a nonwindowed implementation [15].

The memory architecture is a banked style with 32KB of on-chip SRAM split into four 8KB banks. This allows instruction and data accesses to occur simultaneously without stalling the pipeline as long as they address different banks. This is easily achieved with minimal organizational control by the software compiler. In addition, this memory configuration allows for unused banks to be shut down on a cycle-by-cycle basis when not being accessed, yielding an overall power savings in the memory.

Considerable power savings in the memory architecture is realized by the addition of a low-power, 1 kB scratchpad memory. Unlike traditional caches, the scratchpad memory is a tagless bank of low-power memory managed by the WIMS C compiler. The scratchpad is intended to contain the most commonly executed instructions or accessed data, typically found in program loops. Contents of the scratchpad are determined by the compiler and are not under hardware control, as is typical of memory hierarchy caches. It is possible to change the contents of the scratchpad memory dynamically by loading new instructions or data into the scratchpad and resuming program execution. The scratchpad memory introduces minimal hardware overhead due to the banked memory structure, but yields significant power savings [16, 17].

Block transfer instructions

Modern neural signal acquisition systems acquire data in staggering volumes. A typical system might support (at a minimum) 128 channels of data, each sampled 1000 or

more times per second with 12 bits per sample. For a conservative algorithm, which might operate on perhaps 0.5 seconds of data, the system must be able to store and process 93.75 KB of data on a continuous basis—a challenge for an embedded system with potentially limited storage and energy resources. In this scenario, traditional load/store instructions, which typically copy single words of data, suffer from an inefficient ratio of operational overhead to work done.

To more efficiently move large amounts of data around the system, the Gen-3 WIMS ISA includes a family of instructions which transfer a variable amount of data to and from registers, the scratchpad memory, and standard SRAM [14]. The four available instructions allow relative or absolute addressing for both load and store operations.

Executing a block transfer instruction requires initialization of one 16-bit data register, one 24-bit address register, and four memory-mapped registers. While this overhead makes it unlikely that the block transfer will be more efficient than a simple load or store instruction for small amounts of data, it is expected that for filling or emptying the scratchpad memory, for example, the single instruction approach will save significant amounts of energy over the fetch, decode, and execution of many single load or store operations.

Characterizing energy use

Another factor influencing power consumption in a digital system is the efficiency of the code which is executed by the microcontroller. The WIMS microcontroller implements an energy-efficient ISA, but peak efficiency requires awareness of the energy implications of software-level decisions such as instruction ordering, data flow, and memory access. A power-aware compiler was designed to generate more efficient assembly code using the energy profile of the ISA. To evaluate these energy requirements, test cases were designed to measure the energy required by instructions using similar functional units, such as add and subtract. The contribution of this dissertation was to measure the energy

per instruction of the most recently fabricated WIMS microcontroller, and to extend this technique to work in simulation.

The method used for determining energy per instruction was first presented in the context of the Gen-2 WIMS microcontroller [18]. The method was greatly simplified by the absence of a dynamic caching subsystem in the WIMS architecture. To avoid underestimating energy by continuously fetching and decoding the same or similar bytecode, switching activity was modeled by interleaving no-ops between each instruction. The presence of no-op instructions can also mitigate variance due to data-dependent micro-architectural operation, e.g., by potentially reducing the occurrence of pipeline stalls. Instructions using the same hardware, such as add and subtract, were grouped together to reduce test complexity.

Fast, accurate circuit-level power simulators have made possible the extension of this method to operate in simulation with some expectation of relative accuracy, if not absolute accuracy. To achieve the highest correlation between hardware measurements and simulated measurements, power simulations took into account information about the layout of the circuit and technology parameters specific to the fabrication process. An example of this level of modeling is not included here, but is a largely technical process which may be developed with the assistance of vendor-provided documentation. While instruction-level power simulations may not provide absolute accuracy, they allow fast, efficient evaluation of both architecture and software during design and deployment.

Methods

Evaluation of block transfer instructions

Two specific scenarios were designed to analyze the efficiency of the block transfer instructions. In each case, two test vectors were created: one using a single block transfer instruction, and one using the traditional combination of load or store instructions.

The first scenario was designed to find the point at which block transfers become more efficient than traditional load/store sequences. The test for this scenario transferred consecutively larger blocks of data (up to 512 bytes, in 16-byte chunks) between the low-power scratchpad memory and a bank of SRAM. This scenario represents a potentially frequent operation in an embedded neural interface, which would have to deal with large amounts of data. An equivalent test using traditional load and store operations would require each 16-bit word to be loaded into a data register and then stored to the destination memory address.

A second scenario involved transferring the microcontroller state to the low-power scratchpad memory prior to entering a standby mode. This test case used either the block transfer commands or store instructions to copy all registers in a single register window to the scratchpad memory—a total of 8 data registers, 8 address registers, and 4 auxiliary registers such as the program counter and link registers. For the load/store equivalent, no load instruction was needed before a store instruction copied a 16-bit data register to the scratchpad memory. However, for 24-bit address registers, the data must be copied in two sequences of 16 and 8 bits from the address register to a data register, and finally to memory.

Measuring energy per instruction

Two test vectors were required to measure the energy per instruction of a single family of instructions. A full test vector consisted of the instruction(s) of interest interleaved with no-op instructions (Fig 2.1). The body of the test was preceded by some overhead to prepare registers and was followed by a jump back to the beginning of the test. In each case, a second “boot-up” vector was generated consisting of only the register initialization and looping instructions. The boot-up energy was subtracted from the full test energy, with the remainder equal to the energy required to execute a single iteration of the main body of test code. Then, the energy per no-op instruction, multiplied by the number of

```

loop_start:
    // Part A: initialize registers and memory data
    ldbi r0, 0xff
    ldbi r1, 0xa0
    . . .
    // Part B: measure current for instruction group
    add r0, r1
    noop
    sub r2, r1
    noop
    sub r4, r0
    noop
    . . .
    // Part C: infinitely loop test case
    jmp loop_start

```

Fig. 2.1. Sample program loop in assembly code

no-op instructions in the main body, was subtracted. Finally, this value was divided by the number of non-no-op instructions in the main body to give the energy required to execute a single instruction.

To measure no-op energy, a test case containing hundreds of random instructions was created. Two versions, with and without interleaved no-op instructions, were run on the fabricated chip and current measurements were recorded. The energy to execute a single no-op instruction was determined by dividing the difference in energies between these two versions by the number of no-op instructions in the first test vector.

Hardware measurements were taken with a Verigy 93000 tester using the 65nm Gen-3 WIMS microcontroller clocked at 10MHz with a 0.8V supply. Test vectors were run on the fabricated hardware and current measurements were recorded. The current measurements were converted to energy measurements using the power supply voltage (0.8V) and the time to execute a single loop iteration. The method described above was used to derive energies per instruction family from the recorded measurements.

Measuring energy per instruction in simulation

While accuracy can be very high when measuring energy per instruction in fabricated chips, by that point measured results can only be used to improve hardware in subsequent implementations. The ability to perform such a characterization in simulation could be a useful tool during the design process, when architectural decisions need to be made about the format of the ISA and the required hardware. With the availability of high performance CAD tools, full-chip simulation can be performed with reasonable effort and provide good accuracy.

Synopsys NanoSim, a fast, cycle-accurate functional Verilog simulator, was used to estimate power dissipation and calculate the energy per instruction. A value change dump (VCD) file was generated with `ncverilog` by simulating test cases with a Verilog representation of the Gen-2 WIMS Microcontroller [1]. This VCD file was converted to the VEC format using `vcd2vec`, a tool included with NanoSim. Post auto-place-and-route parasitic capacitance and resistance values were extracted directly from GDS files using Calibre xRC. Vendor-supplied technology parameters for the process, standard cells, and memories provided accurate simulation models of physical hardware structures.

With a netlist description of the microcontroller, input vectors, and technology parameters available, NanoSim was configured to run for the exact length of time recorded in the VCD file. Simulations were run at 100MHz with the core voltage at 1.8V. Energy was calculated by multiplying simulated current at the VDD node by the time spent in simulation. Random code with and without no-ops was simulated to obtain the energy per no-op instruction. All measurements were normalized to the no-op energy to account for absolute inaccuracies. Overhead due to test initialization (i.e., Fig. 2.1, Part A) was simulated separately and subtracted from the total test case energy. Next, no-op energy was subtracted and the result was divided by the number of instructions executed.

The simulations presented here were performed on a different generation of the WIMS microcontroller than the one used for the hardware measurements. While the

results shown here cannot be expected to exactly match the hardware measurements, the trends are valid, and the approach for obtaining energy per instruction from simulations is demonstrated.

Results

Operational power

The third-generation digital pipeline along with the scratchpad memory and 32KB of SRAM were fabricated in the IBM 65nm CMOS HVt process through the MOSIS Educational Program (Fig. 2.2) [14]. Total pad area was 5.86 mm^2 , and digital logic area including pipeline and memory was 0.96 mm^2 . Fabricated chips underwent testing on a Verigy 93000 tester. The minimum operating voltage of the digital logic was 0.7 V at 100 kHz , and at 1 V Vdd , it was functional up to 150 MHz . With a core power supply of 0.8 V , the chip consumed $350 \mu\text{W}$ at 10 MHz . Fig. 2.2 shows the power consumed by the fabricated chip for several combinations of V_{dd} and frequency. To describe these results in

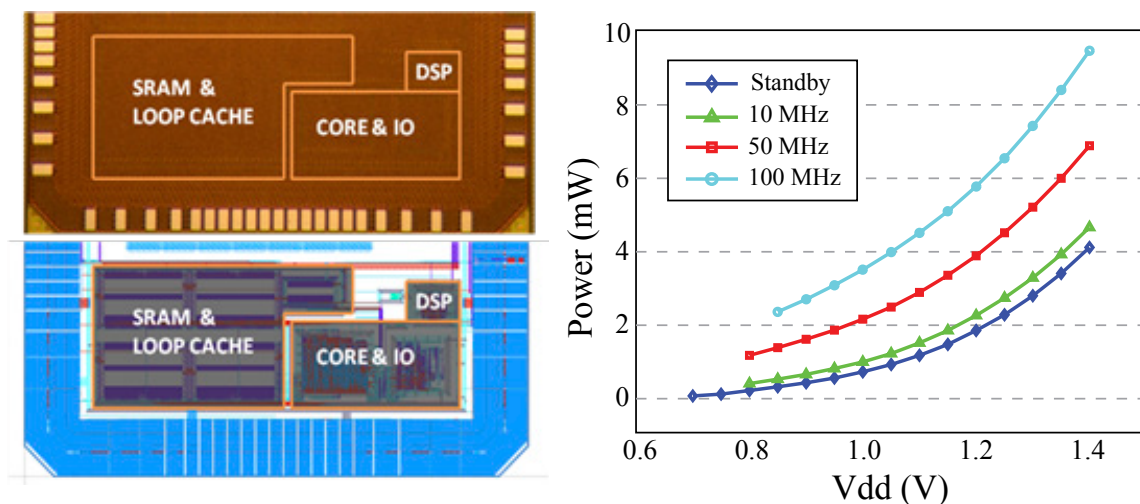


Fig. 2.2. WIMS microcontroller photograph, layout, and power consumption. (Left) WIMS microcontroller fabricated in 65nm IBM CMOS technology. The top portion of this panel is a photograph of the fabricated chip, with most transistor features obscured due to the metallization layer. The bottom portion is a screen capture from the design software. (Right) Power consumption of the fabricated microcontroller at a number of operational frequency and supply voltage points.

practical terms, a 2 g, 20 mAh battery (e.g., QL0020B, Quallion LLC, Sylmar, CA) could sustain the WIMS microcontroller for 45 hours of continuous operation; a 6 g, 230 mAh battery (e.g., QL00230B) could do the same for three weeks.

Energy per instruction: hardware results

The method described earlier to calculate energy per instruction was performed for the fabricated WIMS microcontroller. Based on the recorded current measurements, instruction counts, and execution times, the energy per instruction group was calculated with results shown in Table 2.1. These results bring to light several principles that will be important in programming the microcontroller for low-energy operation.

The energy cost to fetch a 16-bit word was evident in the difference between the absolute and relative loads, stores, and jumps. The absolute-addressed instructions required a second 16-bit word in order to specify the full 24-bit address as an operand. Fetching the extra word corresponded to a 73% increase in energy for the load, 30% increase for the store, and 48% increase for the jump. Increases of this magnitude warrant extra care in making the decision to use the convenience of absolute addressing.

Despite the large amount of energy required by a multiply or divide instruction, these instructions were still more efficient than the corresponding sequence of adds, subtracts, shifts, compares, and branches in most cases. The exception was when, for example, one of the multiplicands is close to a power of two and the result could be determined by a series of shifts and adds. Similar conclusions may be drawn about the efficiency of test-and-set operations compared to the sum of their subcomponents.

Energy per instruction: simulation results

The simulated instruction energies, normalized to the no-op energy, are shown in Table 2.1. Although the relative energies were not always accurate, simulation did preserve architecture-specific trends. For example, multiply and divide required very similar

Table 2.1. Energy of each WIMS instruction group. Measured data from hardware are shown in in nJ and normalized to no-op energy; simulation data are normalized to no-op energy.

Instruction Groups	Hardware Energy (nJ)	Hardware Energy (normalized)	Simulated Energy (normalized)	Clock cycles
add-sub	0.032	0.84	0.91	1
shift	0.029	0.76	1.00	1
boolean	0.034	0.89	0.94	1
compare	0.031	0.82	0.89	1
multiply	0.567	14.9	17.5	18
div	0.506	13.3	16.9	18
bit	0.102	2.68	2.78	2
load-abs	0.063	1.66	1.84	2
load-rel	0.036	0.94	1.85	1
store-abs	0.087	2.29	1.96	2
store-rel	0.067	1.76	0.90	1
swap	0.027	0.71	0.85	1
branch-nt	0.026	0.68	0.80	1
branch-t	0.091	2.39	2.83	3
jump	0.086	2.26	3.06	3
jmp-rel	0.053	1.39	2.15	2
jump-sub	0.078	2.05	2.19	3
jmp-rel-sub	0.062	1.63	0.78	2
ret	0.063	1.66	2.83	2
swi	0.086	2.26	3.27	2
noop	0.038	1	1	1

energies to execute, and both required significantly more energy than all other families of instructions. Simulation also showed the extra energy required to execute absolute stores when compared to relative stores although this was not evident from the load absolute and relative energies. The same held for branch taken compared to branch not taken (the WIMS architecture assumes branches are not taken and so must flush the pipeline for taken branches), and to a lesser degree for the jmp family of instructions.

On average, the normalized EPI from simulations fell within 30% of the normalized hardware EPI. There was substantial error in some of the simulated results, however. For example, returns, software interrupts, load relative, store relative, jump relative, and jump relative to subroutine all displayed 40% or more error in either direction. It is worth noting that most of these outliers incorporate relative addressing, a phenomenon which could indicate, for example, that a block of transistors in the memory controller are difficult to simulate both accurately and efficiently. It is also possible that software testing may need to be more extensive, or that fewer instruction types should be included in these tests to get better accuracy. Excluding these outliers, the simulation EPI results improved to within 16% of the hardware numbers.

As accuracy and runtimes improve, energy simulations will be increasingly valuable for chip and system design and energy-aware compiler support. During the processor design phase, the circuit may be simulated for functionality, performance, and energy to address a growing concern across industry with energy consumption. Using this methodology with post-layout simulations, instruction energies can be estimated and used to perform late stage power simulations to verify that the design satisfies the required power specification prior to fabrication.

Block transfer instructions

Energy was measured during tests transferring between 1 and 32 16-byte chunks of data using either the new block transfer instruction or traditional load/store instructions.

These measurements were normalized to the number of chunks being transferred. Fig. 2.3 shows the difference in energy per transferred chunk as a function of the number of chunks being transferred. These results show that for small amounts of data, a combination of loads and stores was more efficient than the block transfer (negative value in Fig. 2.3). However, beginning at just 32 bytes, the block transfer became increasingly more efficient than the load/store operations. The positive-sloping trend evident in Fig. 2.3 indicates the growing efficiency of the block transfer instruction as more data is being transferred. This result is not surprising, since the block-transfer overhead becomes less significant compared to the memory copy operation.

In the case of saving register state to the scratchpad memory, the block transfer required 44% less energy than the load/store equivalent. Additionally, the average current for the block transfer instruction was 5% lower.

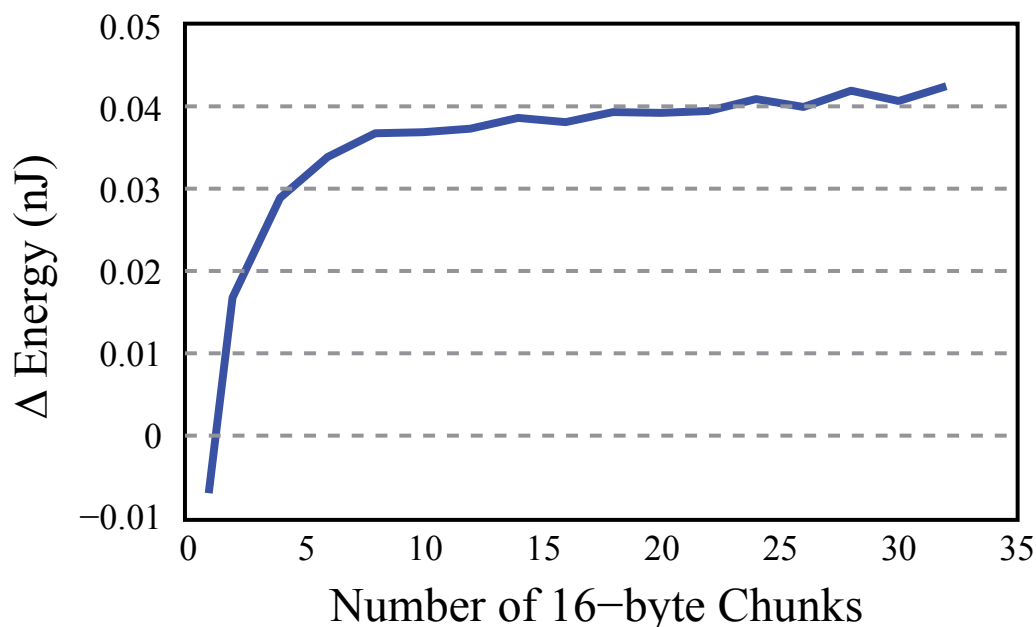


Fig. 2.3. Comparison of energy used by block-transfer and load/store instructions. This figure shows the difference between the energy used by block-transfer instructions and traditional load/store instructions to transfer one data chunk, when the total number of chunks transferred ranges from 1 to 32. A single data “chunk” is a 16-byte block of data; 32 chunks represent 512 bytes of data. Measurements were normalized to the number of chunks being transferred.

Discussion

Apart from the insights into single-instruction efficiencies that are common to many embedded architectures, several key findings of this investigation will directly influence both the software design and hardware considerations of a final system. For instance, the most efficient method of transferring data was to transfer the largest possible amount of data using the block transfer instruction. Hence, signal processing hardware should likely be designed to fill large blocks of memory before data are transferred elsewhere for continued analysis or wireless transmission.

It is important to note two fringe benefits of the block transfer instructions beyond the energy savings. In the first case, saving instructions fetched and decoded may also save storage space, depending on loops and branches. With no loops, transferring 512 bytes from scratchpad to SRAM would require 520 instructions (eight for initialization plus two per 16-bit word), whereas the block transfer could accomplish the same task in 15 instructions. If such a task were written in a loop, it would require constant checking of a counter in a data register, or updating an address register. In either case, the number of instructions might be equivalent between the two options, but with looping overhead built into the hardware implementation of the block transfer instruction, the new instruction will still be more power efficient than the looping alternative.

In the second case, the time to execute is reduced considerably for the block transfer instruction. When copying 512 bytes, the block transfer finishes 9% sooner than the load-store alternative. When storing register values to memory, the block transfer finishes 41% faster. In an embedded system with realtime processing deadlines, such time savings can be significant.

Finally, a particularly interesting result of this investigation is an understanding of the energy consequences of choosing a larger address register width than the datapath width. Although energy savings from fewer fetch and decode operations likely account for significant savings, much of the inefficiency of the load-store sequences comes from

the need to perform transfers in two steps of 16 and 8 bits each—and perhaps even more importantly, that the transfer requires copying the data to a 16-bit data register before storing to memory. A 24-bit address register store instruction would likely narrow the energy gap between block transfer and load-store alternatives. However, an address register store instruction may have little use other than saving state to the scratchpad memory. Under this consideration, the benefits of the additional address space for external flash memory could be a crucial factor in justifying the disparate address and data widths.

Conclusion

Specific contributions of this dissertation include an analysis of the energy profile of the third-generation WIMS microcontroller fabricated in IBM 65nm CMOS technology and the addition of a new instruction family which allows efficient loading and storing of large amounts of data. Collaborative efforts include significant contributions to the overall tapeout and test of the WIMS microcontroller. In its target environment, the microcontroller must be able to operate efficiently over large amounts of incoming and outgoing data. To that end, the energies required to execute single instructions have been characterized in an effort to find energy-conserving programming techniques. Additionally, the energy savings of a new family of instructions designed to efficiently move large blocks of data between the low-power scratchpad memory, registers, and standard SRAM were investigated. These block-transfer instructions were the most efficient way to copy large amounts of data in the WIMS ISA, with improvements in energy that reflected both less power and faster completion. These techniques reflect system-level features which will help to improve the efficiency of systems, like BCIs, which must process large amounts of data with little power. By designing energy-efficient hardware and software, these systems will be able to operate robustly within the limited energy confines of the neural environment.

References

- [1] E. D. Marsman, R. M. Senger, G. A. Carichner, S. Kubba, M. S. McCorquodale, and R. B. Brown, "DSP architecture for cochlear implants," in *Proc. IEEE Int. Symp. Circuits and Systems*, 2006, pp. 657-660.
- [2] R. M. Senger, E. D. Marsman, M. S. McCorquodale, and R. B. Brown, "A 16-bit, low-power microsystem with monolithic MEMS-LC clocking," in *Proc. Asia South Pacific Design Automat. Conf.*, Yokohama, Japan, 2006.
- [3] A. P. Chandrakasan and R. W. Brodersen, "Minimizing power consumption in digital CMOS circuits," *Proc. IEEE*, vol. 83, pp. 498-523, 1995.
- [4] A. P. Chandrakasan, S. Sheng, and R. W. Brodersen, "Low-power CMOS digital design," *IEEE J. Solid-State Circuits*, vol. 27, pp. 473-484, 1992.
- [5] B. Davari, R. H. Dennard, and G. G. Shahidi, "CMOS scaling for high performance and low power-the next ten years," *Proc. IEEE*, vol. 83, pp. 595-606, 1995.
- [6] R. S. Chau, "Intel's breakthrough in high-K gate dielectric drives Moore's law well into the future," *Technology@Intel*, 2004, pp. 1-7.
- [7] B. S. Doyle, S. Datta, M. Doczy, S. Harelund, B. Jin, J. Kavalieros, T. Linton, A. Murthy, R. Rios, and R. Chau, "High performance fully-depleted tri-gate CMOS transistors," *IEEE Electron Device Lett.*, vol. 24, pp. 263-265, 2003.
- [8] J. W. Tschanz, J. T. Kao, S. G. Narendra, R. Nair, D. A. Antoniadis, A. P. Chandrakasan, and V. De, "Adaptive body bias for reducing impacts of die-to-die and within-die parameter variations on microprocessor frequency and leakage," *IEEE J. Solid-State Circuits*, vol. 37, pp. 1396-1402, 2002.
- [9] C. H. Kim and K. Roy, "Dynamic VTH scaling scheme for active leakage power reduction," in *Proc. Design, Automation and Test Europe Conf. Exhib.*, 2002, pp. 163-167.
- [10] L. Hai, S. Bhunia, Y. Chen, T. N. Vijaykumar, and K. Roy, "Deterministic clock gating for microprocessor power reduction," in *Proc. Int. Symp. High-Performance Computer Architecture*, 2003, pp. 113-122.
- [11] G. Magklis, G. Semeraro, D. H. Albonesi, S. G. Dropsho, S. Dwarkadas, and M. L. Scott, "Dynamic frequency and voltage scaling for a multiple-clock-domain microprocessor," *IEEE Micro*, vol. 23, pp. 62-68, 2003.
- [12] R. Kumar, K. I. Farkas, N. P. Jouppi, P. Ranganathan, and D. M. Tullsen, "Single-ISA heterogeneous multi-core architectures: the potential for processor power reduction," in *Proc. IEEE/ACM Int. Symp. Microarchitecture*, 2003, pp. 81-92.

- [13] V. Tiwari, S. Malik, A. Wolfe, and M. Tien-Chien Lee, "Instruction level power analysis and optimization of software," *J. VLSI Signal Process.*, vol. 13, pp. 223-238, 1996.
- [14] R. A. Ravindran, R. M. Senger, E. D. Marsman, G. S. Dasika, M. R. Guthaus, S. A. Mahlke, and R. B. Brown, "Increasing the number of effective registers in a low-power processor using a windowed register file," in *Proc. Int. Conf. Compilers, Architecture Synthesis for Embedded Systems*, San Jose, CA, 2003.
- [15] R. A. Ravindran, P. D. Nagarkar, G. S. Dasika, E. D. Marsman, R. M. Senger, S. A. Mahlke, and R. B. Brown, "Compiler managed dynamic instruction placement in a low-power code cache," in *Proc. Int. Symp. Code Generation Optimization*, 2005, pp. 179-190.
- [16] B. Redd, S. Kellis, N. Gaskin, and R. Brown, "Scratchpad memories in the context of process scaling," in *Proc. IEEE Int. Midwest Symp. Circuits and Systems*, 2011, pp. 1-4.
- [17] R. M. Senger, E. D. Marsman, S. Kellis, and R. Brown, "Methodology for instruction level power estimation in pipelined microsystems," in *Austin Conf. Integrated Circuits and Systems*, Austin, TX, 2007.
- [18] S. Kellis, N. Gaskin, B. Redd, J. Campbell, and R. Brown, "Energy profile of a microcontroller for neural prosthetic application," in *Proc. IEEE Int. Symp. Circuits and Systems*, 2010, pp. 3841-3844.

CHAPTER 3

CORTICAL FIELD POTENTIALS

The activity of the cortex may be recorded at a variety of scales and depths—from microelectrodes within the cortex to large magnets far away from the cortex. Selecting an appropriate technology requires balancing a number of trade-offs including clinical responsibility to mitigate risk, signal integrity, cortical coverage, and specificity in time, space, or frequency. For example, EEG may record brain potentials over the entire scalp without any invasive procedure, but with less detail at a given cortical site than a microelectrode penetrating into the cortex to record from single neurons and the extracellular potential around them. Some applications, such as localization of epileptogenic zones, need coverage over large areas of cortex; others, like brain-computer interfaces, depend more on signal integrity and specificity. Understanding the properties of the neural activity at various scales and depths within and outside the skull and cortex is an important step in selecting the appropriate signal and designing the appropriate electrode to capture that signal. This work compares dynamics in space, time, and frequency of cortical field potentials recorded by three types of electrodes: the Utah microelectrode array (MEA), which penetrates the cortex to record single- or multiunit activity (SUA or MUA) and local field potentials (LFP); electrocorticography (ECoG) electrodes, which are used clinically to record electric potentials at the cortical surface; and, micro-ECoG (μ ECoG) electrodes which also record epicortical potentials but with smaller electrodes and finer spacing than standard clinical ECoG grids.

Signals and dynamics

Low-frequency (i.e., <500 Hz) intracortical, extracellular potentials are generated primarily by the sum of excitatory postsynaptic dendritic current sinks and sources near the recording electrode [1-4]. Likewise, electrical potentials at the cortical surface also consist principally of a summation of nearby synaptic dendritic activity [5], and are typically analyzed in the same or similar low-frequency range as LFPs. Neuronal firing activity may bleed into the upper portion of the frequency range of either LFP or surface potentials, though likely with less power and specificity at the surface than within the cortex since the intracortical electrodes are closer to those small-amplitude sources. Because field potentials constitute a summation, synchronized oscillations will sum to larger contributions than phase-offset oscillations [5-7]. Also, since gray matter is a resistive medium [8], there will be little or no capacitive filtering of the fields generated by dendritic currents, and the frequency content of field potentials recorded intracortically should be similar to that recorded epicortically. Thus, for example, modulation of power in the gamma band (i.e., 30-80 Hz) should appear in both LFPs and surface potentials. However, the properties of electric fields would suggest that with increasing distance between the source and electrode, electric potentials will be smaller in magnitude and more diffuse in space.

In addition to passive propagation through the extracellular space, active processing by cortical circuits will play a role in defining spatiotemporal properties of field potentials. Synchronized oscillations are a fundamental property of the brain's processing mechanisms [2, 9-12]. Temporally and spatially transient binding between and within populations of neurons will be reflected in dynamic and distributed correlations across cortex, if the signals are recorded with enough resolution in space and time. In some areas of the brain, for example striate cortex, neurons with similar processing preferences have been shown to organize in cortical columns with diameters in the range of several hundred microns [10, 13]. Interactions both within and between columns in visual cortex have demonstrated dynamic spatiotemporal patterns which are thought to represent the binding of features

for cortical processing [2, 9-12, 14, 15]. Similar types of neuronal assemblies have been demonstrated in other areas of cortex [16, 17], and subcentimeter organization has been observed in still other areas [18]. These assemblies comprise mesoscopic building blocks of cortical information processing and establish a lower limit on the spatial extent of cortical field potentials on the order of a few hundred microns. The physical manifestation of neuronal organization will also influence the nature of the matter through which the signals propagate and so affect passive spread.

The spatial extent of LFP has been characterized in a number of studies reporting a wide range of values, from a few hundred microns [19-21] to a millimeter or more [2, 15, 22, 23]. These disparate results reflect the complexity inherent in continuous fields produced by the massive, intricate network of electrical sources and pathways in the cortex, and the complex way in which these elements interact to produce coherent outputs from myriad sensory and cognitive inputs. Indeed, the spatial properties of cortical field potentials have been shown to depend on frequency [12, 20, 22, 24, 25], brain state [25], the nature of stimuli [15] and behavior [26], across cortical layers [21], anatomical location [27], between subjects [27], and perhaps even genetic or environmental differences [27].

Although the relationship between LFPs and ECoG is not entirely understood, similar underpinnings suggest that some of their information content may be similar and that some aspects of their dynamic scale may be similar. In terms of the continuous fields, the principal advantage of intracortical LFP versus subdural ECoG has been better specificity of the intracortical field potentials; however, that comparison has typically been made with ECoG recorded on relatively large electrodes. The discrepancy in electrode size is an important distinction, since broader synchronization would be required to effect change in the summed potential of larger neuronal populations integrated by the larger electrodes [6, 7]. A commonly stated estimate of the population size underneath a standard ECoG electrode figures that, with 2.3 mm exposed diameter and an average density of 10^5 neurons/mm² in the human cortex, several hundred thousand to a few million neurons

contribute to the electric potential at a single ECoG electrode. By that same logic, a small electrode 0.1 mm in diameter would rest over many fewer neurons. While these back-of-the-envelope estimates are simplistic in their view of cortical geometry and operation, their results illustrate how different the surface potential could be if it were recorded with electrodes of different sizes [6, 28, 29].

There is strong evidence of fine spatial and temporal dynamics in surface potentials [30-37]. Studies of electrocorticograms recorded by microelectrodes have demonstrated distinct spatial patterns within grids less than 1 cm² in area [38, 39]. Coherence, a measure of correlation as a function of frequency, was found to decline with distance and frequency although abrupt changes were found even among nearest neighbors (within 5-10 mm) and over short timescales (5-15 sec), and the distribution of coherence at any given separation distance could be large [27, 32, 35]. Coherence has been shown to differentiate function or state [32, 40], pathological tissue [36], anatomical location [37] and cognitive tasks [37]. This growing body of work suggests that surface potentials may have better spatial and temporal resolution than has previously been available with grids of large electrodes. Recording at the appropriate spatial scale may therefore reveal fine-scale dynamics even at the surface of the cortex.

Electrodes

In the modern clinical setting, cortical surface potentials are typically recorded with grids of platinum disks, each 4 mm in diameter with 2.3 mm exposed surface diameter, with 1 cm pitch (e.g., Fig. 3.1, silver disks in right panel). The first ECoG electrodes were designed by Penfield and Jasper in the 1950s for the treatment of intractable epilepsy [41]. Then, as now, ECoG electrodes were placed on the surface of the brain to discover epileptogenic zones of cortex prior to surgical resection. Since epilepsy in particular is a pathology which may recruit large networks of cortical tissue, the size and spacing of clinical ECoG electrodes are appropriately scaled to cover more of the cortex. For applications

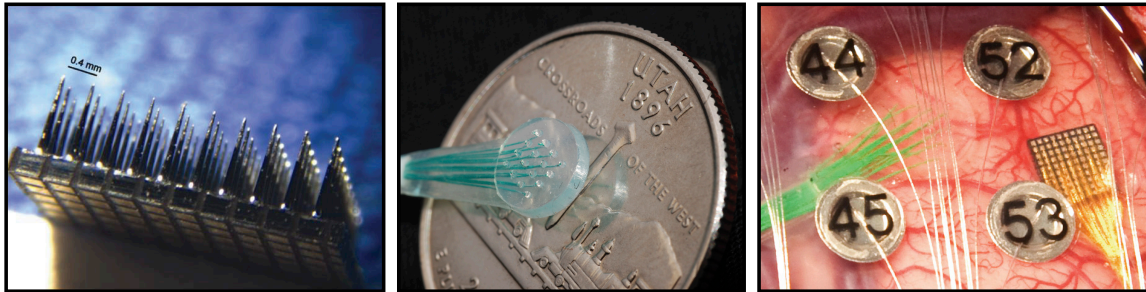


Fig. 3.1. The devices used to record neural activity for this study. (Left) Photograph of the Utah Electrode Array; (Middle) Photograph of nonpenetrating microwire grid; (Right) Utah Electrode Array (gold wires leading to brown square) and nonpenetrating microwire grid (green wires leading to translucent circle) shown implanted alongside standard electrocorticographic (ECoG) electrodes (silver disks with numbers overlaid).

which require more detailed information about activity within cortical functional domains, clinical ECoG electrodes may not be the ideal selection. Still, clinical ECoG electrodes have been in use for more than five decades, their behavior under both recording and stimulating paradigms is well understood and widely accepted by clinicians, and they have been used successfully in brain-computer interfaces [42-45].

A variety of options exist to record neural activity at smaller scales both at the cortical surface and from within the cortex. Nonpenetrating microwire grids, also referred to as micro-ECoG or μ ECoG grids, consisting of platinum microwires terminated to form a grid of contacts, have been used recently in a number of studies [38, 39, 46, 47] (Fig. 3.1, middle panel). The diameter of the microwire is typically less than 100 μ m, and the grid pitch is typically less than 3 millimeters. μ ECoG grids are available from commercial manufacturers with FDA approvals for use in human subjects. For equal wire budgets, μ ECoG grids cover far less cortical surface than clinical ECoG grids. Because the exposed area of a microwire is much smaller than that of a macro ECoG electrode, it will record from a smaller volume of cortex, and hence may be considered a more locally derived signal than standard ECoG.

The Utah MEA is one of only a few methods approved by the FDA to record intracortical brain activity in human subjects [48-50] (Fig. 3.1, left panel). It consists of a 10x10 grid of platinum-tipped silicon electrodes rising 1.5 mm out of a 4x4 mm base

(400 μm pitch). Each electrode's tip is approximately 4 μm in diameter. These arrays are inserted so that the electrode tips impale the cortex to record the spiking activity of neurons as well as continuous LFPs within the cortex. Intracortical LFP recorded at this scale is a modern standard for recording continuous brain activity with high integrity and specificity in both space and time, although the area covered is necessarily small.

Cortical field potentials were recorded from human subjects using clinical ECoG and μECoG electrodes and the Utah MEA. These data were explored to better understand the nature of the field potentials recorded at different scales and depths. In particular, cortical field potentials recorded by microelectrodes at the cortical surface were examined to determine whether they might reflect high signal integrity and good specificity in space and time. Linear relationships in the data were estimated by averaging over substantial amounts of time in order to elicit the persistent relationships; however, distributions contributing to these averages were also examined to understand the variability of the linear relationships. Signals tended to be more highly correlated the closer they were in space and time, and in the lower frequencies. Furthermore, surface potentials could be recorded with similar specificity as field potentials recorded intracortically. This work represents the first study of its kind to systematically compare the dynamics in space, time, and frequency of intracortical LFPs and subdural ECoG and μECoG in humans.

Methods

Implant, recording, and data selection

All subjects in this study required surgical intervention to treat intractable epilepsy, and gave informed consent for their participation in an institution review board-approved study. Two 4x4 channel μECoG grids (Table 3.1, SM1 and SM2) with 75- μm electrodes and 1-mm pitch were implanted in one male patient over the arm and the hand areas of M1. Clinical need mandated the relocation of the macro-ECoG after several days' implantation, so the μECoG grids were moved to the face area of M1 and Wernicke's area (Table 3.1,

Table 3.1. Listing of subjects and grid types.

Label	Type	Channels (used)	Implant type	Cortical region	Institution
SC	ECoG	64 (63)	Subdural	Left hemisphere	U of WA
SM1	μ ECoG	16 (16)	Subdural	M1 arm	U of UT
SM2	μ ECoG	16 (13)	Subdural	M1 hand	U of UT
SM3	μ ECoG	16 (14)	Subdural	M1 face	U of UT
SM4	μ ECoG	16 (11)	Subdural	Wernicke's area	U of UT
UA1	Utah MEA	96 (87)	Intracortical	Right Temporal lobe	U of UT
UA2	Utah MEA	96 (88)	Intracortical	Left Temporal lobe	U of UT

SM3 and SM4) (Fig. 3.2, right panel). In two other male patients, 96-channel Utah MEAs were implanted in the right temporal lobe (Table 3.1, UA1; Fig. 3.2, left panel) and left temporal lobe (Table 3.1, UA2; Fig. 3.2, middle panel). The UA implant sites were regions of cortex targeted for subsequent resection. Data provided by the University of Washington were recorded from an 8x8-channel clinical ECoG grid, with standard 2.3 mm exposed electrode area and 1-cm spacing (Table 3.1, SC).

Data from the subdural SM and UA grids were amplified, bandpass filtered (single-pole Butterworth high pass filter at 0.3 Hz, and three-pole Butterworth low pass filter at 7500 Hz), and digitized at 30,000 samples per second (Cerebus, Blackrock Microsystems, SLC, UT). Data from the clinical SC grid were amplified and bandpass filtered, then digitized at 1,000 samples per second. The SM data were recorded against the clinical reference, located several centimeters away in the epidural space. The UA data were referenced to 2 cm exposed length of low-impedance wire which was either in the subdural or epidural space.

For the SM and UA datasets, 1800 sec of continuous data were selected by hand, based on criteria of minimum artifact and pathology, for further analysis. For SC, 1000 sec of data were selected by the same criteria. For the UA grids, the clinical video feed was reviewed to ensure that the patient was awake and behaving naturally (although all patients were confined to the hospital beds while in the Neurocritical Care Unit); otherwise, the

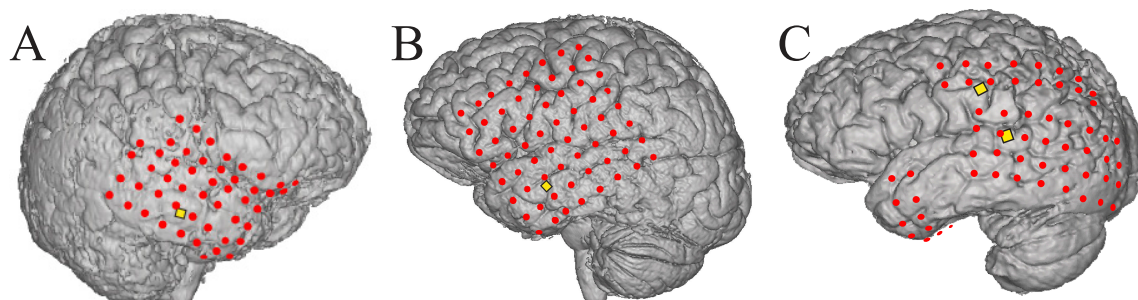


Fig. 3.2. Locations of the electrode grids. (A) Yellow square indicates position of UA1; (B) Yellow square indicates position of UA2; (C) Yellow squares indicate positions of SM3 and SM4 (SM1 and SM2 were implanted in the same patient over arm and hand area of primary motor cortex).

data were selected from recordings between the hours of 10am and 6pm to maximize the likelihood of awake natural behavior. Each channel of data from each grid was reviewed manually and discarded if it exhibited significant artifact (Table 3.1 indicates how many channels were used from each grid).

Preprocessing

Prior to analysis, the SM and UA data were low pass filtered with cutoff frequency at 400 Hz (Butterworth filter with 7 second-order sections for 30 kS/sec data) then downsampled to 1,000 samples per second. Due to contamination from line noise, the data were further filtered to attenuate narrow bands at 60 Hz and harmonics through 480 Hz. All filtering was performed both in the forward and reverse directions so that the phase of the signals was left unchanged from the original signal.

It was sometimes useful to identify statistical outliers. Given the 75th percentile Q_3 and the 25th percentile Q_1 , and the interquartile range $IQ=Q_3-Q_1$ between them, lower and upper fences were defined to bound the statistical inliers

$$Q_1 - 1.5 * IQ < x < Q_3 + 1.5 * IQ \quad (3.1)$$

If a point fell outside these fences, it was considered a statistical outlier [51]. These boundaries would correspond approximately to $\pm 2.7\sigma$ if the data were normally distributed with standard deviation σ .

Correlation functions

Correlation measures linear similarity between two sets of data. When the data represent samples in time, correlations can be calculated for a range of lags between the two datasets to explore temporal dynamics in their similarity. If the two time series are identical, the measure is called the autocorrelation function (ACF); otherwise, it is called

the cross-correlation function (CCF). Correlation is not a direct function of frequency, although if two signals oscillate similarly, their cross-correlation will be high. Thus, correlation is useful for determining the transient dynamics of broadband activity, and was used to explore both temporal and spatial relationships in the neural data.

Correlation functions were estimated for all possible two-channel permutations (including autocorrelation). For two time series x and y with means μ and standard deviations σ , the normalized correlation coefficient ρ_{xy} between them was calculated over a range of lags m as

$$\rho_{xy}(m) = \frac{\sum_{n=0}^{N-|m|-1} (x_{n+m} - \mu_x)(y_n - \mu_y)}{\sigma_x \sigma_y} \quad (3.2)$$

These calculations were performed for nonoverlapping 4-second data segments, for lags between -4 seconds and +4 seconds, and in time increments of 1 msec. For each channel pair, the CCF was estimated by averaging the results of all 4-sec segments.

The full-duration at half maximum (FDHM) of a waveform is a measure of how quickly the waveform declines from a central peak to minimum values in the tails. FDHMs of the ACFs were calculated by finding the length of the line intersecting each ACF at half of its maximum height, i.e., at $\rho = 0.5$. This quantity was calculated for each 4-sec segment of data. If the FDHM of more than half the channels for any given data segment were considered statistical outliers, that segment was not included in further analysis. Baseline values for the correlation functions were calculated as the average correlation between $m = 3.5$ sec and $m = 4.0$ sec.

Zero-lag correlations averaged over channel pairs at each unique separation distance and across all segments were calculated to form estimates of correlation versus distance. The total population being averaged thus varied over two dimensions: multiple channel pairs at each separation (i.e., variation in space), and multiple nonoverlapping

data segments (i.e., variation in time). By averaging over channel pairs and leaving the full set of values across data segments, the variation in time could be presented. Similarly, by averaging over time and leaving the full set of channel pairs at each separation, the variation in space could be presented. Each of these approaches was used in order to demonstrate variability in the distribution of correlation versus distance over space and time. Separately, zero-lag correlation between each pair of channels was also calculated using all data simultaneously (1000 sec for SC; 1800 for all other grids) to investigate long-term spatial relationships.

In two-dimensional Euclidean space, the vector between the Cartesian coordinates of two channels has magnitude (i.e., separation distance) and angle. With 0° selected arbitrarily as the line $y = 0$ in the grid of electrodes, zero-lag correlations were further refined to average over unique separation distances at 0° , 45° , 90° , and 135° relative to the horizontal axis. For example, all channel pairs whose vector was parallel to the 45° grid diagonal were incorporated into an estimate of correlation versus distance at that orientation. In this way, directional anisotropy could be explored in the relationships between correlation and distance.

Frequency analysis

Coherence is a measure of the linear relationships between two time series as a function of frequency. As the correlation function is to time-domain relationships, coherence is to frequency-domain relationships; indeed, the cross power spectrum, which is normalized by the power spectra to give the coherence, may be calculated as the Fourier transform of the cross-correlation function of the two time series (if the two time series are equal, this property simplifies to the Wiener-Khinchin theorem which defines the relationship between the auto-correlation and power spectral density). True coherence may be a complex term with both magnitude and phase; in this case, the magnitude indicates the strength of the relationship and the phase is indicative of a time delay in the coupling.

For two time series $x_1(t)$ and $x_2(t)$, given estimates of their power spectra $S_1(f)$ and $S_2(f)$, and where $*$ denotes complex conjugation, the coherence between them is given by:

$$C_{1,2}(f) = \frac{S_1^*(f)S_2(f)}{\sqrt{S_1^*(f)S_1(f)}\sqrt{S_2^*(f)S_2(f)}} \quad (3.3)$$

This relationship normalizes the cross power spectral density (PSD) by the individual PSDs, and provides a measure of the correlation between the two signals in each frequency band. Often, only the magnitude of the coherence, $|C_{1,2}(f)|$, or its square, are reported. Like normalized correlation, coherence is bounded above by 1 and below by 0.

To estimate coherence, each data set was divided into 450 segments of 4,000 samples each (250 segments for SC). The Chronux package (<http://chronux.org>) [52] was used to calculate multitaper estimates of the spectra, with a time-bandwidth parameter of 3, 5 tapers, 4096-point FFTs, and set to average over all segments. These results were further averaged over all channel pairs at each unique separation distance, to form an estimate of coherence as a function of both frequency and separation. Then, for each frequency, an interpolating spline was fit to the sparsely sampled coherence versus distance points, and the half-height was calculated as the level of coherence midway between the maximum and minimum coherence. The half-height decay (HHD) was found as the separation distance (in the spline-interpolated sequence) at which the half-height level of coherence was achieved.

In some cases, it was convenient to report the average coherence within one of the standard electroencephalographic frequency bands, e.g., the gamma band between 30-80 Hz. In these situations, the coherence was directly averaged over these frequencies. Otherwise, to allow for enough white space in figures to make out form and structure, coherence at single frequencies distributed (linearly or with log spacing) throughout the range of frequencies between 0 and 400 Hz were selected for display.

Software re-referencing

To explore the effects of re-referencing the signals in software, the common average of all channels in a grid (except those channels labeled as bad channels) was found at each sample, and subtracted from each channel. This technique, often called common average re-referencing (CAR), attenuates global elements in the signals and allows local, differential activity to show up more distinctly across channels.

Results

Correlations

Correlations estimated from data recorded with each grid revealed patterns in time and space in the neural signals (Fig. 3.3 and 3.4). The three-dimensional meshes in Fig. 3.3 and 3.4 illustrate correlation as a function of both time and space. The lines in the mesh do not represent averaged data, but individual rows or columns with log spacing (in the case of lag) or linear spacing (for separation distance). Also shown are two-dimensional projections of the three-dimensional mesh onto both the time and space axes, in which color represents the compressed axis. Correlations for each electrode pair were averaged over substantial amounts of time (250 4-sec segments for SC; 450 4-sec segments for all others). The correlations of all electrode pairs at a given separation distance were further averaged to form the estimate of correlation at that separation. The purpose in averaging the data was to elicit persistent relationships in the neural signals. Correlations were strongest for signals close in both space and time, and departure in either dimension resulted in decreasing correlations. Despite this general trend, dynamic activity was also observed in both time and space.

Temporal dynamics

Correlation tended to be largest at all spatial separations for the smallest lags (Fig. 3.3 and 3.4). Likewise, correlation tended to be smallest at all separations for the largest

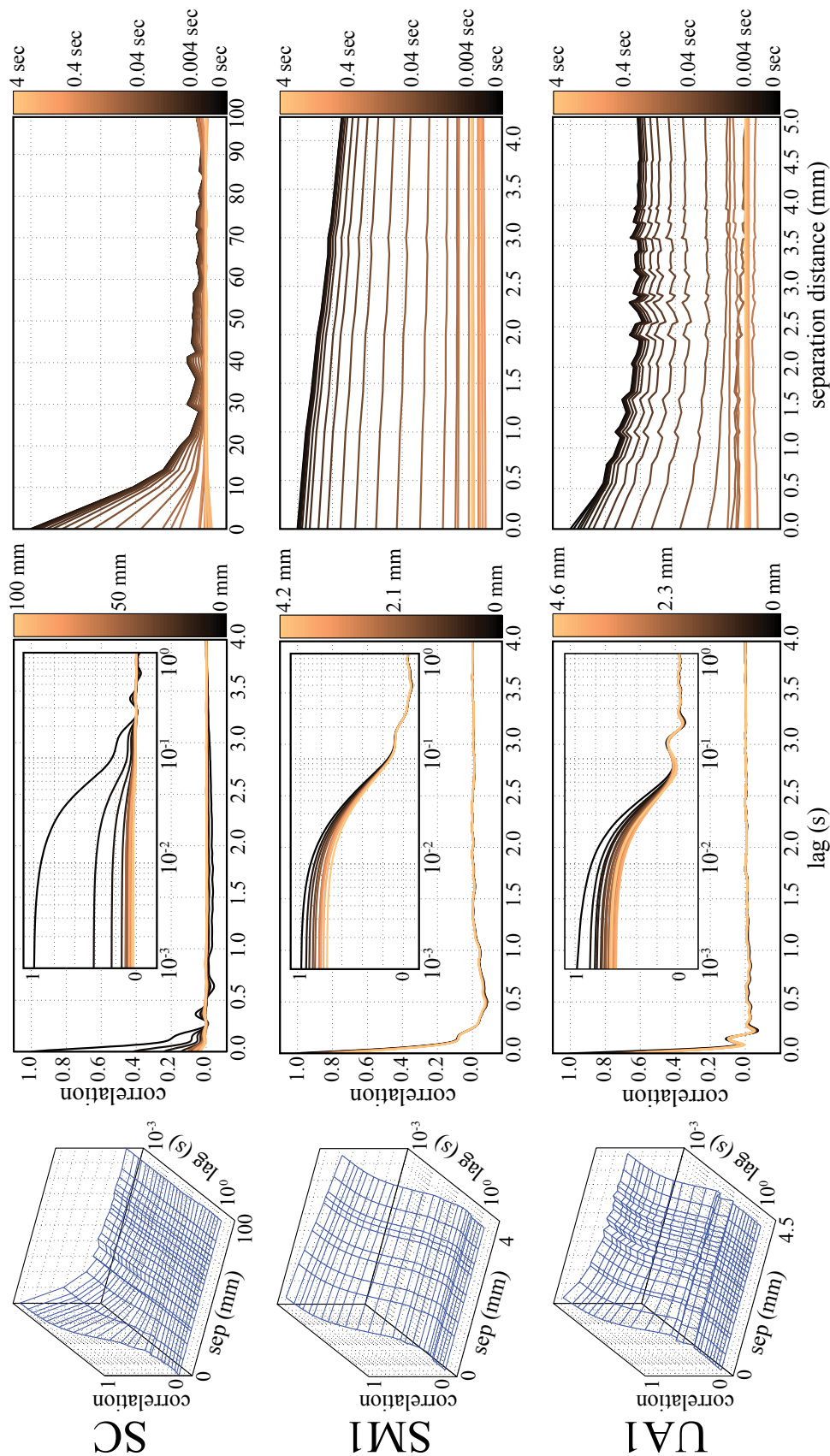


Fig. 3.3. Correlation functions estimated for each grid type. The leftmost panel in each row is a mesh showing the correlation plotted against both separation distance and lag. The middle panel shows correlations plotted against lag, with color representing separation distance. The right panel shows the correlations plotted against separation distance, with color representing lag. The top row shows coherence from the SC grid; the middle row shows correlations from SMI; and the bottom row shows correlations from UAI.

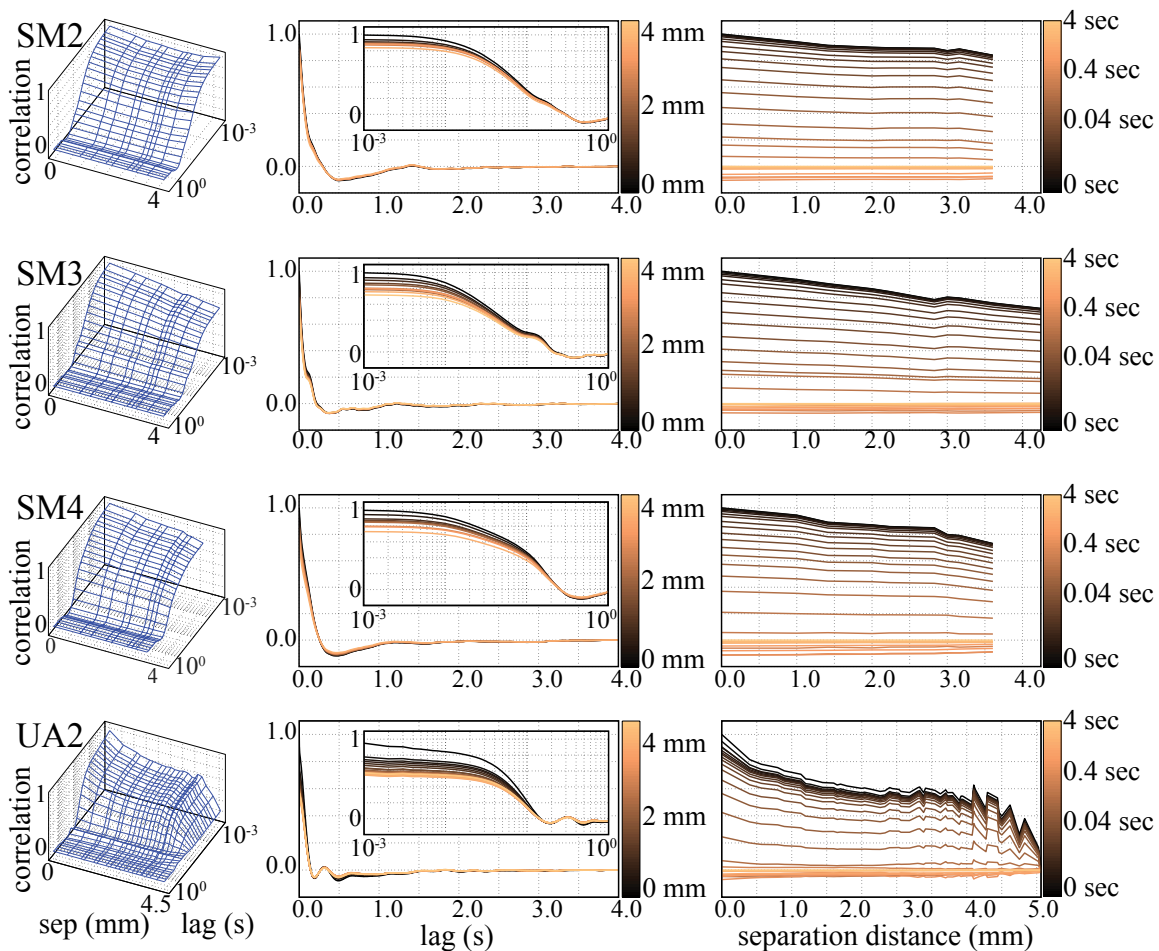


Fig. 3.4. Correlation over space and time for SM2, SM3, SM4, and UA2. The leftmost panel in each row is a mesh showing the correlation plotted against both separation distance and lag. The middle panel shows correlations plotted against lag, with color representing separation distance. The right panel shows the correlations plotted against separation distance, with color representing lag.

lags. The magnitude of the autocorrelation and cross-correlation between 3.5 and 4 sec lag was less than 0.0045 on average across all grids. All of the ACFs (the darkest line in the plots of correlation versus lag in Fig. 3.3 and 3.4) and CCFs (in the same plot, lines ranging from nearly black to orange for increasing separation distance) fell to these baseline values rapidly, i.e., within a few hundred milliseconds.

The initial descent of the ACFs was characterized by calculating the full duration of each channel's ACF (note that only half the ACF is shown in Fig. 3.3 and 3.4) at half its maximum, i.e. the FDHM (Table 3.2). A small value of FDHM would reflect a rapid decline in autocorrelation, thereby suggesting a rapidly changing signal, whereas a large value of FDHM would indicate a more slowly changing signal. On average, the FDHMs of the UA grids were smallest. Three of the four SM grids had FDHMs in the same range as the UA grids; SM4 over Wernicke's area had a larger average FDHM than the other SM grids, but comparable standard deviation. The SC grid had both a larger average FDHM than most of the smaller grids and a larger standard deviation in the FDHM than any of the other grids. Both the mean and standard deviation FDHM values were much larger for UA2 than for UA1; this discrepancy will be addressed in more detail later in this chapter.

To assess how widely the FDHM varied around its average, variability across time and space is illustrated in Fig. 3.5 and 3.6. Panel A in each shows FDHMs over time for each channel (gray) and the average across channels (black). These traces show that in some cases the FDHM changes dramatically over the course of a few seconds (each point represents one 4-sec segment). The SC and UA grids had the largest fluctuations; however, these figures show how different the time course of FDHM could be even for the same electrode types in different patients or anatomical areas.

Table 3.2. Finite-duration at half maximum (FDHM). Results were measured in the autocorrelations of the data recorded by each grid.

	SM1	SM2	SM3	SM4	UA1	UA2	SC
FDHM (msec)	97 ± 4	135 ± 12	97 ± 10	191 ± 7	66 ± 9	129 ± 30	148 ± 55

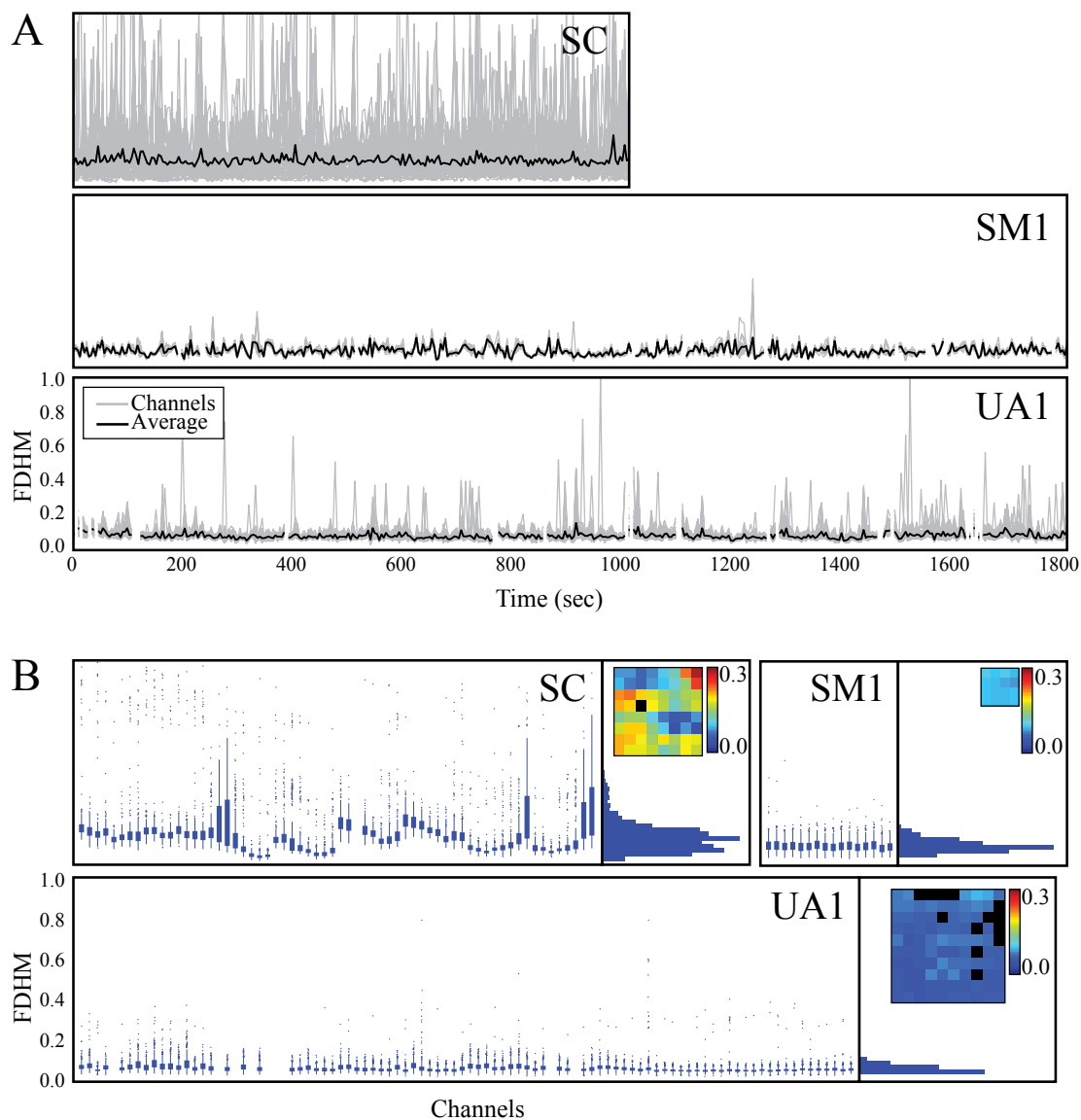


Fig. 3.5. Behavior of FDHM over time and space. Finite-duration at half maximum (FDHM) was measured in autocorrelation functions calculated for consecutive nonoverlapping 4-second segments of data. Panel A shows the time course of FDHM values calculated from all electrodes (gray) and the average FDHM (black) for consecutive nonoverlapping 4-second segments of data from the SC, SM1, and UA1 grids. Panel B shows the distribution of values for each channel, for SC, SM1, and UA1 grids, with the histogram of all values indicated to the right of the boxplot. Inset above the histograms, the average FDHM of each channel is shown in its relative position within the grid, with the color scale indicating the magnitude of the value.

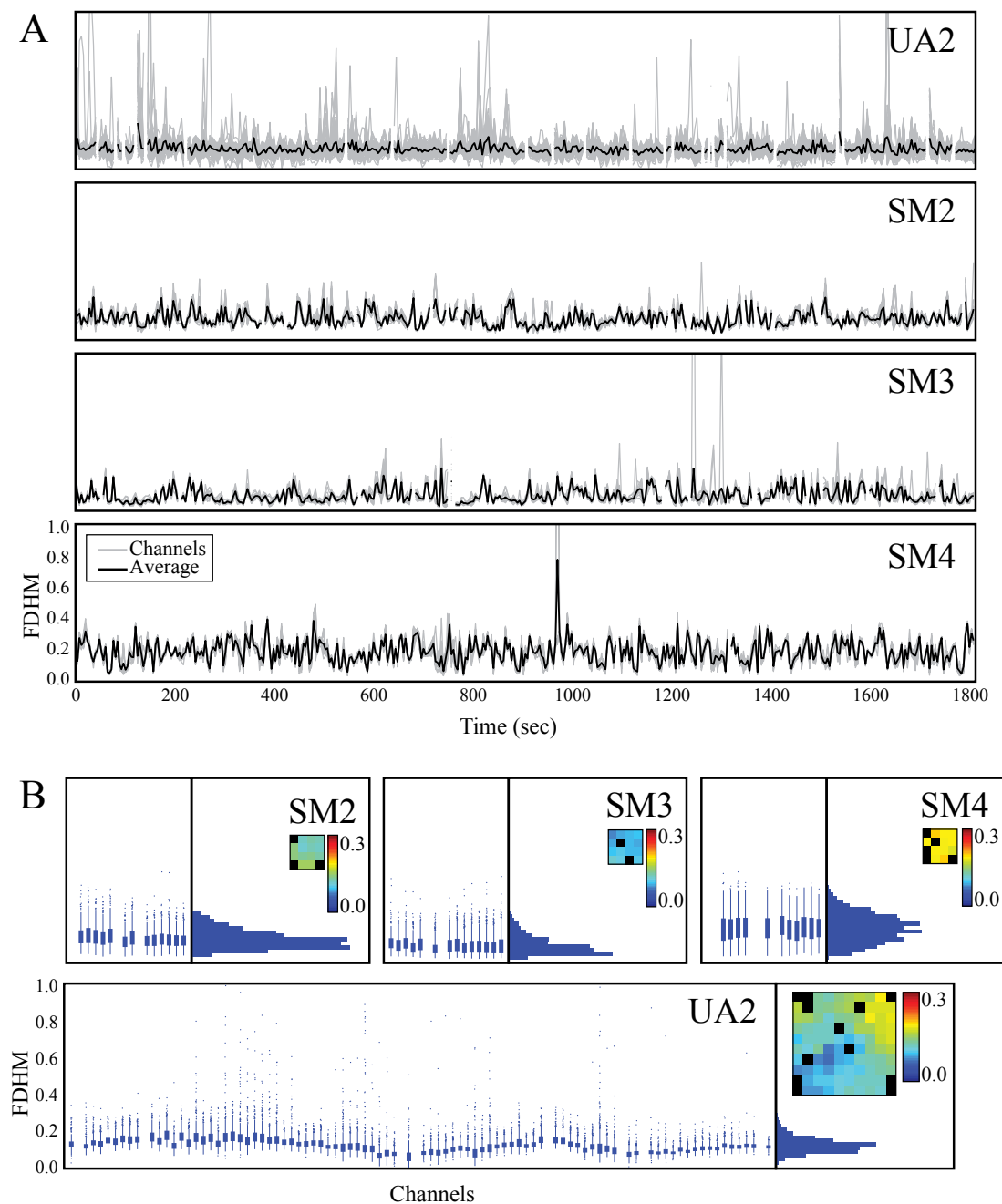


Fig. 3.6. Behavior of FDHM over time and space. Panel A shows the time course of FDHM values calculated from all electrodes (gray) and the average FDHM (black) for consecutive nonoverlapping 4-second segments of data from the UA2, SM2, SM3, and SM4 grids. Panel B shows the distribution of values for each channel, for UA2, SM2, SM3, and SM4 grids, with the histogram of all values indicated to the right of the boxplot. Inset above the histograms, the average FDHM of each channel is shown in its relative position within the grid, with the color scale indicating the magnitude of the value.

Panel B in Fig. 3.5 and 3.6 illustrates distributions of the FDHM over time and space. The histograms represent the full population of FDHMs over both time and channels. Distributions showed a peak at their average value, but were skewed toward larger FDHMs. The SC grid had a wide distribution of FDHMs, although the layout indicated that change tended to occur gradually within grid rows (but could occur abruptly between rows). The SM grids generally had narrow distributions with obvious peaks; the exception was SM4 over Wernicke's area, which had an uncharacteristically wide distribution of FDHM values. UA1 had the tightest distribution over time and smoothly varying spatial patterns across the array.

Spatial dynamics

The correlations revealed a trend of decreasing correlation with increasing separation in all grid types (Fig. 3.3 and 3.4). In some cases, CCFs scaled down with increasing separation until reaching a baseline, after which they did not change substantially with further increases in separation distance. For example, after a few incremental separations (about 30 mm), cross-correlations in the SC grid were negligibly small at all lags. CCFs from the SM grids showed no sign of reaching a baseline correlation by their largest separation, whereas CCFs from the UA grids exhibited an inflection point and subsequent baseline by approximately 2 mm separation. In the supplementary material, there is an uncharacteristically steep decline in the correlation versus distance of UA2; this behavior will be discussed in more detail in a later part of this chapter.

The relationship between correlation and distance is explored in more detail in Fig. 3.7. In that figure, the left plot of Panel A shows correlation versus distance for each dataset used in the study; the right plot shows the same information, but zoomed to the spatial scale of the smaller grids. The slopes of the SC and SM grids were nearly equal over their shared range of separations. The UA grids had a steeper initial slope although the correlations of the two UA grids deviate slightly at the larger separations where fewer channel pairs

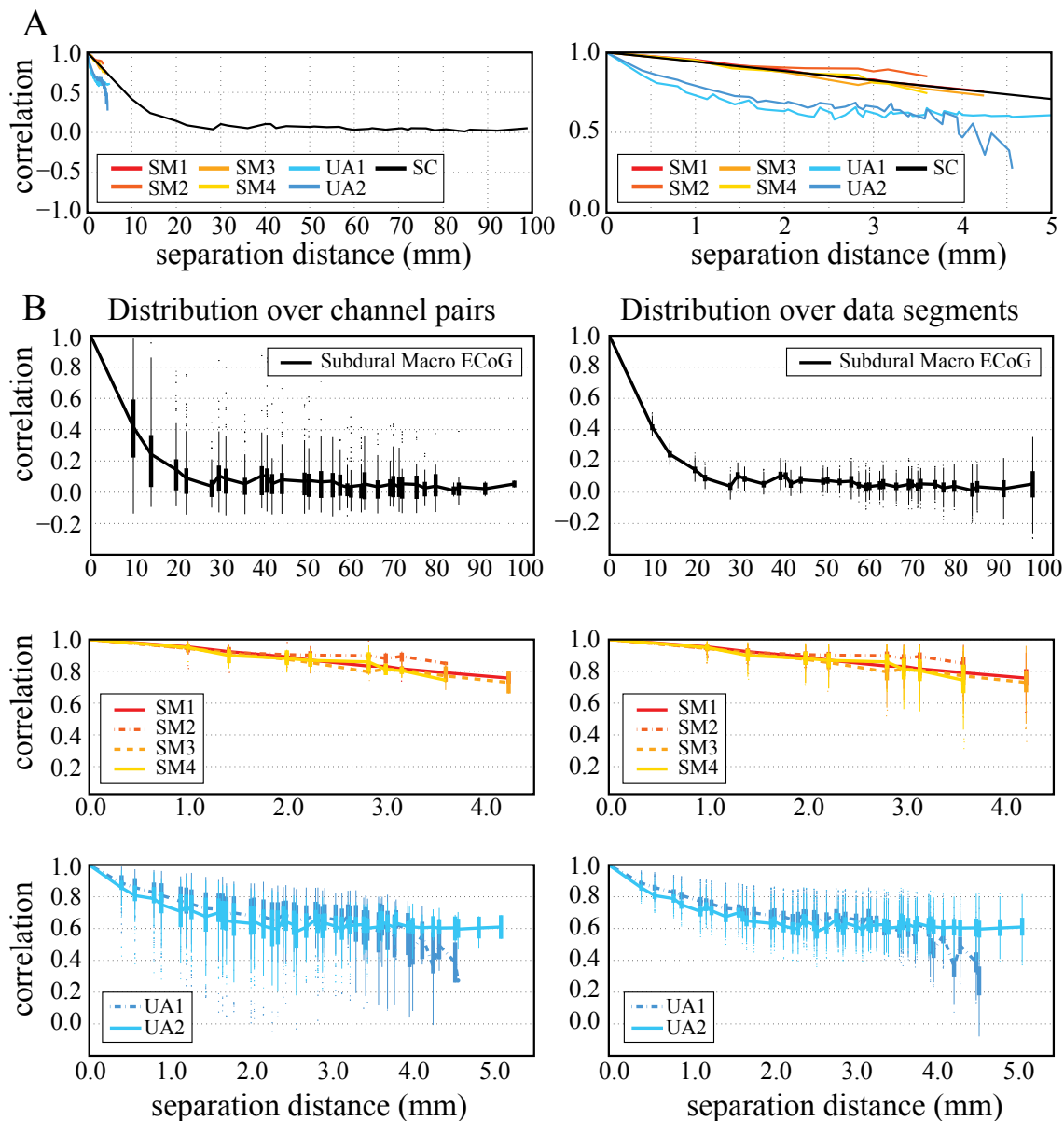


Fig. 3.7. Correlation vs. distance for each grid type. In each of the grids, correlations were measured between all pairs of channels for consecutive nonoverlapping 4-sec segments of data. Colors are consistent through the figure, with black indicating the SC grid; reds, oranges and yellows indicating the SM grids; and blues indicating the UA grids. Panel A shows the average correlation at each unique separation distance separating pairs of channels in each grid. These values include averaging over consecutive segments of data (i.e., averaging over time), as well as averaging over the channel pairs of a given separation distance (i.e., averaging over space). Panel B illustrates the distribution of values at each unique separation distance. Both columns include the average value as a solid thick line. The left column shows the distribution of correlations formed by averaging correlations over time, but leaving correlations between channel pairs unaveraged. The right column shows the distribution of correlations formed by averaging correlations of channel pairs with like separations, but leaving the results over time unaveraged.

contribute to the average. Only the SC grid fell to a negligibly small correlation, about 0.1, and remained there after the inflection point around 30 mm. The UA and SM grids, which include maximum separations of only a few millimeters, demonstrated higher correlations at their largest separations. Particularly in the SM grids, the rate of decay did not flatten out to the same degree as seen in the larger grids, suggesting that the correlation might decline further to a baseline value if the grids were larger. Because two SM grids were implanted several centimeters apart in the same patient, the baseline correlation could be estimated from the correlation between the two grids. Using all 1800 seconds of data simultaneously, the average zero-lag correlation between each channel in SM1 and all channels in SM2, and between SM3 and SM4, was 0.31 ± 0.05 , confirming the notion that the baseline correlation would likely continue to decrease for the SM grids if they were larger.

Panel B of Fig. 3.7 shows the distribution of correlations at each separation distance for each data set. For the left column, correlations were averaged over time, leaving a distribution of correlations across channel pairs for each separation. For the right column, the correlations were averaged over channel pairs at each separation, leaving the distribution of correlations over all 4-sec segments for each separation. In this way, the two columns illustrate distributions over space (left column) and time (right column). Distributions over space were larger than distributions over time for the SC and UA grids; the SM grids had small distributions in both columns. Whereas spatial distributions of correlation grew smaller with increasing separation for all grids, the distribution of correlations over time was largest at the largest separations.

To investigate the nature of correlations between pairs of channel in more detail, the correlation of each channel with all other channels in the same grid are plotted for three example grids in Panel A of Fig. 3.8 and 3.9. These correlations were calculated using the entire time series simultaneously (1000 sec for SC; 1800 sec for all other grids). Here again, the general trend shows decreasing correlation with increasing distance. However, there were some widely separated channel pairs with high correlations; a few examples of this

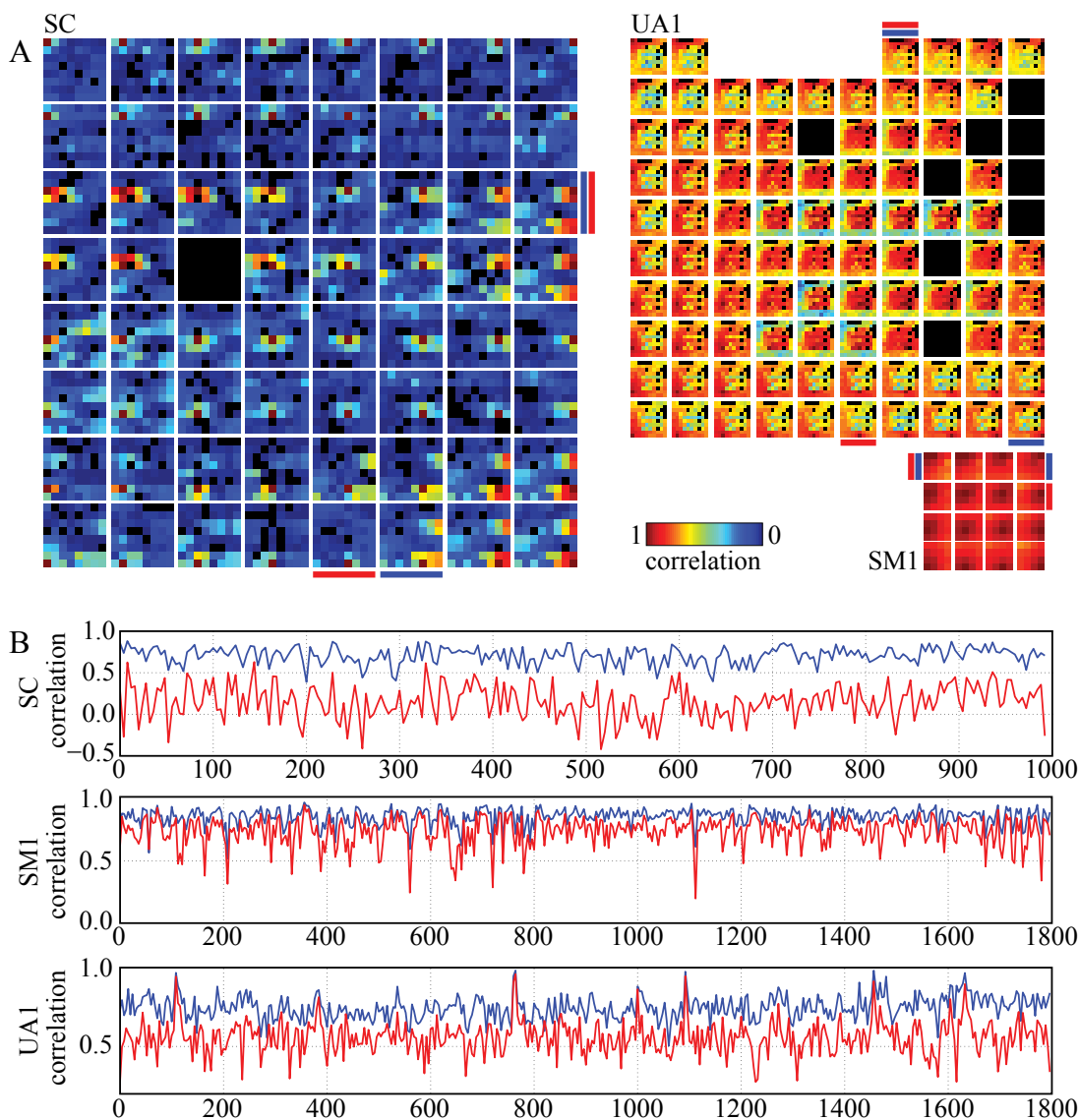
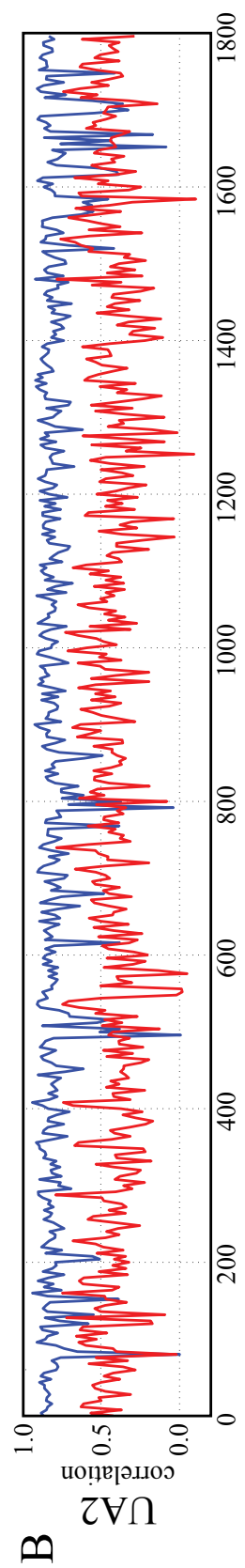
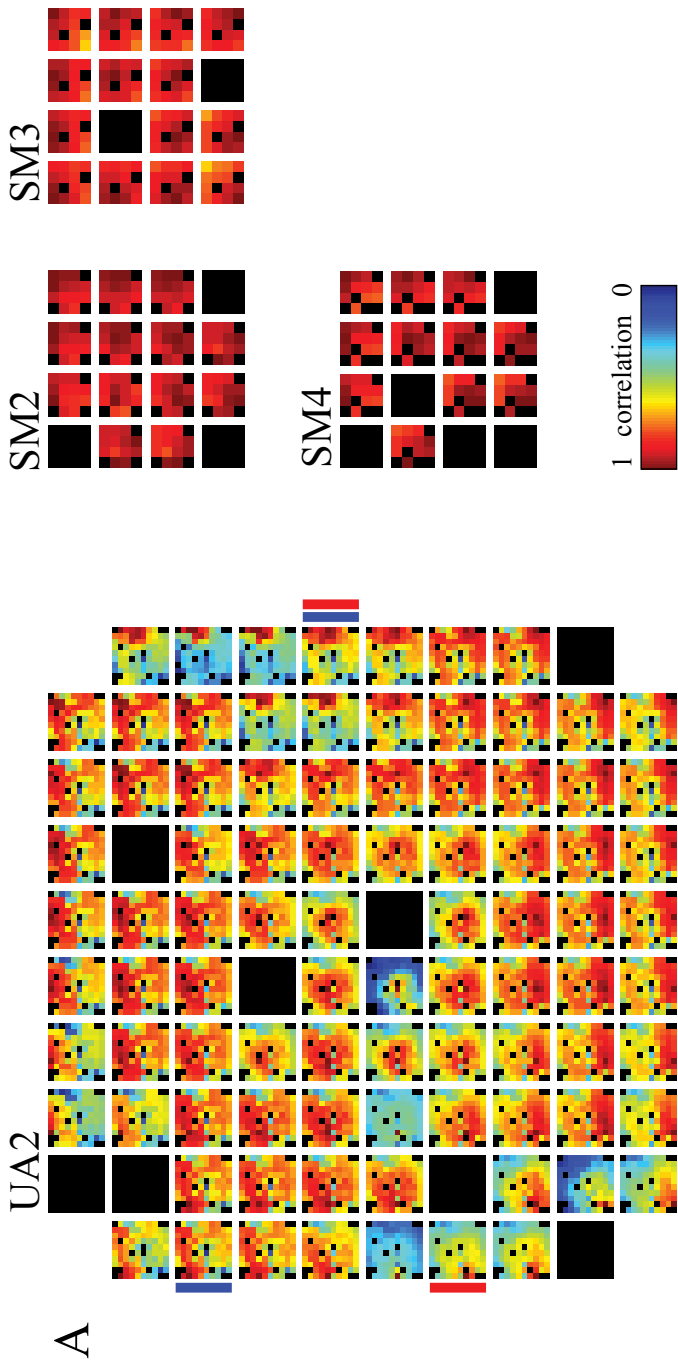


Fig. 3.8. Correlations between electrodes shown spatially. Also shown are examples of the time course of correlation between two electrodes. In Panel A each small square shows the correlation of the electrode at that position in the grid with all other electrodes in the grid. All black squares indicate that the electrode at that position was not included in the analysis. Otherwise, the color indicates the magnitude of the correlation (between 0 and 1). The red and blue bars next to some squares indicate which electrodes were used for the example shown in Panel B. Panel B shows the time course of correlations between two pairs of electrodes in each grid. The red trace shows the correlation between the two electrodes with red bars indicated in Panel A. The blue trace shows the correlation between the two electrodes with blue bars indicated in Panel A. One of the electrodes in each of these pairs was the same (both red and blue bars next to one electrode in Panel A). The other electrodes in each pair were located far from the common electrode, but close to each other (single blue or red bar in Panel A).

Fig. 3.9. Correlations between electrodes shown spatially. Also shown is an example of the time course of correlation between two electrodes. In Panel A each small square shows the correlation of the electrode at that position in the grid with all other electrodes in the grid. All black squares indicate that the electrode at that position was not included in the analysis. Otherwise, the color indicates the magnitude of the correlation (between 0 and 1). The red and blue bars next to some squares indicate which electrodes were used for the example shown in Panel B. Panel B shows the time course of correlations between two pairs of electrodes in each grid. The red trace shows the correlation between the two electrodes with red bars indicated in Panel A. The blue trace shows the correlation between the two electrodes with blue bars indicated in Panel A. One of the electrodes in each of these pairs was the same (both red and blue bars next to one electrode in Panel A). The other electrodes in each pair were located far from the common electrode, but close to each other (single blue or red bar in Panel A).



finding are shown in Panel B of Fig. 3.8 and 3.9: each plot shows two traces representing the correlation over time between two channel pairs. These two pairs have one common channel (indicated by the presence of both blue and red line segments in Panel A). The other channels in the two pairs are far away from the common element but close to each other (indicated by the presence of either the blue or red colored line segment in Panel A). Thus it was possible for high correlations to exist at large separations, but for these high correlations to change quickly as the distant electrode was moved a few millimeters, or as time progressed a few seconds. These findings demonstrate the dynamic nature of correlation at separated cortical sites as well as dynamic nature of correlations over time.

The large range of correlations among channel pairs at a given separation distance prompted the question whether there might be some directional anisotropy in the relationship between correlation and distance. For example, would channels along a horizontal axis exhibit a different relationship between correlation and distance than channels along a vertical axis? The average correlation vs. distance was found for electrodes along the horizontal plane (0°), and at 45° , 90° , and 135° angles (moving counter-clockwise) to the horizontal plane (Fig. 3.10). In the case of the UA2 grid, the 90° and 135° directions were tightly coupled and distinct from the other angles, demonstrating an increase in correlation around 3-4 mm before tapering down again. The other grids showed largely consistent behaviors across the four orientations.

Coherence: the role of frequency

Coherence, a measure of correlation as a function of frequency, demonstrated patterns in frequency and space (Fig. 3.11 and 3.12). Coherence functions were estimated by averaging the results of consecutive 4-second segments (250 4-sec segments for SC; 450 4-sec segments for all other grids). Three-dimensional meshes in Fig. 3.11 and 3.12 show coherence as a function of both frequency and separation distance simultaneously; the two columns of plots next to the meshes are projections onto the frequency and separation

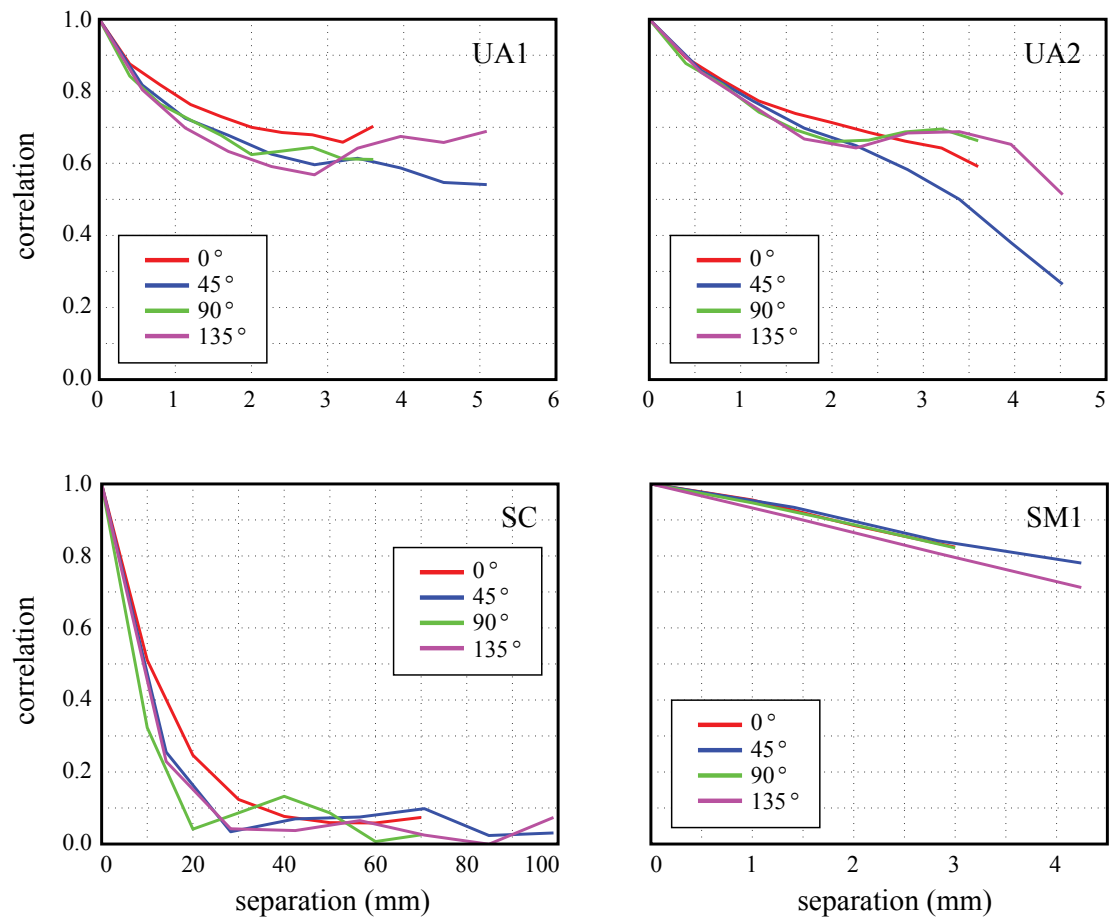
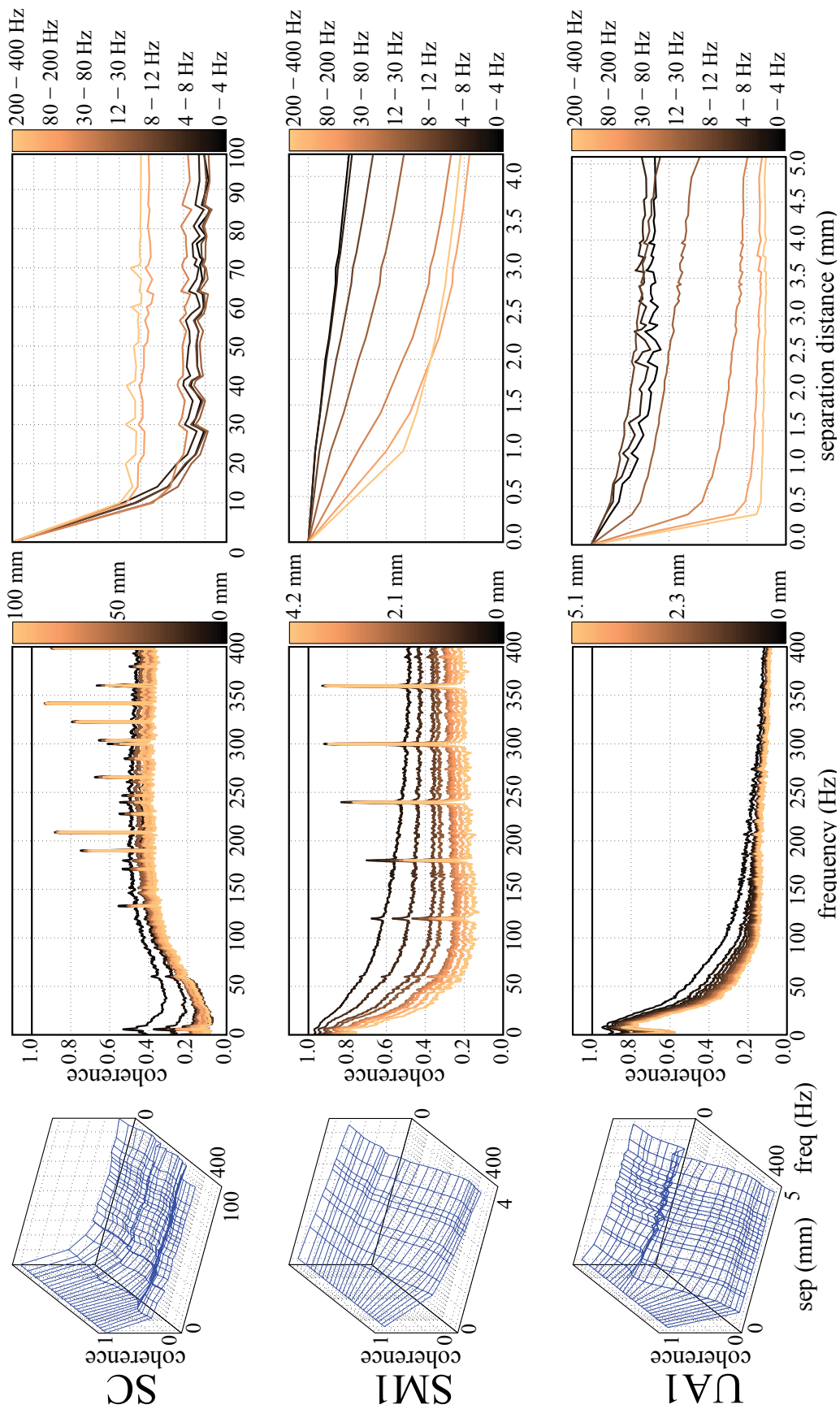


Fig. 3.10. Correlation vs. distance for channels along angled axes. Consider a line connecting each pair of channels in a grid. With the horizontal plane of each grid chosen as an arbitrary zero-degree axis, the angle of this line with respect to the zero-degree axis was found. Then, correlations between pairs of channels with like angles (where the angles considered included 0° , 45° , 90° , and 135°) were averaged to determine whether there was a directional dependence in the spatial distribution of correlations. Representative data are shown for UA1, UA2, SC, and SM1 only.

Fig. 3.11. Coherence functions estimated for each grid type. The leftmost panel in each row is a mesh showing the coherence plotted against both separation distance and frequency. The middle panel shows coherence plotted against frequency, with color representing separation distance. The right panel shows the coherence plotted against separation distance, with color representing frequency. The top row shows coherence from the SC grid; the middle row shows correlations from SM1; and the bottom row shows correlations from UA1.



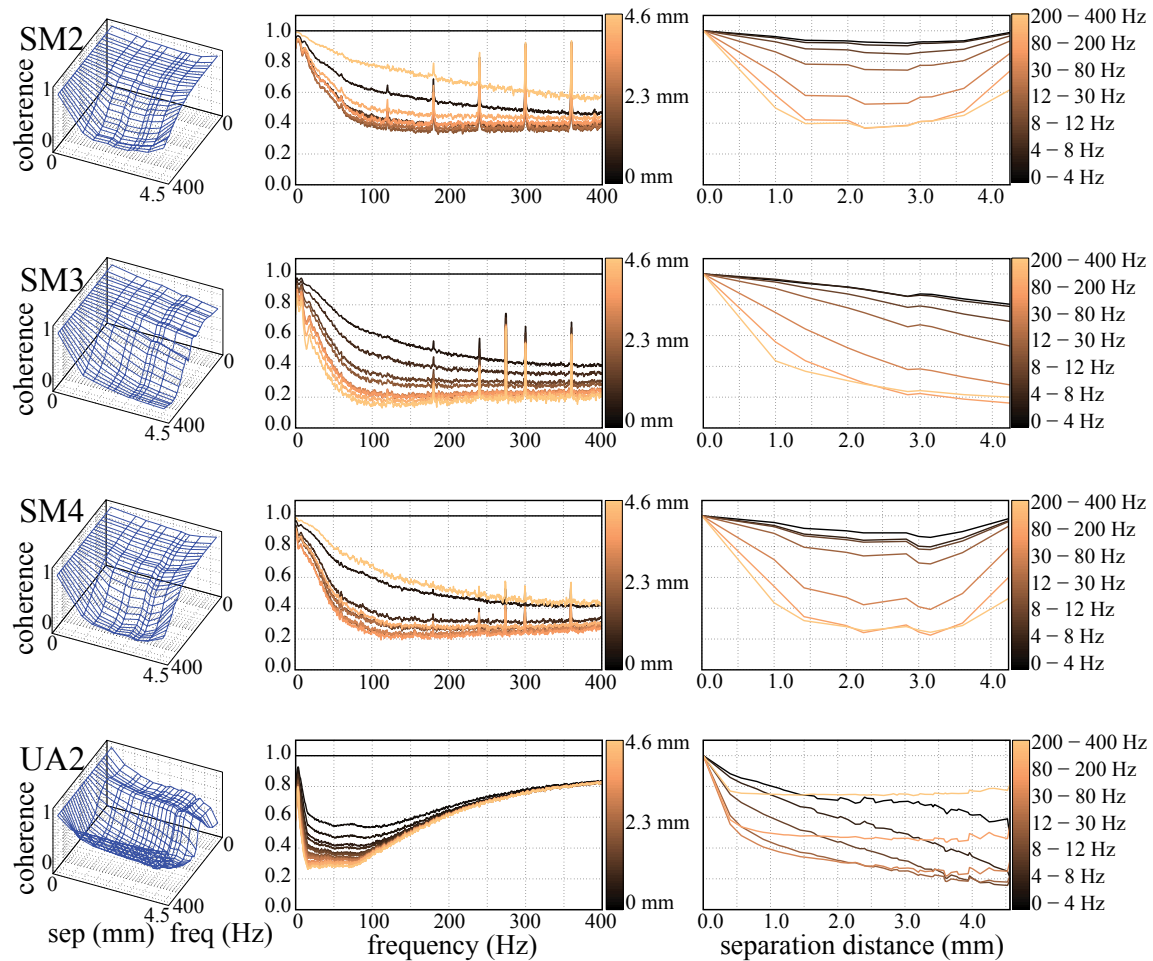


Fig. 3.12. Coherence over space and frequency for SM2, SM3, SM4, and UA2 grids. The leftmost panel in each row is a mesh showing the coherence plotted against both separation distance and frequency. The middle panel shows coherence plotted against frequency, with color representing separation distance. The right panel shows the coherence plotted against separation distance, with color representing frequency. Results are shown for SM2, SM3, SM4, and UA2 grids.

axes, with color representing the compressed axis (separation distance and frequency respectively for the middle and right columns). Only in the plots of coherence versus separation distance, coherence was averaged over frequencies to produce estimates of the coherence within the standard electroencephalographic frequency bands, e.g., delta (0-4 Hz), theta (4-8 Hz), alpha (8-12 Hz), beta (12-30 Hz), gamma (30-80 Hz), high gamma (80-200 Hz), and a very high band (200-400 Hz). Coherence was generally strongest for signals close in space and in lower frequencies; it was also observed that coherence was generally weakest in the high frequencies. The primary exception to this observation was the SC grid, which had the smallest maximum coherence (discounting auto-coherence and peaks due to line noise contamination) of any of the grids. The UA2 dataset also presents an exception to this general trend (Fig. 3.12), but will be discussed in more detail in a later section of this chapter.

For the UA and SM grids, coherence declined more rapidly with distance in higher frequencies than it did in lower frequencies. To characterize this behavior, the distance required for the coherence to decay to half its maximum range was calculated for each frequency (Fig. 3.13). This quantification, called half-height decay (HHD), is a measure of the spatial extent of the signals. Large HHD suggests that the signal remains highly correlated between widely separated electrodes; small HHD indicates that correlation declines quickly with separation. The SC grid had the largest HHD across all frequencies, with a peak of 8.9 mm at 6.35 Hz and a baseline value of 5.1 mm average between 300-400 Hz. The SM grids exhibited variable peak HHD with values ranging from 2.35 mm to 3.15 mm; however, HHD was tightly grouped in the high frequencies across the SM grids, with average values in the range 0.53-0.70 mm between 300-400 Hz. Baseline HHD was smallest for the UA grids, at 0.16 and 0.11 mm for UA1 and UA2, respectively. However, their peak HHD was as large as those seen in the SM grids with maximum values of 1.8 mm at 11.2 Hz (UA1) and 2.5 mm at 5.6 Hz (UA2). These results illustrate that cortical surface potentials contain millimeter and submillimeter scale dynamics.

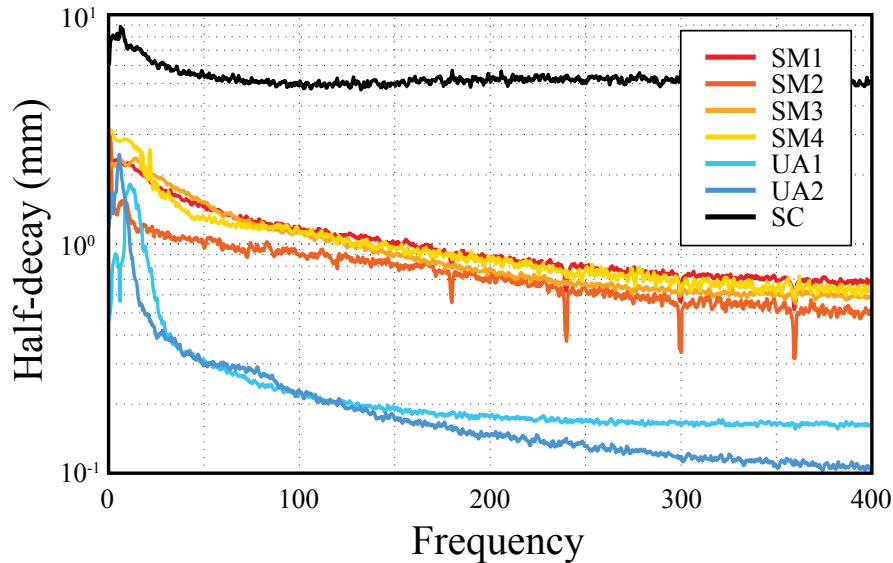


Fig. 3.13. Half-height decay (HHD) of the coherence (in millimeters). These results are shown as a function of frequency, for each grid in the study. For each frequency, the coherence from all channel pairs at a given separation distance were averaged to find coherence as a function of distance. A spline was fit to this curve, and the distance in millimeters found at which the coherence had dropped to half its maximum value (the HHD).

Coherence as a function of separation distance is illustrated in more spatial detail in Fig. 3.14, in which the coherence of each electrode with all other electrodes of the same grid is shown for two frequency bands: alpha (8-12 Hz) and gamma (30-80 Hz). Comparing these results to the correlation versus distance shown in Fig. 3.8 suggests that the low frequency components of the signal dominate correlations in broadband data, particularly for the smaller UA and SM grids. In the SC grid, however, the higher frequencies demonstrated higher correlations at larger separations than the lower frequencies.

The effects of software re-referencing

Re-referencing each channel to the grid average (i.e., common average re-reference, or CAR) substantially decreased correlations between pairs of channels in the smaller SM and UA grids, but not as much for the SC grid (Fig. 3.15; compare to Fig. 3.7). The initial slope of correlation versus distance for SM and UA grids was steeper for CAR data than for raw data (Table 3.3); for the SM grids, it decreased enough that the relationship between

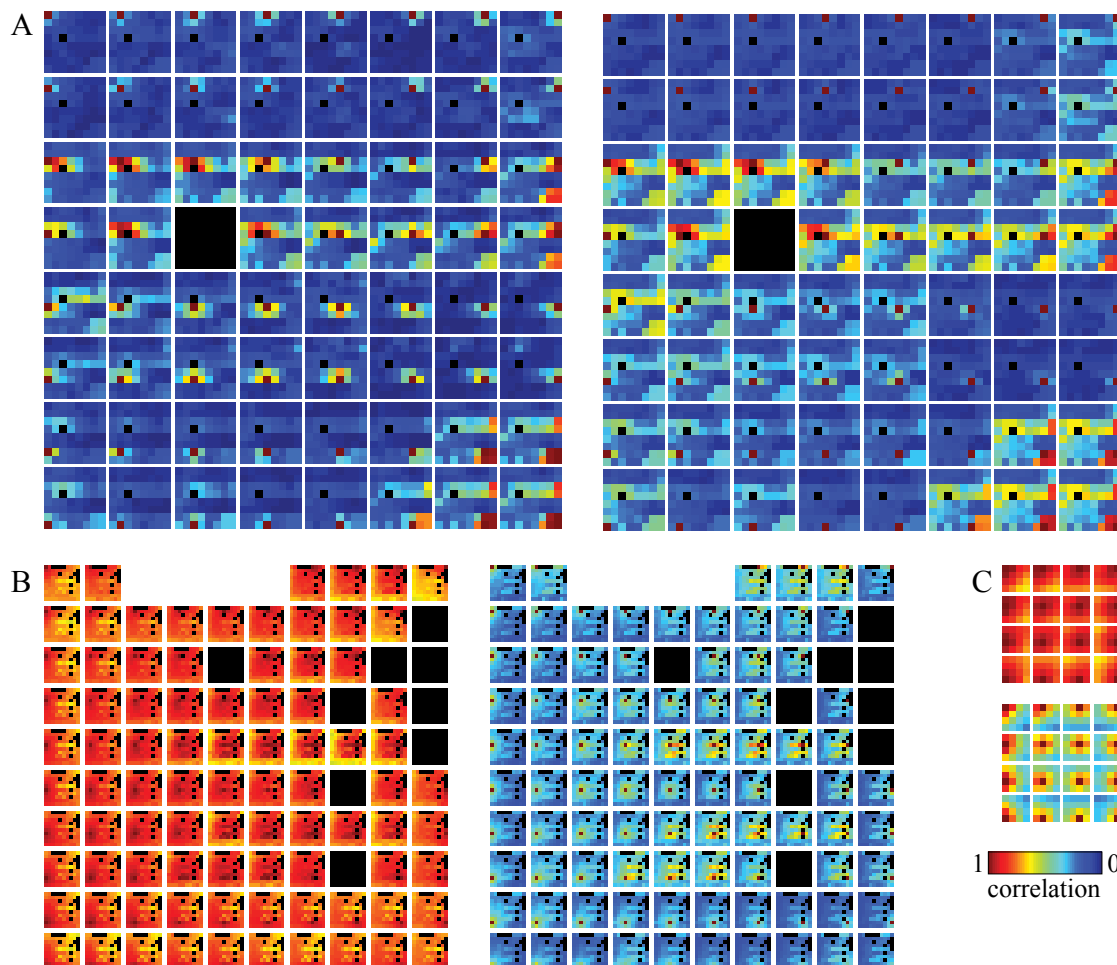


Fig. 3.14. Coherence between each channel and all other channels in the same grid. Shown are results for SC (Panel A), UA1 (Panel B), and SM1 (Panel C). The left portion (Panels A and B) or top portion (Panel C) shows coherence for the alpha band (8-12 Hz); the right portion (Panels A and B) or bottom portion (Panel C) of each panel shows coherence for the gamma band (30-80 Hz).

Table 3.3. Comparing the initial slope of correlation versus distance with and without common average re-referencing.

	SM1	SM2	SM3	SM4	UA1	UA2
ρ at 2 mm (raw)	0.89	0.90	0.87	0.87	0.64	0.67
ρ at 2 mm (CAR)	-0.03	-0.19	-0.00	-0.15	-0.09	-0.08

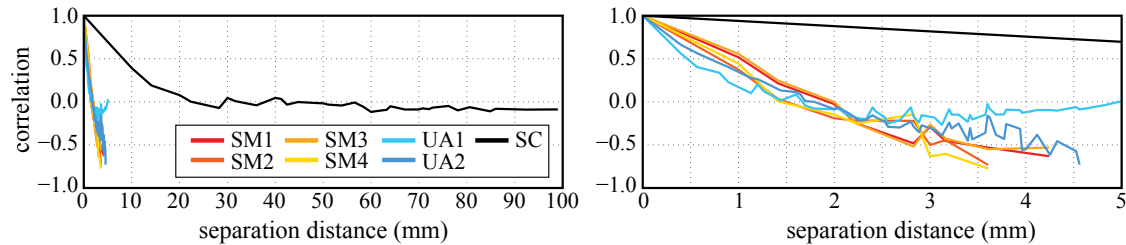


Fig. 3.15. Correlation vs. distance for data re-referenced to the common average. The left panel shows the correlation versus distance at the scale of the SC grid (i.e., 0-100 mm). The right panel shows the correlation versus distance at the scale of the SM and UA grids.

correlation and distance in microscale recordings of surface potentials was similar to that of the intracortical LFP. However, CAR preprocessing had little effect on the initial slope of correlation versus distance for the SC grid (average correlation at 10 mm was 0.42 for raw data versus 0.39 for CAR data). After CAR preprocessing, the baseline half-height decay between 300-400 Hz in the coherence was 0.31-0.39 mm for the SM grids, 0.16-0.17 mm for the UA grids, and 4.4 mm for the SC grid.

For the large SC grid, the correlation at large separations was still comparably small after CAR preprocessing: the average correlation over the last 30 mm of separation was -0.08 for CAR data and 0.04 for raw data. However, for all of the smaller grids except UA1, the CAR data extended almost linearly from strong positive correlations at small separations to strong negative correlation (e.g., less than -0.5) at the largest separations within the array (Fig. 3.15). The common average was not dominated by any one channel (correlations of each channel's raw data with the common average were 0.95 ± 0.02 across the four SM grids and 0.83 ± 0.10 across the two UA grids).

As pointed out previously in this chapter, UA2 demonstrated behavior, particularly in higher frequencies of the coherence, which was unexpected both as a general characteristic of neural data and also when compared to the behavior of UA1. To investigate the cause of this phenomenon, the spectrum of the common average was compared between the two UA grids, and the spectrum of UA2's common average was found to contain significantly

more power in the higher frequencies than UA1 (data not shown). It is likely that noise contaminated the UA2 data perhaps through an unquiet ground or reference; after re-referencing the UA2 data to the common average, the high-frequency contamination largely disappeared, and the coherence of the two UA grids were more similar (Fig. 3.16; Panel A shows coherence for raw and CAR data from UA1; Panel B shows the same results for UA2).

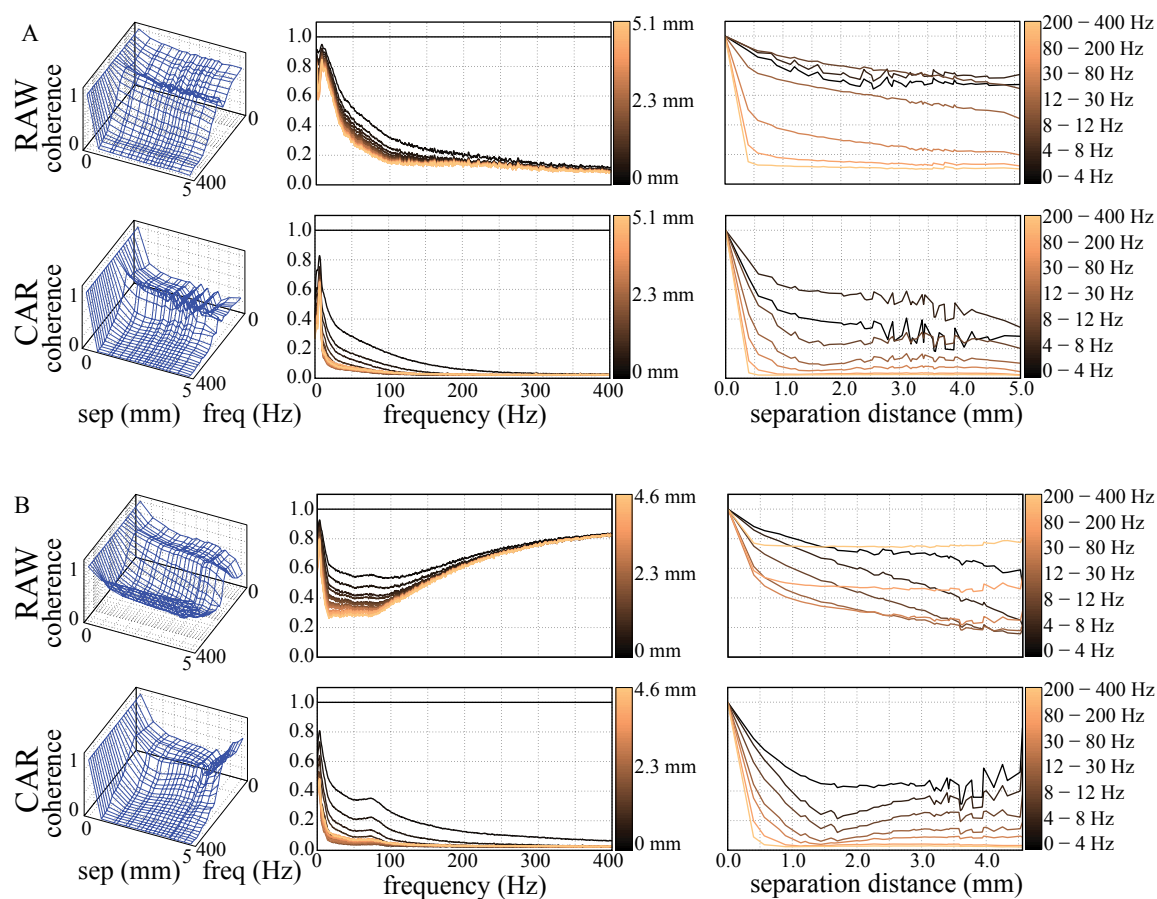


Fig. 3.16. Coherence for UA1 and UA2 compared for raw and CAR data. Panel A shows results for UA1; Panel B shows results for UA2. The top row in Panel A and Panel B is the coherence for raw data; the bottom row in each panel is the coherence for CAR data. The leftmost panel in each row is a mesh showing the coherence plotted against both separation distance and frequency. The middle panel shows coherence plotted against frequency, with color representing separation distance. The right panel shows the coherence plotted against separation distance, with color representing frequency.

Discussion

Linear measures, i.e., correlation and coherence, have been used to evaluate temporal, spatial, and frequency-domain dynamics in neural signals recorded intracortically by microelectrodes and epicortically by both micro- and macroelectrodes. Correlation and coherence were strongest across all modalities for signals closest in space and time, and in the lower frequencies. Furthermore, these linear relationships, on average, tended to decay gradually over space, time, and frequency, but significant dynamics remain even at large separations. The baseline half-height decay of the signals was 110-160 μm for the UA grids, 530-700 μm for the SM grids, and 5.1 mm for the SC grid. The half-height measurements of the autocorrelation function (i.e., the FDHMs) were found to be in the range 66-129 msec for the UA grids, 97-191 msec for the SM grids, and 148 msec for the SC grid. Re-referencing the data to the common average affected the smaller grids differently from the large clinical ECoG grid, in that removing the “global” element from the small grids tended to pull correlations at large separations to strong negative values, whereas in the clinical grid the correlations stayed negligibly small at large separations. Intracortical LFP is the most specific method, in both space and time, of recording cortical field potentials, but surface potentials recorded at the appropriate scale, i.e., by microelectrodes, contain fine dynamics in both space and time which are comparable in extent to, if not always as fine as, the intracortical LFP.

Factors influencing spatiotemporal dynamics

The resolution with which neural activity may be recorded at any depth is practically limited by a number of factors. The distance between the electrode and the neural source(s) and the transmittance properties of the materials in the intervening space determine the severity of the attenuation and filtering of the neural activity before it can be recorded. The size of the electrode and its impedance properties relative to both the surrounding tissue and the amplifier input influence how much of the surrounding tissue

will contribute to the electric potential. Small, transient dynamics, which would be masked in the integration of larger volumes of cortex, might be observable when recorded by tightly spaced microelectrodes. Intuitively, it is reasonable to expect that field potentials recorded by microelectrodes within the cortex should afford the greatest resolution since they are nearest the signal generators. These results support such a possibility, in that the UA grids demonstrated, on average, the smallest half-height decay in both time and space. Such concepts also suggest that μ ECoG may consist of a fundamentally different signal than traditional ECoG, an idea further supported by the different spatiotemporal properties found for the SM vs. the SC grids.

Processing mechanisms of the cortex, including differences across cortical layers, have been shown to influence the spatial extent of LFP. For example, it has been observed in cat suprasylvian cortex that coherence falls off more rapidly with distance during wake or REM sleep states than during slow wave sleep [25]. Sleep or drowsiness most typically lowered coherence across frequencies in human cortex [32], and alpha rhythms demonstrated significantly different coherence when resting with eyes open vs. squeezing a sponge with eyes closed [40]. Spatially extensive coherence has been observed in macaque V1 with large-grating visual stimuli whereas smaller stimuli were found to induce more local activity [15], and long-distance correlations (e.g., between pre- and postcentral LFPs) have been shown to be more likely during exploratory tasks than during trained motor movements [26]. The cortical spread of LFP was found to vary significantly across cortical layers in macaque V1, from 150 μ m in layer 4B to 280 μ m in layer 2/3 [21]. For comparison, correlations in spontaneous neuronal spiking activity in cat visual cortex have been shown to fall to 50% within 240 μ m [53]. To avoid as many of these confounding variables as possible, data were selected from hours when the patients were most likely to be awake and behaving naturally. Additionally, estimates of the linear relationships in the data were formed by averaging over significant amounts of time in order to reveal the underlying patterns of spatiotemporal dynamics in the neural data.

Anatomical location may have played some role in the spatiotemporal dynamics of the field potentials. SM4 over Wernicke's area had a larger average FDHM and wider distribution of FDHM than the other SM grids, and the SC grid had the largest distribution of FDHMs of all the grids. While there is no straightforward explanation for why the nature of signals over Wernicke's area might be different from those over motor cortex, in the case of the SC grid the large variance is perhaps due to disparate functional areas covered by the large grid. Indeed, some electrodes in SC demonstrated large FDHMs and large distributions while others demonstrated smaller FDHMs with tighter distributions, suggesting variation on a scale more in line with crossing functional cortical boundaries.

Characteristics of spatiotemporal dynamics

In figures demonstrating correlation versus distance, the SC and UA grids were characterized by an inflection point where the slope of the curve flattened out while the SM grids exhibited no such knee. The presence of an inflection point suggests that there is a baseline correlation in the field potentials, and that the correlation will not change with increasing separation distance. In the case of the SC grid, the inflection occurred between 20 and 30 mm, and the baseline correlation was close to 0. For the UA grids, the correlation flattened out at much higher levels. It is possible that the high baseline correlation in the UA grids and the lack of an inflection point in the SM grids is due to the small size of the grids, or particularly in the case of the SM grids, it could also be due to the few unique separations between channels. The fact that correlation between SM channels separated by several centimeters dropped to approximately 0.3 suggests that it is more likely the former issue for the SM grid. However, it could also be the case that intracortical LFP is more dynamic on finer scales than surface potentials regardless of the size of the recording electrode.

In some cases, high correlations were present between electrodes which were separated by large distances. Spatially distinct correlations could arise when one region of

cortex is functionally bound to a discretely separate region of cortex during task or stimulus [27, 35]. Such synchronous oscillations in the field potentials of the two regions would be registered as an increase in the level of correlation between them. In further evidence that the underlying brain activity was spatially variable, the distributions of correlation versus distance over space and time (Fig. 3.7) was dynamic over time, but changes in spatial correlation patterns demonstrated even larger distributions [35].

The majority of grids showed no directional anisotropy, which could be due to the arbitrary relationship between the orientation of the array with respect to the cortex, and the angles selected for analysis, or perhaps that too much or too little cortex was included to elicit directional patterns. In the SC grid, one might expect to see directional patterns at a smaller spatial scale, or between just one or two pairs of electrodes. It is also likely that anisotropies in the cortical information processing do not necessarily occur in consistent directional modalities, but rather in highly nonlinear spatial patterns, particularly as effects from anatomical considerations such as vasculature and gyrii and sulci, as well as mesoscopic and macroscopic functional organization come into play.

Clear changes were evident in the strength of linear relationships between channels across frequency. Previous work has found similar dependence on frequency: tuning for speed and direction in extrastriate cortex (MT) was found to exhibit superior specificity for high frequencies, i.e., gamma and above [20]. In general, high frequencies have been shown to exhibit more local extent whereas low frequencies are more spread out [12, 20, 22, 24, 25]. It has been suggested that this dependence on frequency could be an artifact of low pass filtering by capacitive properties of cortical tissue [54]; however, with direct experimental evidence for isotropically flat frequency response in gray matter, the impedance of cortical tissue is unlikely to be a significant factor in any frequency-dependent trends in the decay of neural activity [8]. A different plausible explanation for the dependence of correlation on frequency is that small, local populations with fast transient activities generate high frequency oscillations whereas low frequency content represents spatially

broad modulation of local population activity as these distributed processing elements are coordinated to produce coherent, cognitive outputs [9, 12, 24].

The SC grid had the smallest maximum coherence, discounting self-coherence or noisy peaks, of any of the grids. It is possible that the dynamics seen in the other grids were largely missed in the 10 mm separating the closest SC electrodes; the smaller grids had much larger coherence at the closest spacing although the high frequencies exhibited small coherence across all separations.

Referencing

Substantial changes were observed in the nature of the spatiotemporal dynamics on the smaller UA and SM grids, but not as much in the SC grid, after re-referencing the data in software to the common average. Correlation between the common average and each channel of raw data was calculated to see whether one channel might have contaminated the average, but there were no obvious outliers. It is likely that the wide range of correlations in the CAR data reflects the presence of local activity in the small arrays. That the CAR had little effect on the large SC grid is probably due to the amount of cortex contributing to the common average. In the small grids, the common average itself is approximately the signal that would be recorded by a single large ECoG electrode in the SC grid. What is global to the SM and UA grids is local to the SC grid, and locally-derived activity is probably a more dominant factor in the common average of these smaller grids than in the SC grid. These issues are further complicated by the variety of referencing strategies employed. Electric potentials are by definition a relative measurement; if the reference is very close to the recording electrode, only very local neural sources will induce changes in the potential between the two. If the reference is far from the recording electrode, both global and local components may contribute to the recorded electric potential [55].

Limitations

The data collected for this study were acquired in patients undergoing surgical intervention for medically refractory epilepsy. At least one study has illustrated that pathology in cortical tissue affects the coherence [36]; thus, the results presented here must be taken in that context. In particular, the UA grids were implanted in portions of the temporal lobe likely to be resected, and so are most likely to be widely contaminated pathological cortical network interactions. Portions of the SC are likely to be over epileptogenic zone, while the SM grids were generally placed away from epileptogenic zones and over functional areas which could be exercised with motor and speech tasks. Although the possibility of contamination of the data by epileptiform discharges is real, care was taken to select data which was not recorded during seizure and demonstrated little pathological behavior.

Conclusion

The brain is comprised of many millions of distinct sources which operate at the scale of microns and milliseconds. Selecting an electrode to record activity generated by this complex network requires balancing a number of factors including patient risk, cortical coverage, and spatiotemporal specificity required by the application. This work has demonstrated that surface potentials recorded by microelectrodes demonstrate fine spatiotemporal resolution—much greater than when the same potentials are recorded by macro ECoG electrodes. Thus, microelectrocorticography presents an attractive option for applications like brain-computer interfaces which rely on locally differential features within and between functional areas to actuate external devices by interpreted thought.

References

- [1] T. H. Bullock, "Signals and signs in the nervous system: the dynamic anatomy of electrical activity is probably information-rich," *Proc. Nat. Acad. Sci.*, vol. 94, pp. 1-6, Jan. 1997.
- [2] A. K. Engel, P. Konig, C. M. Gray, and W. Singer, "Stimulus-dependent neuronal oscillations in cat visual cortex: inter-columnar interaction as determined by cross-correlation analysis," *Eur. J. Neurosci.*, vol. 2, pp. 588-606, 1990.
- [3] U. Mitzdorf, "Current source-density method and application in cat cerebral cortex: investigation of evoked potentials and EEG phenomena," *Physiol. Rev.*, vol. 65, pp. 37-100, Jan. 1985.
- [4] U. Mitzdorf, "Properties of the evoked potential generators: current source-density analysis of visually evoked potentials in the cat cortex," *Int. J. Neurosci.*, vol. 33, pp. 33-59, Mar. 1987.
- [5] W. J. Freeman and J. M. Barrie, "Analysis of spatial patterns of phase in neocortical gamma EEGs in rabbit," *J. Neurophysiol.*, vol. 84, pp. 1266-1278, Sep. 2000.
- [6] C. Mehring, M. P. Nawrot, S. C. de Oliveira, E. Vaadia, A. Schulze-Bonhage, A. Aertsen, and T. Ball, "Comparing information about arm movement direction in single channels of local and epicortical field potentials from monkey and human motor cortex," *J. Physiol.-Paris*, vol. 98, pp. 498-506, 2004.
- [7] S. Ray, N. E. Crone, E. Niebur, P. J. Franaszczuk, and S. S. Hsiao, "Neural correlates of high-gamma oscillations (60–200 Hz) in Macaque local field potentials and their potential implications in electrocorticography," *J. Neurosci.*, vol. 28, pp. 11526-11536, Nov. 2008.
- [8] N. K. Logothetis, C. Kayser, and A. Oeltermann, "In vivo measurement of cortical impedance spectrum in monkeys: implications for signal propagation," *Neuron*, vol. 55, pp. 809-823, 2007.
- [9] P. Fries, "Neuronal gamma-band synchronization as a fundamental process in cortical computation," *Annu. Rev. Neurosci.*, vol. 32, pp. 209-224, 2009.
- [10] W. Singer and C. M. Gray, "Visual feature integration and the temporal correlation hypothesis," *Annu. Rev. Neurosci.*, vol. 18, pp. 555-586, 1995.
- [11] C. von der Malsburg, "Binding in models of perception and brain function," *Curr. Opin. Neurobiol.*, vol. 5, pp. 520-526, 1995.
- [12] G. Buzsaki and A. Draguhn, "Neuronal oscillations in cortical networks," *Science*, vol. 304, pp. 1926-1929, Jun. 2004.
- [13] V. B. Mountcastle, "Modality and topographic properties of single neurons of cat's somatic sensory cortex," *J. Neurophysiol.*, vol. 20, pp. 408-434, Jul. 1957.

- [14] I. Ayzenshtat, E. Meirovithz, H. Edelman, U. Werner-Reiss, E. Bienenstock, M. Abeles, and H. Slovin, "Precise spatiotemporal patterns among visual cortical areas and their relation to visual stimulus processing," *J. Neurosci.*, vol. 30, pp. 11232-11245, Aug. 2010.
- [15] X. Jia, M. A. Smith, and A. Kohn, "Stimulus selectivity and spatial coherence of gamma components of the local field potential," *J. Neurosci.*, vol. 31, pp. 9390-9403, Jun. 2011.
- [16] B. Amirikian and A. P. Georgopoulos, "Modular organization of directionally tuned cells in the motor cortex: is there a short-range order?," *Proc. Nat. Acad. Sci.*, vol. 100, pp. 12474-12479, Oct. 2003.
- [17] A. Georgopoulos, M. Taira, and A. Lukashin, "Cognitive neurophysiology of the motor cortex," *Science*, vol. 260, pp. 47-52, Apr. 1993.
- [18] A. Flinker, E. F. Chang, N. M. Barbaro, M. S. Berger, and R. T. Knight, "Sub-centimeter language organization in the human temporal lobe," *Brain Lang.*, vol. 117, pp. 103-109, Jun. 2011.
- [19] S. Katzner, I. Nauhaus, A. Benucci, V. Bonin, D. L. Ringach, and M. Carandini, "Local origin of field potentials in visual cortex," *Neuron*, vol. 61, pp. 35-41, 2009.
- [20] J. Liu and W. T. Newsome, "Local field potential in cortical area MT: stimulus tuning and behavioral correlations," *J. Neurosci.*, vol. 26, pp. 7779-7790, Jul. 2006.
- [21] D. Xing, C. I. Yeh, and R. M. Shapley, "Spatial spread of the local field potential and its laminar variation in visual cortex," *J. Neurosci.*, vol. 29, pp. 11540-11549, Sep. 2009.
- [22] P. Berens, G. A. Keliris, A. S. Ecker, N. K. Logothetis, and A. S. Tolias, "Comparing the feature selectivity of the gamma-band of the local field potential and the underlying spiking activity in primate visual cortex," *Frontiers Syst. Neurosci.*, vol. 2, Dec. 2008.
- [23] G. Kreiman, C. P. Hung, A. Kraskov, R. Q. Quiroga, T. Poggio, and J. J. DiCarlo, "Object selectivity of local field potentials and spikes in the macaque inferior temporal cortex," *Neuron*, vol. 49, pp. 433-445, 2006.
- [24] R. T. Canolty and R. T. Knight, "The functional role of cross-frequency coupling," *Trends Cogn. Sci.*, vol. 14, pp. 506-515, 2010.
- [25] A. Destexhe, D. Contreras, and M. Steriade, "Spatiotemporal analysis of local field potentials and unit discharges in cat cerebral cortex during natural wake and sleep states," *J. Neurosci.*, vol. 19, pp. 4595-4608, 1999.
- [26] E. E. Fetz, D. Chen, V. N. Murthy, and M. Matsumura, "Synaptic interactions mediating synchrony and oscillations in primate sensorimotor cortex," *J. Physiol.-Paris*, vol. 94, pp. 323-331, 2000.

- [27] F. Aoki, E. E. Fetz, L. Shupe, E. Lettich, and G. A. Ojemann, "Increased gamma-range activity in human sensorimotor cortex during performance of visuomotor tasks," *Clin. Neurophysiol.*, vol. 110, pp. 524-537, 1999.
- [28] M. W. Slutzky, L. R. Jordan, T. Krieg, M. Chen, D. J. Mogul, and L. E. Miller, "Optimal spacing of surface electrode arrays for brain-machine interface applications," *J. Neural Eng.*, vol. 7, p. 26004, Apr. 2010.
- [29] M. W. Slutzky, L. R. Jordan, and L. E. Miller, "Optimal spatial resolution of epidural and subdural electrode arrays for brain-machine interface applications," in *Proc. IEEE Engineering in Medicine and Biology Conf.*, 2008, pp. 3771-3774.
- [30] T. H. Bullock and M. C. McClune, "Lateral coherence of the electrocorticogram: a new measure of brain synchrony," *Electroencephalogr. Clin. Neurophysiol.*, vol. 73, pp. 479-498, 1989.
- [31] T. H. Bullock, M. C. McClune, J. Z. Achimowicz, V. J. Iragui-Madoz, R. B. Duckrow, and S. S. Spencer, "Temporal fluctuations in coherence of brain waves," *Proc. Nat. Acad. Sci.*, vol. 92, pp. 11568-11572, Dec. 1995.
- [32] T. H. Bullock, M. C. McClune, J. Z. Achimowicz, V. J. Iragui-Madoz, R. B. Duckrow, and S. S. Spencer, "EEG coherence has structure in the millimeter domain: subdural and hippocampal recordings from epileptic patients," *Electroencephalogr. Clin. Neurophysiol.*, vol. 95, pp. 161-177, 1995.
- [33] V. Menon, W. J. Freeman, B. A. Cutillo, J. E. Desmond, M. F. Ward, S. L. Bressler, K. D. Laxer, N. Barbaro, and A. S. Gevins, "Spatio-temporal correlations in human gamma band electrocorticograms," *Electroencephalogr. Clin. Neurophysiol.*, vol. 98, pp. 89-102, Feb 1996.
- [34] X. Pei, E. C. Leuthardt, C. M. Gaona, P. Brunner, J. R. Wolpaw, and G. Schalk, "Spatiotemporal dynamics of electrocorticographic high gamma activity during overt and covert word repetition," *Neuroimage*, vol. 54, pp. 2960-2972, Feb. 14 2011.
- [35] B. Shen, M. Nadkarni, and R. A. Zappulla, "Spectral modulation of cortical connections measured by EEG coherence in humans," *Clin. Neurophysiol.*, vol. 110, pp. 115-125, 1999.
- [36] V. L. Towle, I. Syed, C. Berger, R. Grzesczcuk, J. Milton, R. K. Erickson, P. Cogen, E. Berkson, and J.-P. Spire, "Identification of the sensory/motor area and pathologic regions using ECoG coherence," *Electroencephalogr. Clin. Neurophysiol.*, vol. 106, pp. 30-39, 1998.
- [37] C. M. Gaona, M. Sharma, Z. V. Freudenburg, J. D. Breshears, D. T. Bundy, J. Roland, D. L. Barbour, G. Schalk, and E. C. Leuthardt, "Nonuniform high-gamma (60–500 Hz) power changes dissociate cognitive task and anatomy in human cortex," *J. Neurosci.*, vol. 31, pp. 2091-2100, Feb. 2011.

- [38] S. Kellis, K. Miller, K. Thomson, R. Brown, P. House, and B. Greger, "Decoding spoken words using local field potentials recorded from the cortical surface," *J. Neural Eng.*, vol. 7, p. 056007, 2010.
- [39] H. Panagiotides, W. J. Freeman, M. D. Holmes, and D. Pantazis, "Behavioral states may be associated with distinct spatial patterns in electrocorticogram," *Cogn. Neurodyn.*, vol. 5, pp. 55-66, Mar. 2011.
- [40] H. P. Zaveri, W. J. Williams, J. C. Sackellares, A. Beydoun, R. B. Duckrow, and S. S. Spencer, "Measuring the coherence of intracranial electroencephalograms," *Clin. Neurophysiol.*, vol. 110, pp. 1717-1725, 1999.
- [41] W. Penfield and H. Jasper, *Epilepsy and the functional anatomy of the human brain*. Oxford, England: Little, Brown & Co., 1954.
- [42] E. C. Leuthardt, C. Gaona, M. Sharma, N. Szrama, J. Roland, Z. Freudenberg, J. Solis, J. Breshears, and G. Schalk, "Using the electrocorticographic speech network to control a brain-computer interface in humans," *J. Neural Eng.*, vol. 8, p. 036004, Jun. 2011.
- [43] E. C. Leuthardt, G. Schalk, J. R. Wolpaw, J. G. Ojemann, and D. W. Moran, "A brain-computer interface using electrocorticographic signals in humans," *J. Neural Eng.*, vol. 1, pp. 63-71, Jun. 2004.
- [44] J. C. Sanchez, A. Gunduz, P. R. Carney, and J. C. Principe, "Extraction and localization of mesoscopic motor control signals for human ECoG neuroprosthetics," *J. Neurosci. Meth.*, vol. 167, pp. 63-81, Jan. 2008.
- [45] G. Schalk, J. Kubanek, K. J. Miller, N. R. Anderson, E. C. Leuthardt, J. G. Ojemann, D. Limbrick, D. Moran, L. A. Gerhardt, and J. R. Wolpaw, "Decoding two-dimensional movement trajectories using electrocorticographic signals in humans," *J. Neural Eng.*, vol. 4, pp. 264-275, Sep. 2007.
- [46] S. S. Kellis, P. A. House, K. E. Thomson, R. Brown, and B. Greger, "Human neocortical electrical activity recorded on nonpenetrating microwire arrays: applicability for neuroprostheses," *Neurosurg. Focus*, vol. 27, p. E9, Jul 2009.
- [47] E. C. Leuthardt, Z. Freudenberg, D. Bundy, and J. Roland, "Microscale recording from human motor cortex: implications for minimally invasive electrocorticographic brain-computer interfaces," *Neurosurg. Focus*, vol. 27, p. E10, Jul 2009.
- [48] E. M. Maynard, C. T. Nordhausen, and R. A. Normann, "The Utah Intracortical Electrode Array: a recording structure for potential brain-computer interfaces," *Electroencephalogr. Clin. Neurophysiol.*, vol. 102, pp. 228-239, 1997.
- [49] C. T. Nordhausen, E. M. Maynard, and R. A. Normann, "Single unit recording capabilities of a 100 microelectrode array," *Brain Res.*, vol. 726, pp. 129-140, 1996.

- [50] C. T. Nordhausen, P. J. Rousche, and R. A. Normann, "Optimizing recording capabilities of the Utah intracortical electrode array," *Brain Res.*, vol. 637, pp. 27-36, 1994.
- [51] M. Natrella, NIST/SEMATECH e-Handbook of Statistical Methods: NIST/SEMATECH, 2010.
- [52] P. Mitra and H. Bokil, *Observed brain dynamics*. Oxford University Press, 2008.
- [53] Y. H. Ch'Ng and C. Reid, "Cellular imaging of visual cortex reveals the spatial and functional organization of spontaneous activity," *Frontiers Integrative Neurosci.*, vol. 4, Aug. 2010.
- [54] C. Bédard, H. Kröger, and A. Destexhe, "Modeling Extracellular Field Potentials and the Frequency-Filtering Properties of Extracellular Space," *Biophys. J.*, vol. 86, pp. 1829-1842, 2004.
- [55] G. Fein, J. Raz, F. F. Brown, and E. L. Merrin, "Common reference coherence data are confounded by power and phase effects," *Electroencephalogr. Clin. Neurophysiol.*, vol. 69, pp. 581-584, Jun 1988.

CHAPTER 4

CHARACTERIZATION OF MICRO-ECOG ELECTRODES

Brain-computer interfaces (BCIs) must capture the information-bearing spatiotemporal dynamics of neural activity in order to maximize performance. Cortical surface potentials, which are attractive for BCIs because of their limited invasiveness, have traditionally been recorded with large, widely spaced electrodes which integrate the activity of large volumes of cortex. Nonpenetrating microwires are a novel solution for recording surface potentials at spatial resolutions more suited to high-performance BMI applications. Because smaller neuronal populations are integrated to form the potential at each electrode, these small grids may also capture more detailed temporal dynamics. Nonpenetrating microwires consist of platinum microwire, typically 40-80 μm in diameter, terminated in a grid with 1-2 mm pitch. Initial reports have shown that nonpenetrating microelectrodes are good candidates for BCI applications [1-3]. The microelectrode grids characterized in this study were manufactured commercially and are approved by the FDA for human use (PMT Corporation, Chanhassen, MN; Ad-Tech Medical, Racine, WI).

Methods

Electrochemical Impedance Spectroscopy

Three grids from two manufacturers were characterized using electrochemical impedance spectroscopy (EIS): a 16-channel grid with 70 μm wire and 1 mm spacing (PMT Corp.); a 32-channel grid with 55 μm wire and 2 mm spacing (PMT Corp.); and, a 32-channel grid with 45 μm wire and 2 mm spacing (Ad-Tech Medical) [4, 5]. These three

grids will be referred to as PMT16, PMT32, and ADT32, respectively (Fig. 4.1). In both PMT32 and ADT32, two of the 32 electrodes are large platinum discs to be used as ground and reference.

In separate experiments, each of the microwire grids was submersed in 0.1M phosphate-buffered saline (PBS) solution, with a saturated calomel electrode (SCE) as reference and platinum wire as counter electrode. EIS was performed using a Gamry Reference 600 Potentiostat to apply small-magnitude AC signals and measure the corresponding changes in phase and magnitude of the sensed signals.

An electrical model of a single platinum microwire electrode was formulated as a resistor in parallel with a series combination of a constant phase element (CPE) and Warburg diffusion element (W) (Fig. 4.2). The CPE element is defined by $Y_{0,CPE}$, the capacitance, and α_{CPE} , a nonideality factor (equal to 1 for an ideal capacitor). The CPE models the electric double-layer at the metal-solution interface. The Warburg diffusion element W models ion diffusion from solution to electrode, and is defined by an admittance parameter $Y_{0,W}$ and β_W , which accounts for finite thickness of the diffusion layer.

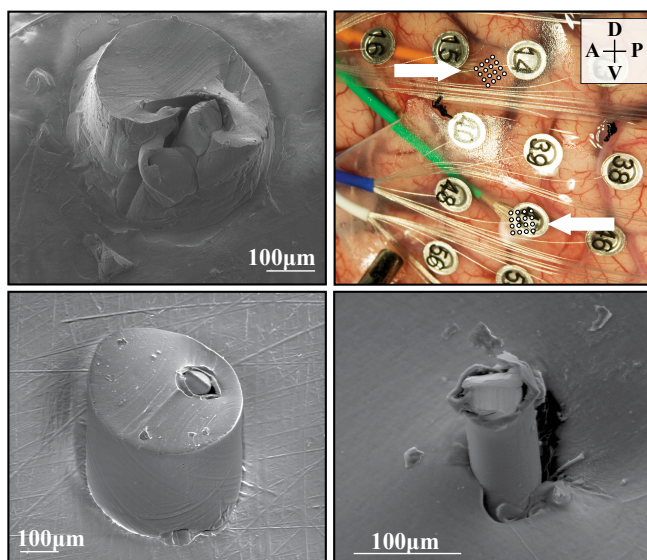


Fig. 4.1. Nonpenetrating microwire devices. (Top Left) A single electrode from PMT16. (Top Right) A surgical photo showing two PMT16-style grids (white arrows) implanted underneath a grid of macro ECoG electrodes (large silver-colored disks). (Bottom Left) A single electrode from PMT32. (Bottom Right) A single electrode from ADT32.

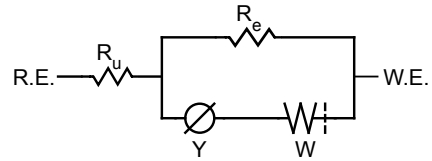


Fig. 4.2. Equivalent circuit used to fit the measured EIS results.

SPICE modeling

A resistor mesh (Fig. 4.3) was designed in SPICE to model frequency-independent signal propagation through the structure of the cerebral cortex [6]. The basic unit of the model represented an area of cortex approximately 0.5 mm^2 in diameter and 4 mm deep, with resistors modeling impedance in three dimensions: two orthogonal dimensions which span the plane of the cortical surface (e.g., x and y dimensions), and a surface-perpendicular dimension (i.e., z). A voltage source was placed between depth layers at 2 and 3 mm to excite the mesh network from within the modeled cortex. Fig. 4.3 shows a two-dimensional slice (x and z dimensions) of the model. Sufficient replicas of the basic three-dimensional unit were arranged to model a volume of cerebral cortex large enough to provide coverage for a full 16-channel microelectrode grid.

Within the cerebral cortex portion of the model, resistivity parallel to the cortical surface was set at $6 \text{ } \Omega/\text{m}$, and resistivity perpendicular to the cortical surface was set at $5 \text{ } \Omega/\text{m}$. The slight offset in these impedances was intended to model local neuronal assemblies working synchronously to process similar types of input stimuli. The resistivity perpendicular to the surface corresponds to the reported conductivity of gray matter, 0.2 S/m [7].

A second resistor mesh was added to the “surface” of the modeled cerebral cortex to represent cerebrospinal fluid (CSF). An electrical model of the microelectrodes, with parameters fitted from the measured EIS data, was connected to the CSF layer. A very high impedance represented the amplifier input. The resistivity of the CSF resistor mesh was swept between $0.2 \text{ } \Omega/\text{m}$ and $2 \text{ k}\Omega/\text{m}$. A resistivity of $0.56 \text{ } \Omega/\text{m}$ corresponds to the reported conductivity of CSF, approximately 1.8 S/m [8].

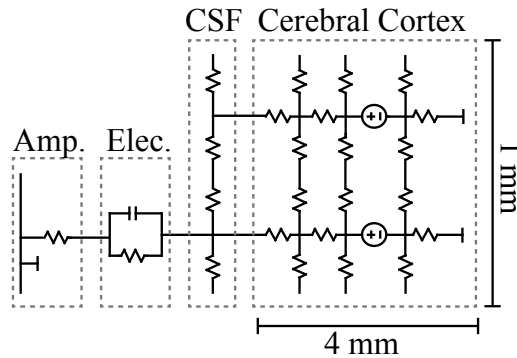


Fig. 4.3. Resistor mesh modeling electrode and cortical tissue. Components of the model represent amplifier input, electrode, CSF, and cortex, for 1 mm of cortical surface (in a single dimension) and 4 mm of depth.

The resistor mesh model was driven with uncorrelated pink noise generated within each modular unit. The pink noise was created by filtering white noise to mimic the $1/f$ power-law characteristic of cortical field potentials, then bandpass filtering to retain frequencies between 30 Hz and 200 Hz. These inputs were fed into the resistor network using piece-wise linear voltage sources. While simulating the full circuit in SPICE, voltages were probed at the amplifier input. Correlation coefficients were calculated for this simulated data in a similar fashion as was used for the measured data.

Results

Electrochemical Impedance Spectroscopy

The magnitude of the measured impedance of the platinum microwires in all three grids was log-linear from 1 Hz to 100 kHz (PMT16: 11.9 M Ω to 4.37 k Ω ; PMT32: 49.6 M Ω to 4.79 k Ω ; ADT32: 74.9 M Ω to 8.31 k Ω) (Fig. 4.4). The average impedance between 4-30 Hz (comprising theta, alpha, and beta bands) was 1.94 M Ω , 7.20 M Ω , and 11.2 M Ω ; and, between 80-200 Hz (comprising the high gamma bands) the average impedance was 231 k Ω , 744 k Ω , and 1.21 M Ω (PMT16, PMT32, and ADT32 respectively). At 1 KHz (a typical frequency for measuring the impedance of penetrating electrodes because of the higher frequency content of action potential waveforms), their average impedance magnitude was 49.2 k Ω , 135 k Ω , and 233 k Ω , respectively.

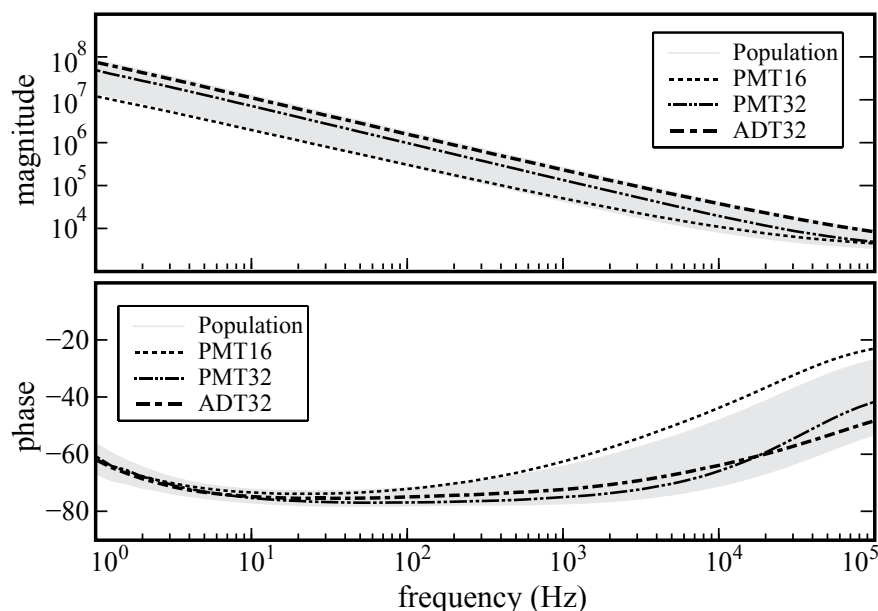


Fig. 4.4. Measured electrochemical impedance spectroscopy results. Magnitude of the measured impedance is shown in the top panel, and phase is shown in the bottom panel. The light gray areas represent the standard deviation of channels from all three grids.

The nonpenetrating microwires displayed relatively constant phase over the range of frequencies typically analyzed for surface potentials (Fig. 4.4). Between 1 Hz and 500 Hz, the mean and standard deviation of the phase angle (in degrees) was -71.4 ± 4.55 , -74.33 ± 4.92 , and -73.43 ± 3.85 (PMT16, PMT32, and ADT32, respectively).

Equivalent Circuit

The equivalent circuit used a resistor to model charge transfer resistance, a constant phase element (CPE) to model double-layer capacitance at the electrode-electrolyte interface, and a porous, bounded Warburg diffusion element to model diffusion across the interface (Fig. 4.2). With this configuration, 65 of the 76 microwires (86%) matched the equivalent circuit with an average goodness-of-fit of $2.5E-3$ (Table 4.1).

The value of the resistor modeling charge-transfer resistance increased with decreasing wire diameter, from $52.9 \text{ M}\Omega$ for the largest wire (PMT16; $70 \text{ }\mu\text{m}$) up to $322 \text{ M}\Omega$ for the smallest (ADT32; $45 \text{ }\mu\text{m}$). The exponent α in the CPE was more consistent across all three grids at 0.834, 0.872, and 0.848 (PMT16, PMT32, and ADT32), although

Table 4.1. Model parameters fit to measured EIS data.

	Mean	Std Dev	Units
Re	78.7	116	M Ω
$Y_{0,CPE}$	26.4E-09	17.5E-09	S*s $^{\alpha}$
α_{CPE}	832E-03	41.9E-03	--
$Y_{0,W}$	1.91E-06	4.19E-06	S*s $^{(1/2)}$
β_w	8.55E-03	17.3E-03	s $^{(1/2)}$
Goodness-of-fit	3.76E-03	3.99E-03	--

the parameter $Y_{0,CPE}$, indicating the magnitude of the capacitance, was largest for the grid with the largest wire diameter (24.2 nS*s $^{\alpha}$, 4.37 nS*s $^{\alpha}$, and 2.97 nS*s $^{\alpha}$ for PMT16, PMT32, and ADT32, respectively). The admittance $Y_{0,W}$ of the porous, bounded Warburg element was also consistent across all three grids, while the time constant parameter β_w was largest for ADT32 (1.61E-03 for ADT32 vs. 1.12E-03 and 1.01E-03 for PMT16 and PMT32 respectively).

Modeling the impact of CSF on channel correlation

The resistor mesh modeling tissue and electrodes was simulated in SPICE, and correlations in the voltage probed at the electrode-amplifier interface were calculated for several separation distances as a function of CSF conductivity (Fig. 4.5). With very low conductivity in the CSF layer, simulations predicted a baseline correlation at the cortical surface due to spread through the cerebral cortex resistor network, of $\rho = 0.70$ for 1 mm spacing, which is close to the measured values of 0.79 and 0.77 for FMC and Wernicke's area, respectively.

Introducing a layer of increasing conductivity (which could correspond, for example, to increasing thickness in the CSF layer) at the tissue-electrode interface strengthened linear relationships. At the reported conductivity of CSF, electrodes 3 mm apart were 92% correlated. Comparing in vivo measurements to these simulated results suggests a conductivity of between 0.05 S/m and 0.25 S/m at the cortical surface.

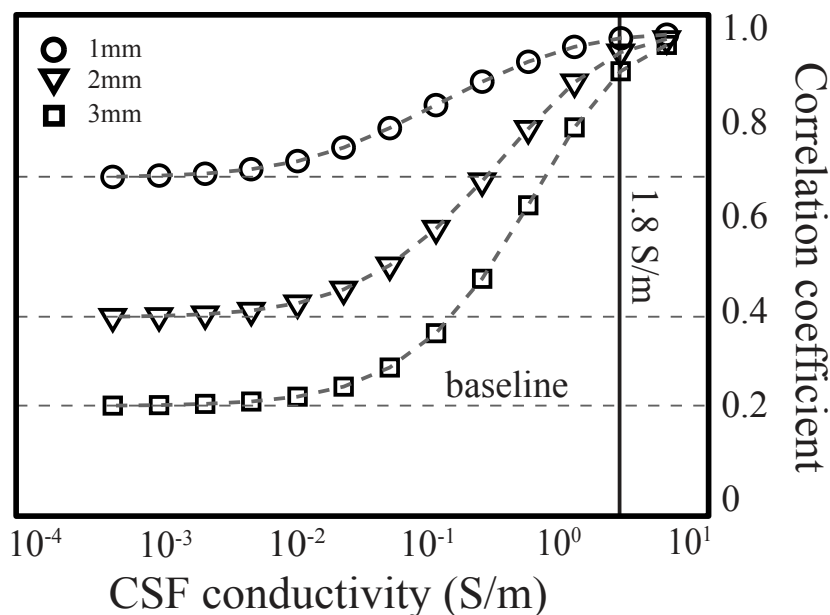


Fig. 4.5. Correlations calculated for simulated data. Correlation was measured from neighboring microwires as the conductivity of the CSF element in the SPICE model varied.

Discussion

Microelectrodes record surface local field potentials

Results from simulated models of the cerebral cortex have demonstrated the potential for millimeter-scale dynamics in neural activity recorded from the cortical surface. Data were simulated using platinum microwires (or an equivalent electrical model). Because of their recording characteristics and grid size and spacing, these electrodes appear to be well suited to capturing the information-bearing dynamics of the activity of the brain insofar as these dynamics are available at the cortical surface.

The signal recorded by nonpenetrating microelectrodes could be different from the signal recorded by clinical ECoG electrodes. Because the clinical electrodes are larger in diameter and have lower impedance, they are sensitive to activity from much larger regions of cortex. As the activity recorded by microwires is likely to be from a more local region of cortex, these signals could be termed surface local field potentials.

Comparison with macro-ECoG electrodes

Due to differences in the exposed surface area, the impedance properties of the platinum microwires were different from the impedance properties of clinical ECoG electrodes. EIS results from a few macro-ECoG electrodes demonstrated log-linear impedance magnitude which, for 1 Hz to 100 kHz, ranged between approximately 100 k Ω and 100 Ω – several orders of magnitude lower than the impedances measured for microwire electrodes.

Because the microwires have larger impedances than the clinical ECoG electrodes, a recording system which is used to record from clinical ECoG electrodes may not work well with micro ECoG sensors unless it has sufficiently high input impedance. For example, the Neuroport system used to record data for this study has an input impedance of approximately 10^{13} Ω , which is large enough that the difference between impedance of macro and micro ECoG electrodes is probably negligible.

Physically, the nonpenetrating microwire grids are much smaller than the macro ECoG grids, which means more electrodes fit per unit area at the cost of less total coverage of the cortex. The number of channels is most limited by the physical, transcutaneous cables which must connect subdural sensors to extracranial recording systems, and are an impediment to the patient's movements as well as a constant source of infection risk. In research applications, however, one is often interested in deriving as much information as possible from a specific functional area of the cortex, so high channel counts may outweigh the disadvantages of smaller total surface area.

It should also be noted that physically making such small grids is a challenge for standard manufacturing processes. Lithographic manufacturing processes, which are better suited to forming small features, could improve the quality of microelectrode contacts.

Impact of microwire diameter

The wire thickness was closely correlated with changes in the magnitude of the measured impedance (Fig. 4.4; magnitude of the impedance increased with decreasing wire diameter) and also with some model parameters (Table 4.1). In particular, the charge transfer resistance grew from 52.9 M Ω for the PMT16 grid to over 300 M Ω for the ADT32 grid with the smallest diameter wire, while the capacitance associated with the CPE fell from 24.2 to 2.97 nS*s^a. The lower charge transfer resistance may be an advantage to using larger gauge wire.

Reducing signal spread through CSF

CSF has a reported conductivity of 1.8 S/m—9 times more conductive than gray matter [7, 8]—and could allow significant signal spreading between closely spaced electrodes, depending upon the thickness of the CSF layer. Because propagation of electric potentials through conducting tissues and fluids would negatively impact the spatiotemporal resolution of the recorded signals, identifying and mitigating avoidable causes of signal spread is an important problem. The PMT16 and PMT32 grids were manufactured with silicone protrusions rising out of the base of the grid to surround and shield the platinum microwire up to the exposed tip (Fig. 4.1). In contrast, the ADT32 grid was manufactured to leave the platinum microwire to extend out of the grid base shielded only by the wire insulation. Whether intended or not, the silicone sheathing in the PMT grids may help the grid adhere to the cortical surface and also could shield the electrodes from biological matter such as CSF that flows in the subdural space. Despite imperfections in the commercial manufacturing process (Fig. 4.1), such a design feature may actually help to improve the performance of microelectrodes by reducing the amount of signal spread through CSF at the cortical surface.

Room for improvement in the SPICE model

The SPICE resistor mesh simulations do not perfectly represent the significant complexities of the human neocortex. For example, electrical sources were represented as discrete voltage sources within each organizational unit, missing both the complexities of ion flow driven by populations of neuron firings and synaptic activity, as well as inputs from other cortical areas. The resistor mesh, while modeling potential differences in lateral vs. vertical dimensions, was otherwise evenly and symmetrically organized, unlike the tortuous mesh of tissue in the cortex. Furthermore, some correlation in neural activity is likely to be inherent in the synchrony among functional areas necessary to produce coherent physical outputs.

The impedance of gray matter has been shown to be isotropic in surface-parallel planes and anisotropic across cortical layers [6]. Although the model used in this study did separate the cortex into layers of resistors, these were not intended to accurately capture the varying impedances of the different anatomically defined cortical layers. Rather, resistivity was generally consistent across the three dimensions, but surface-parallel resistivity was slightly higher than surface-perpendicular resistivity. This choice was made to approximate the synchronous activity of populations of neurons, perhaps loosely organized in surface-perpendicular oriented assemblies, working to process similar kinds of stimuli, e.g., cortical columns and related findings [9, 10].

Despite limitations, a resistor mesh may be a reasonable approximation of cortical tissue since previously measured impedances of cortical tissue have not been dependent on frequency [6]. The SPICE model estimates, to a first order, propagation in the cortex and potential signal spread through CSF at the cortical surface. Because the performance of an ECoG BCI is so tightly coupled to the accurate measurement of information-bearing dynamics, the indicated potential for blurring of features could be detrimental. Electrodes intended for ECoG BCIs should be designed to minimize signal spread through CSF in order to maximize information recorded from the neural activity at the cortical surface.

Conclusion

A brain signal sensor, consisting of platinum microwires terminated in a grid with millimeter-spaced intervals, has been characterized using EIS and modeling. The size and impedance characteristics of these microelectrodes indicate they will record a more local signal than that recorded by the large macro ECoG electrodes. In turn, this finding suggests that nonpenetrating microwires are well suited for BCI applications, where fast and accurate performance depends on the ability to capture as much information as is available to record. However, simulation of a conductive layer at the cortical surface has illustrated the potential consequences of conductive pathways through CSF between electrodes. These results motivate continued investigation of electrode design for neural prostheses using micro-ECoG, and illustrate the impact of accurately capturing millimeter-scale dynamics of cortical surface potentials on BCI performance.

References

- [1] S. S. Kellis, P. A. House, K. E. Thomson, R. Brown, and B. Greger, "Human neocortical electrical activity recorded on nonpenetrating microwire arrays: applicability for neuroprostheses," *Neurosurg. Focus*, vol. 27, p. E9, Jul 2009.
- [2] S. Kellis, K. Miller, K. Thomson, R. Brown, P. House, and B. Greger, "Decoding spoken words using local field potentials recorded from the cortical surface," *J. Neural Eng.*, vol. 7, p. 056007, Oct 2010.
- [3] E. C. Leuthardt, Z. Freudenberg, D. Bundy, and J. Roland, "Microscale recording from human motor cortex: implications for minimally invasive electrocorticographic brain-computer interfaces," *Neurosurg. Focus*, vol. 27, p. E10, Jul 2009.
- [4] S. Kellis, B. Greger, S. Hanrahan, P. House, and R. Brown, "Sensing millimeter-scale dynamics in cortical surface potentials for neural prosthetics," in *Proc. IEEE Sensors*, Limerick, Ireland, 2011, pp. 1823-1826.
- [5] S. Kellis, B. Greger, S. Hanrahan, P. House, and R. Brown, "Platinum microwire for subdural electrocorticography over human neocortex: millimeter-scale spatiotemporal dynamics," in *Proc. IEEE Engineering in Medicine and Biology Conf.*, Boston, MA, 2011, pp. 4761-4765.

- [6] N. K. Logothetis, C. Kayser, and A. Oeltermann, "In vivo measurement of cortical impedance spectrum in monkeys: implications for signal propagation," *Neuron*, vol. 55, pp. 809-823, Sep. 2007.
- [7] C.-I. Li, A. F. Bak, and L. O. Parker, "Specific resistivity of the cerebral cortex and white matter," *Exp. Neurol.*, vol. 20, pp. 544-557, 1968.
- [8] S. B. Baumann, D. R. Wozny, S. K. Kelly, and F. M. Meno, "The electrical conductivity of human cerebrospinal fluid at body temperature," *IEEE Trans. Biomed. Eng.*, vol. 44, pp. 220-223, 1997.
- [9] V. B. Mountcastle, "Modality and topographic properties of single neurons of cat's somatic sensory cortex," *J. Neurophysiol.*, vol. 20, pp. 408-34, Jul 1957.
- [10] V. B. Mountcastle, "Brain mechanisms for directed attention," *J. R. Soc. Med.*, vol. 71, pp. 14-28, Jan. 1978.

CHAPTER 5

DECODING MOTOR ACTIVITY USING LOCAL FIELD POTENTIALS RECORDED FROM THE CORTICAL SURFACE

Various approaches have been successfully used to correlate neuronal activity with specific movements. In some cases, this correlation has been sufficiently robust to drive the movement of an external device or cursor [1, 2]. Approaches based on standard electrocorticographic (ECoG) electrode arrays, used in most of the studies involving human subjects, have required the user of the device to focus on movement of different body parts. This requires patients to use nonintuitive movements to control an external device. It is possible such nonintuitive control signals have been required due to the limited spatial fidelity of the physical interface with the neocortex that is provided by ECoG electrodes.

Nonpenetrating microwire arrays could provide more spatial and temporal resolution than what is currently possible with electroencephalography (EEG) or using standard ECoG grids [3]. Because the electrodes are smaller, they have different physical properties, such as higher electrical impedances, than standard ECoG recording electrodes. These electrical properties require different amplification and signal analysis capabilities than those available with clinical EEG recording equipment, limiting investigations using nonpenetrating microwires to research protocols [5]. This work describes investigations using a nonpenetrating microwire platform to derive local neuronal signals and determine whether these signals contain sufficient information to decode a relatively stereotyped movement [6].

Methods

Subjects

Two male patients requiring extraoperative electrocorticographic monitoring for medically refractory epilepsy were enrolled in an Institutional Review Board-approved protocol. Informed consent was obtained from each patient.

Patient one (P1) was implanted with two 16-channel nonpenetrating microwire arrays (40-micron wire) (PMT Corporation, Chanhassen, MN) with 1-mm interelectrode spacing, placed in the epipial space underneath a standard clinical ECoG grid (Fig. 5.1). P1 suffered primarily from complex partial seizures subsequently shown to initiate in the posterior left temporal area. He harbored significant occipital encephalomalacia from a perinatal injury, but the peri-Rolandic area where the arrays were placed was essentially normal on MR imaging. One of the arrays was placed over upper extremity primary motor cortex as confirmed with intraoperative somatosensory evoked potential (SSEP) monitoring. The other array was placed more inferiorly along the precentral gyrus. Both arrays were referenced to a pair of epidural bare wires.

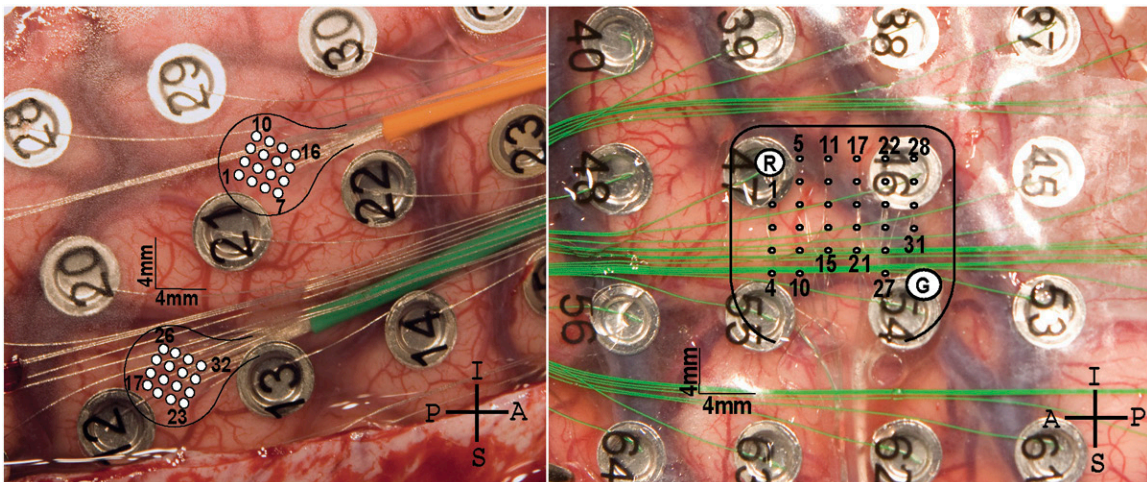


Fig. 5.1. Implant pictures from Patients 1 and 2. (Left) Two nonpenetrating microwire arrays (1-mm spacing) were implanted over right primary motor cortex in P1. Channels 1–16 are over hand area (orange wire), and channels 17–32 are over arm area (green wire). (Right) A single 30-channel array (2-mm spacing) was implanted over left primary motor cortex hand and arm area in P2.

Patient two (P2) was implanted with a single 30-channel nonpenetrating microwire array with 2-mm interelectrode spacing. P2 harbored a large right parietal gliotic cyst abutting the postcentral gyrus and suffered from focal motor as well as complex partial seizures. The anterior portion of the array was placed over the hand area of primary motor cortex as confirmed using extraoperative electrical stimulation with electromyographic confirmation. The array was referenced to two low-impedance electrodes built into the device. A standard ECoG grid with 1-cm electrode spacing was also placed on top of the array.

After electrode placement, the patients were observed in the Neurocritical Care Unit for continuous seizure monitoring. P1 was monitored for 2 weeks and performed 7 sets of movement tasks; P2 was monitored 5 days and performed 3 sets of movement tasks.

Experimental paradigm

Patients were instructed to perform simple, repetitive movements using a computer mouse. The mouse position was recorded continuously by use of a computerized pen tablet (Wacom Co., Ltd, Japan). Movement was accomplished using the hand and arm contralateral to the hemisphere in which the ECoG electrode array and nonpenetrating microwire array were located. On verbal cue, the patient moved the mouse from a starting position, at the bottom center of the tablet, to the upper left or the upper right corner, then returning to start position.

The order of targets was determined beforehand to be interleaved pseudorandomly and was communicated through the verbal cue. Trials lasted 2–3 seconds with a 1-second separation. Only trials at least 80% within one standard deviation of the average path, in both the horizontal and vertical components of movement, were retained for analysis. Approximately 20–30 recorded trials per patient per modality of movement remained after filtering. Plots of the recorded and analyzed movements and velocities for a portion of one patient recording are shown in Fig. 5.2.

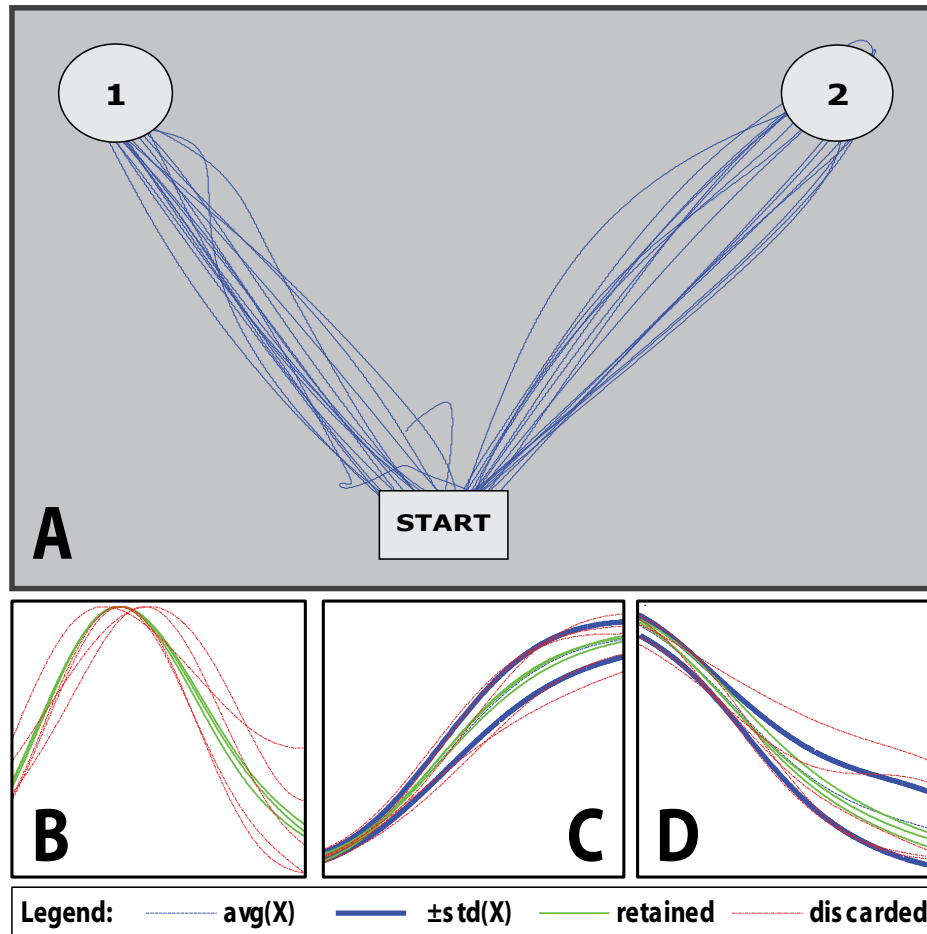


Fig. 5.2. Trial detection and filtering for a portion of recorded motor tasks including continuous movement, velocity profiles, and filtering of horizontal and vertical components. A: An overlay of computer mouse x- and y-position with the starting position and reach targets. Patients were instructed to move a computer mouse from the starting position (bottom center) to either the upper-left or upper-right corners of a computerized tablet, then return to the starting position. The target of each sequence was relayed verbally as a cue to begin movement. Movement sequences (outward reach and return) typically lasted 2–3 seconds with a brief pause at the target; however, only data recorded during outward reaching movement was used for analysis. Trials were marked by evaluating times at which velocity crossed a threshold. B: Overlaid velocity profiles of trials in the up-left direction. C: Filtering of the vertical component of movement for each trial in the up-left direction. D: Filtering of the horizontal component of movement for each trial in the up-left direction. In both the vertical and horizontal cases, the thick, dark lines indicate a single standard deviation away from the average path. To be retained for further analysis, a trial must be at least 80% within the boundaries in both the horizontal and vertical components of movement. Retained trials are shown in green; discarded trials are shown in dashed red. Overall, 55% of P1 trials and 56% of P2 trials were retained for analysis.

Data acquisition

The tablet and array outputs were recorded with a NeuroPort system (Blackrock Microsystems, Salt Lake City, UT). During digitization, the signals were bandpass filtered to preserve frequencies between 0.3 Hz and 7.5 KHz. Neural data were recorded at 30,000 samples/sec, and movement data were recorded at either 2,000 samples/sec or 30,000 samples/sec. All movement and electrode data were recorded by the same sampling and filtering process simultaneously, ensuring that movement position was well synchronized to ECoG data.

Preprocessing and analysis for directionality

Raw neural data were first downsampled from 30,000 samples/sec to 3,000 samples/sec. To mitigate the effects of 60-Hz noise, the trial-averaged spectrum for each nonpenetrating microwire was calculated to determine the width and amplitude of the 60-Hz noise band. Across all nonpenetrating microwires in P2, for example, noise levels in this band ranged from 5 dB through 20 dB above the normal spectrum, meaning that a single filter might effectively attenuate noise in a few channels but would leave large banding in most of the data. Therefore, a fifth-order Chebyshev Type-II filter was designed to individually mirror the calculated width and height of the 60-Hz noise. Next, the data were filtered to remove frequencies below 5 Hz and above 150 Hz using fifth-order Butterworth filters. Filtering was performed in MATLAB (MathWorks, Natick, MA), running once in the forward direction and once in the reverse direction, with appropriate initial conditions in the second pass, to ensure zero phase distortion.

Trial components were marked by points where the velocity of the patient's motion crossed a threshold of one standard deviation from rest. This model was used to mark both outward and return movement; additionally, baseline trials were marked at periods of no movement between trials. Only outward movement trials were included in the present analysis. The timestamps of these outward movements were used as markers for reading

electrode data. For spectrograms, one second of data, with movement aligned at 0.5 seconds, was used.

Spectrograms were generated using the Chronux (chronux.org) package with 250 msec windows and 50 msec step size; tapering parameters were set to a time-bandwidth product of five, and nine leading tapers. Spectrum plots of the raw data were characterized by a power law trend whose features dominated frequency analysis. For this reason, the spectrograms were normalized to the trial-averaged spectrum for all trials of like movement.

Differential power analysis was performed by normalizing the average gamma-band power between movements in the contralateral and ipsilateral directions to the average power in spectrograms from just contralaterally directed movement. First, spectrograms were generated in the same manner described above for data from each microwire. Next, the power in the region between 30 Hz and 80 Hz, for times between -500 msec and 0 msec, was averaged to a single value. Once these averaged powers were obtained for each nonpenetrating microwire (independently calculated for each direction of movement), the values for the contralateral direction were re-referenced against those of the ipsilateral direction, then normalized by division to the contralateral values. In this way, percent change of gamma-band power between contralateral and ipsilateral directions of movement was obtained for each channel in the nonpenetrating microwire array.

Pairwise cross-correlation analysis between each set of nonpenetrating microwires was performed on neuronal recordings from a period during arm movement to explore the strength of the linear relationship between the signals recorded by nonpenetrating microwires within close proximity. Because the correlation metric indicates the degree to which two sequences are linearly related, this estimation of independence, while not a complete metric, can approximate the possible usefulness of the high spatial-resolution recording afforded by the nonpenetrating microwire devices. In particular, the correlation analysis should help to clarify whether the nonpenetrating microwire array could be replaced

by a single large electrode, or if the tighter spacing of the nonpenetrating microwires allows for recording of potentially unique signals.

Neural data were bandpass filtered to 30–80 Hz. For each movement trial, one second of filtered data was used to generate pairwise correlation coefficients for each combination of channels. For each pair of channels, the resulting correlation coefficients were averaged.

Preprocessing and analysis for continuous decode

Separately, the data were explored to test whether a continuous decode of hand position could be implemented. Neural data recorded during task sessions for both P1 and P2 were lowpass filtered and downsampled to 2 kS/sec. The data were highpass filtered at 1 Hz to attenuate potential confounds with artifacts introduced by the reaching movements. Multitapered spectrograms between 0 and 500 Hz were generated using the Chronux package, with time-bandwidth parameter five, nine leading tapers, and nonoverlapping 250 msec windows. A total of 14 sessions were used for P1, and nine sessions for P2.

To mimic a realtime implementation, the data were further processed so that the decode could operate on continuously presented frames of data. The spectral data were averaged into frequency bins covering 0-5 Hz, 5-13 Hz, 13-30 Hz, 30-80 Hz, 80-200 Hz, and 200-500 Hz. All frequencies within ± 5 Hz of 60 Hz or its harmonics were removed due to line noise contamination. The movement data were downsampled to the same sampling rate as the spectrograms (4 samples/sec). An offset of 150 msec was introduced between the movement data and the spectral data to model delay between neural activity and motor output. The final feature vector z_k consisted of 6 frequency bins per channel and the hand state x_k was represented by a six-dimensional vector comprising x and y position, velocity, and acceleration. These vectors were defined for $k = 1, 2, \dots, M$, where M was the number of samples in the data set.

A standard Kalman filter was implemented to perform the trajectory decode [7], implicitly making the simplifying assumption that a linear relationship existed between x_k and z_k . The likelihood model was defined as

$$z_k = H_k x_k + q_k \quad (5.1)$$

where H_k linearly relates the hand kinematics to the neural features and q_k represents noise in the observation, assumed to be zero-mean and normally distributed with covariance matrix Q_k . Next, the temporal prior was defined to model how the system state, i.e., the hand kinematics, varied over time. This relationship was characterized by A_k , the state transformation matrix, and w_k , the noise term, also assumed to be zero-mean and normally distributed with covariance W_k .

$$x_{k+1} = A_k x_k + w_k \quad (5.2)$$

Again, a linear relationship was assumed in the temporal progression of the hand state.

With these relationships defined, the decoding process required learning the parameters A , H , W , and Q from the training data, then predicting the hand kinematics at each time given the prior estimate of the state and new measurements of neural data. Neural data recorded during two different task sessions were used for training and testing. The parameters were directly calculated from the training data as described in [7] and were assumed to be constant, e.g., $A_k = A$. Additionally, the means of the movement and neural data features were calculated in order to center the data, and the data were orthogonalized using PCA, with tailing principal components contributing less than 1% of the variance discarded. The principal components and means found during training were applied to the testing data to stay as close as possible to the realtime case where such information would be unavailable.

To decode the hand kinematics from the testing data, the prior state estimate was formed, in the time update step, according to

$$\hat{x}_k^- = Ax_k \quad (5.3)$$

with *a priori* error covariance matrix

$$P_k^- = AP_{k-1}A^T + W \quad (5.4)$$

Next, in the measurement update step, the prior state estimate and new neural data were used to update the state estimate and find the posterior error covariance matrix

$$\hat{x}_k = \hat{x}_k^- + K_k(z_k - H\hat{x}_k^-) \quad (5.5)$$

$$P_k = (I - K_kH)P_k^- \quad (5.6)$$

$$K_k = P_k^- H^T (HP_k^- H^T + Q)^{-1} \quad (5.7)$$

The output of the Kalman filter was analyzed by calculating the correlation coefficient between the actual trajectory, recorded during the task session, and the predicted trajectory output from the Kalman filter. To understand which frequencies were important to the Kalman filter, frequency features were averaged into 10 Hz frequency bins between 0 and 500 Hz (from all channels). These narrowband features were tested individually with the Kalman filter, and the correlation coefficients for the x- and y-positions were recorded for each run.

To determine the level of chance in the context of the continuous trajectory decode, the Kalman filter was trained and tested using zero-mean white noise in place of the neural data (but maintaining the kinematic data). The level of chance was estimated as the average correlation across all combinations of training and testing sessions.

Results

Implantation and data acquisition

No difficulties, such as hemorrhage or electrode migration, were encountered during placement, use, or removal of the nonpenetrating microwire arrays. The motor task design was purposefully simple in nature to allow patients to participate in trials even on the first postoperative day after array implantation.

As noted previously, microwires have significantly higher electrical impedance than standard ECOG electrodes. However, the recording system used was originally designed for single unit action potential analysis from penetrating high-impedance sources. This U.S. Food and Drug Administration–approved system handled signals from the nonpenetrating microwire arrays as well as the standard ECoG contacts without modification of the amplification system.

Correlation Analysis

Fig. 5.3 shows the correlation coefficients mapped to each electrode for all devices placed in both patients. P1 showed a decrease in correlation with distance. P2 had an area of high correlation on the anterior side of the device. The posterior half of the array showed drop-off similar to that seen in both arrays placed in P1. The correlation between nonpenetrating microwires in P1 ranged between 50% and 100%; for P2 the range was between 0% and 100%. For both patients, stronger correlation was generally found between closer nonpenetrating microwires. The decay in correlation strength over distance indicates a degree of independence present across the array, i.e., the nonpenetrating microwire array did not act as a single macroelectrode. Additionally, the disparity between correlations in the anterior and posterior regions of P2 is supported by the underlying anatomy. The highly correlated anterior portion of P2 is directly over hand area in primary motor cortex.

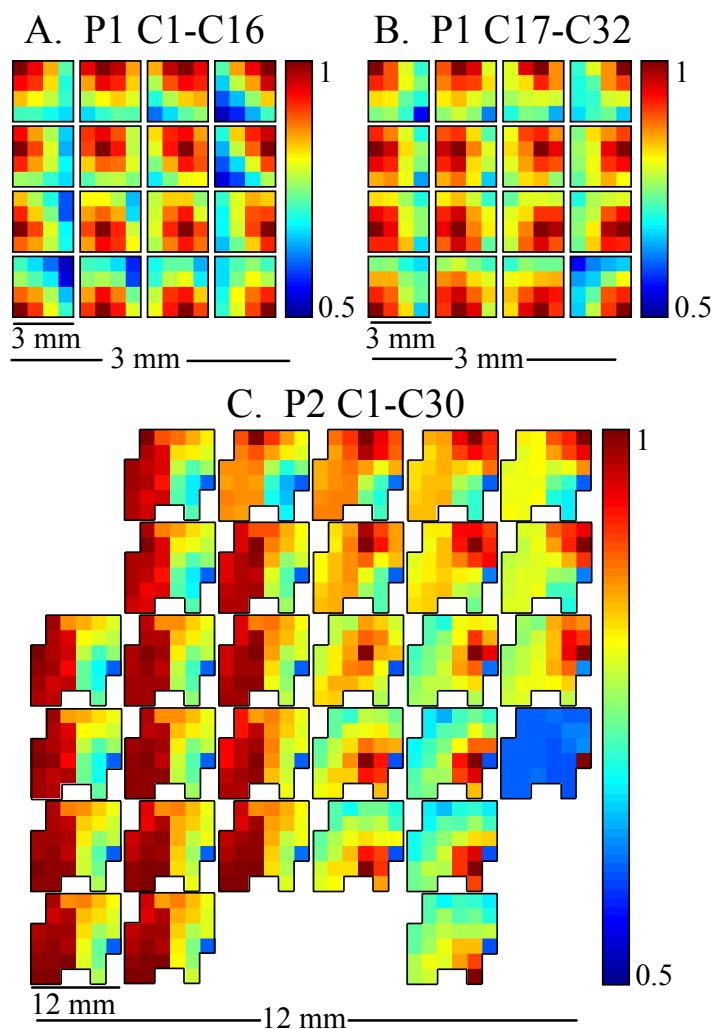


Fig. 5.3. Gamma band (30–80 Hz) pairwise cross-correlations between each nonpenetrating microwire and all other microwires within an array. A: Patient 1 (P1) array correlation, channels 1–16 (orange wire on Fig. 5.1). B: P1 array correlation, channels 17–32 (green wire on Fig. 5.1). C: Patient 2 (P2) array correlation, 30 channels. The physical layouts of the devices in this figure are shown at two scales. At each location in the array, a miniature replica of the entire array indicates the pairwise cross-correlation of that nonpenetrating microwire with all other microwires in the array. The location itself is identifiable in the miniature replica by the dark red pixel showing the autocorrelation. Both arrays in P1 show an inverse relationship between correlation strength and distance. High correlation between microwires in the anterior portion of P2, located over hand area of primary motor cortex, contrasts with the decay seen in the posterior portion, which rested over parietal cortex. The variation evident in correlation strength across arrays suggests that nonpenetrating microwire arrays can capture higher spatial-resolution detail of neuronal signals than standard 5-mm diameter ECoG electrode that might rest over the same surface area. Note that the color scale is optimized to visually emphasize the correlation drop across a device.

Directionality analysis

Patients were able to participate in the motor tasks without significant difficulty. The majority of movements were relatively stereotyped, and only movements within a standard deviation of the average path were used. As the recording properties of the nonpenetrating microwire system were not well known, signals were initially visually evaluated using a limited frequency range (0–70 Hz). Visual inspection revealed ECoG-like recordings in which some standard features such as interictal spikes could be identified.

Spectrograms were created for each patient by averaging results from a single reaching task session. Visual analysis of the spectrograms revealed significant and consistent patterning consistent with previous analyses, including modulation in the beta band power before and during movement [4]. Although data from only a single nonpenetrating microwire are displayed in Fig. 5.4, these results are representative of data from most microwires in both patients (Fig. 5.5 and 5.6). In general, a substantial increase in gamma band power was noted to occur before movement onset in the contralateral direction, with much less gamma band power being seen related to movement in the ipsilateral direction.

Modulation of power in the lower gamma band was especially noticeable for P1, with activity evident around 30–40 Hz beginning 500 msec before movement in the contralateral direction and quickly dropping off after onset of movement. The corresponding region for ipsilaterally directed tasks in P1 is relatively void of similar activity, showing instead a general attenuation in power over the entire gamma band. Power modulation was also evident across the entire gamma-band in P2.

The outward reach movement was immediately followed by the return movement. Gamma-band activity, while generally increased prior to movement, is evident during the outward reaching movement. This increased activity is presumably representative of planning for the return movement. For example, in Fig. 5.4, P2 Ipsilateral (-0.1 sec, 75–100 Hz), upper gamma band power increases significantly during outward movement. This increase in power occurs approximately 500 msec before initiation of the return movement.

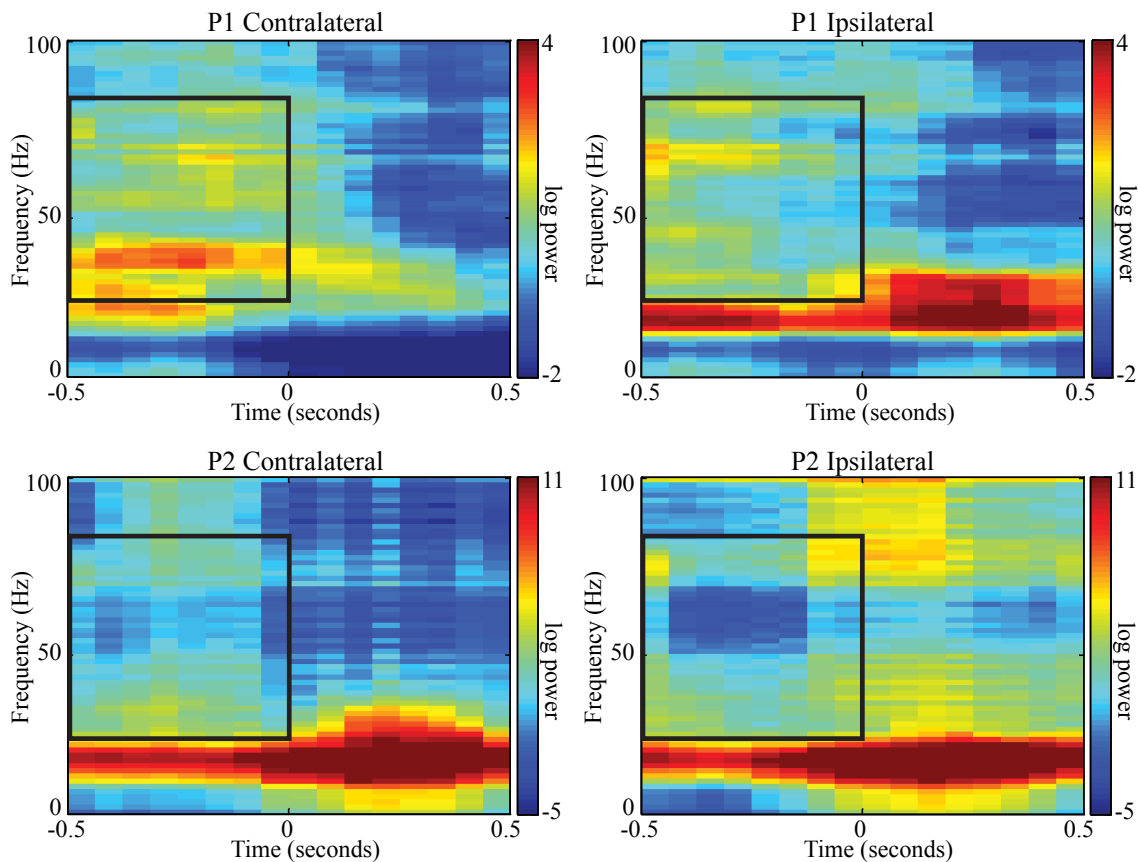


Fig. 5.4. Spectrograms from a single nonpenetrating microwire for each patient demonstrating increased power in the gamma band during the planning phase for movement in the contralateral versus the ipsilateral direction. These spectrograms are aligned at the 0-sec tick to an outward reach movement. Recorded data from the nonpenetrating microwires were band-pass filtered to 5–150 Hz. Spectrograms were generated using the Chronux routines with a moving window of 250-msec and 50-msec step size; additionally, spectrograms were normalized to the average spectrum across time within the 1-sec window as described in the Methods section. Movement in the left column is toward the target contralateral to hemisphere in which the array was implanted; movement in the right column is toward the ipsilateral direction. The inlaid boxed area represents an outline of the gamma band for the planning stage evaluated in Fig. 5.5. Although only a single electrode is shown, the results are representative of most electrodes on each array. Complete spectrograms for all electrodes are included in the Supplemental Material. Patterns in the spectrogram, such as modulation in the Beta-band with respect to movement and planning, are consistent with related work [4].

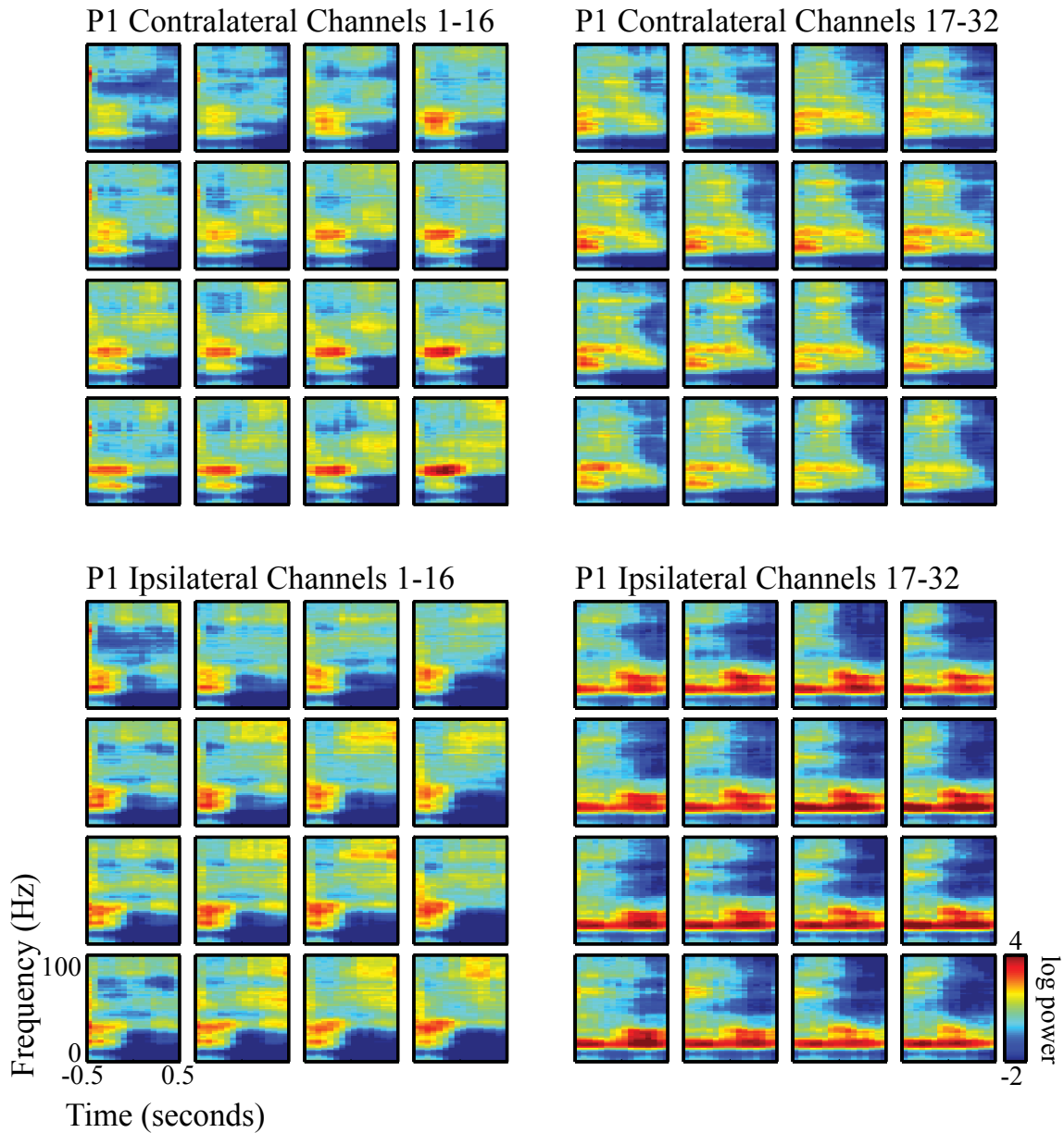


Fig. 5.5. Spectrograms from all nonpenetrating microwires in P1 demonstrating increased power in the gamma band during the planning phase for movement in the contralateral versus the ipsilateral direction. These spectrograms are aligned at the 0-sec tick to an outward reach movement. Recorded data from the nonpenetrating microwires were band-pass filtered to 5–150 Hz. Spectrograms were generated using the Chronux routines with a moving window of 250-msec and 50-msec step size; additionally, spectrograms were normalized to the average spectrum across time within the 1-sec window as described in the Methods section. The upper figures show spectral content for movement toward the target contralateral to implantation hemisphere; the lower figures represent movement toward the ipsilateral direction.

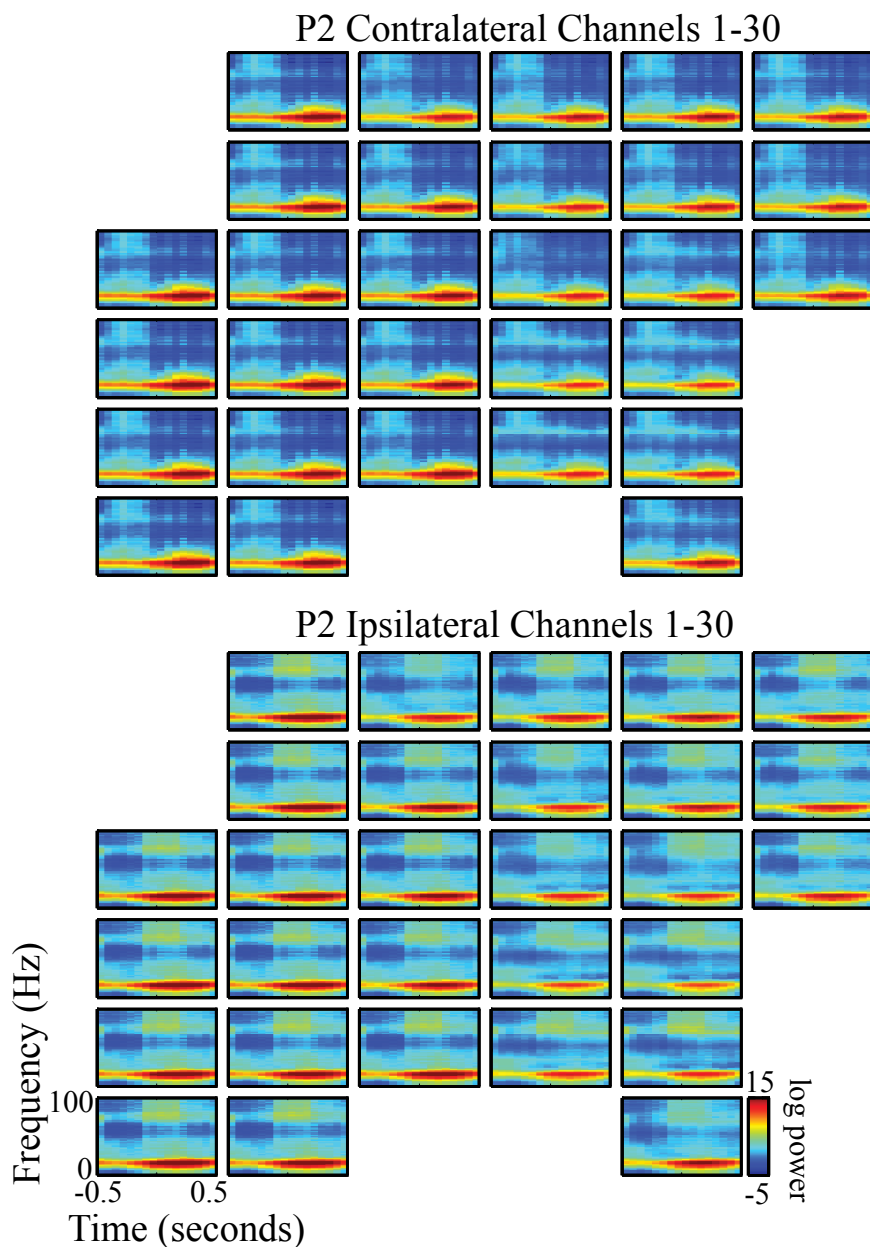


Fig. 5.6. Spectrograms from all nonpenetrating microwires in P2 demonstrating increased power in the gamma band during the planning phase for movement in the contralateral versus the ipsilateral direction. These spectrograms are aligned at the 0-sec tick to an outward reach movement. Recorded data from the nonpenetrating microwires were band-pass filtered to include 5–150 Hz. Spectrograms were generated using the Chronux routines with a moving window of 250-msec and 50-msec step size; additionally, spectrograms were normalized to the average spectrum across time within the 1-sec window as described in the Methods section. The upper figures show spectral content for movement toward the target contralateral to implantation hemisphere; the lower figures represent movement toward the ipsilateral direction.

Similar activity is evident, albeit to a lesser degree, in P2 during planning for the outward movement.

Fig. 5.7 shows the percent change in average gamma-band power during planning for movement in the contralateral versus the ipsilateral direction for 500 msec preceding movement. The difference between these mean values was reasonably substantial. This metric revealed patterns consistent with the underlying anatomy. For example, in P1 channels 17–32 were placed over upper extremity primary motor cortex as confirmed intraoperatively with phase reversal of the SSEP signal. These channels intended to be placed over the expected hand area, with channels 1–16 being placed closer to the expected face area. Channels 17–32 showed significantly higher directional preference as indicated by 20–30% increase in signal power over 14 of 16 microwires when direction of movement changed from ipsilateral to contralateral targets. Channels 1–16 showed very small gains of less than 10%. In P2, extraoperative stimulation confirmed that the majority of the array was over primary hand motor cortex with the higher numbered contacts laying over the postcentral gyrus. Gamma-band power increase follows the gyral contours, with nonpenetrating microwires known to record over hand area indicating 40 to 60% change in power for movement in the contralateral direction. Microwires over parietal cortex recorded slightly lower changes in power (30–40%), whereas microwires over the Rolandic vein recorded the lowest changes (around 20%).

Perhaps most interesting, however, is the level of detail evident in gradients in the percent change visible across both arrays. With only 1 or 2 mm spacing between contacts, an entire nonpenetrating microwire array fits into the area covered by one or two standard ECoG electrodes. Individual microwire contacts are clearly recording activity not fully present in other channels in the array. These results suggest binary classification between movements in grossly contralateral or ipsilateral directions would be possible using millimeter-spaced microwires.

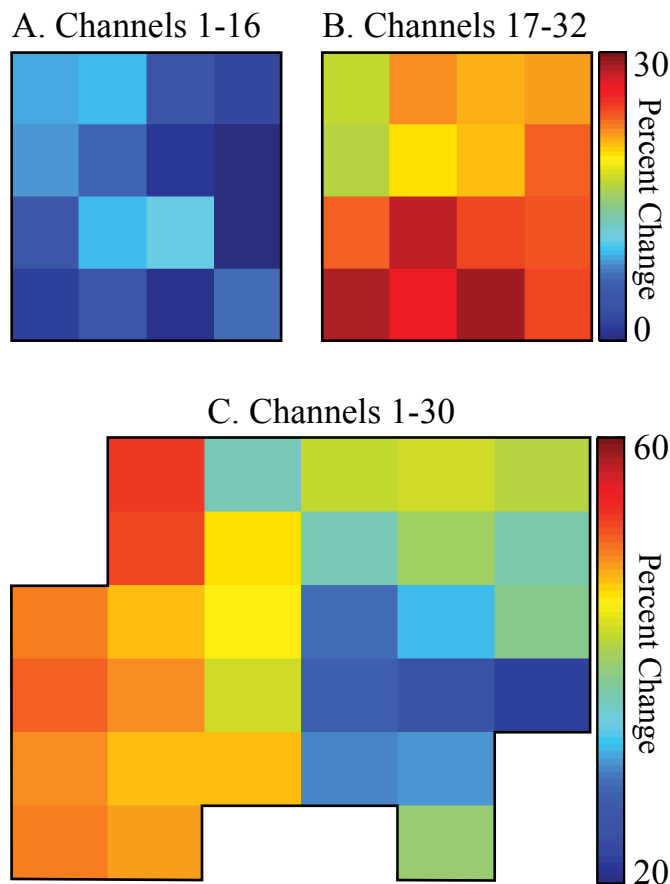


Fig. 5.7. Plots showing, for each nonpenetrating microwire channel in each patient, the percent change in average gamma-band power during planning for movement in the contralateral direction over movement in the ipsilateral direction. After generating spectrograms for each channel as shown in Fig. 5.4, values for frequencies between 30 and 80 Hz and the full 500 msec before movement were averaged to a single value representative of the power over the entire gamma band during the movement planning phase. The difference between these mean values, normalized to the contralaterally directed mean values, is shown above. In A and B, percent change between contralaterally and ipsilaterally directed movement is shown for both electrode arrays implanted in Patient 1. The disparity in magnitude of percent change between arrays is indicative of the underlying structure; channels 17–32 were located over upper extremity primary motor cortex whereas channels 1–16 were located more inferiorly along the precentral gyrus. In C, percent change between contralateral and ipsilateral direction is shown for all 30 channels in Patient 2. The patterns evident in C also correspond closely to the underlying anatomy as noted in the Discussion section.

Continuous trajectory decodes

In a separate analysis, a Kalman filter was implemented to decode the continuous trajectories of the hand movements during the reaching task sessions. As an initial step to verify that there was some basis to the Kalman filtering approach, each task session was used as both the training and the test set. The correlation between the Kalman filter's predicted hand position and the actual position were calculated to evaluate performance. With the same data used for both training and testing (14 task sessions for P1, and 9 task sessions for P2), the mean and standard deviation of the correlations for x- and y-position of P1 was 0.76 ± 0.18 and 0.78 ± 0.17 respectively; for P2 they were 0.76 ± 0.16 and 0.73 ± 0.14 , respectively. That the parameters A, H, W, and Q could be learned and then statically reapplied to the data indicates that linear relationships persisted, at least on this short time scale, between hand kinematics and the neural data.

As expected, performance was lower when the Kalman filter was run on separate data for training and testing, although in some cases performance was still tolerable (see example, Fig. 5.8). The level of chance was estimated by running the Kalman filtering with white noise instead of neural data, for all combinations of training and testing sessions (Table 5.1). To evaluate the performance of the Kalman filter, all possible pairs of task sessions were used as training and testing sets for each patient, under the constraint that the test set had to have occurred later in time than the training set (Fig. 5.9). With 14 task sessions for P1, there were 91 possible training and testing pairs; for P2, there were nine task sessions and 36 possible pairs. The mean and standard deviation of x-position correlation across these pairings was 0.13 ± 0.10 for P1 (48 of 91, or 52.7% above chance) and 0.19 ± 0.15 for P2 (27 of 36, or 75.0% above chance). For the y-position, correlations

Table 5.1 Level of chance for all kinematic variables, for each patient.

	x-pos	y-pos	x-vel	y-vel	x-accel	y-accel
P1	0.08	0.08	0.06	0.06	0.04	0.04
P2	0.09	0.07	0.06	0.06	0.05	0.04

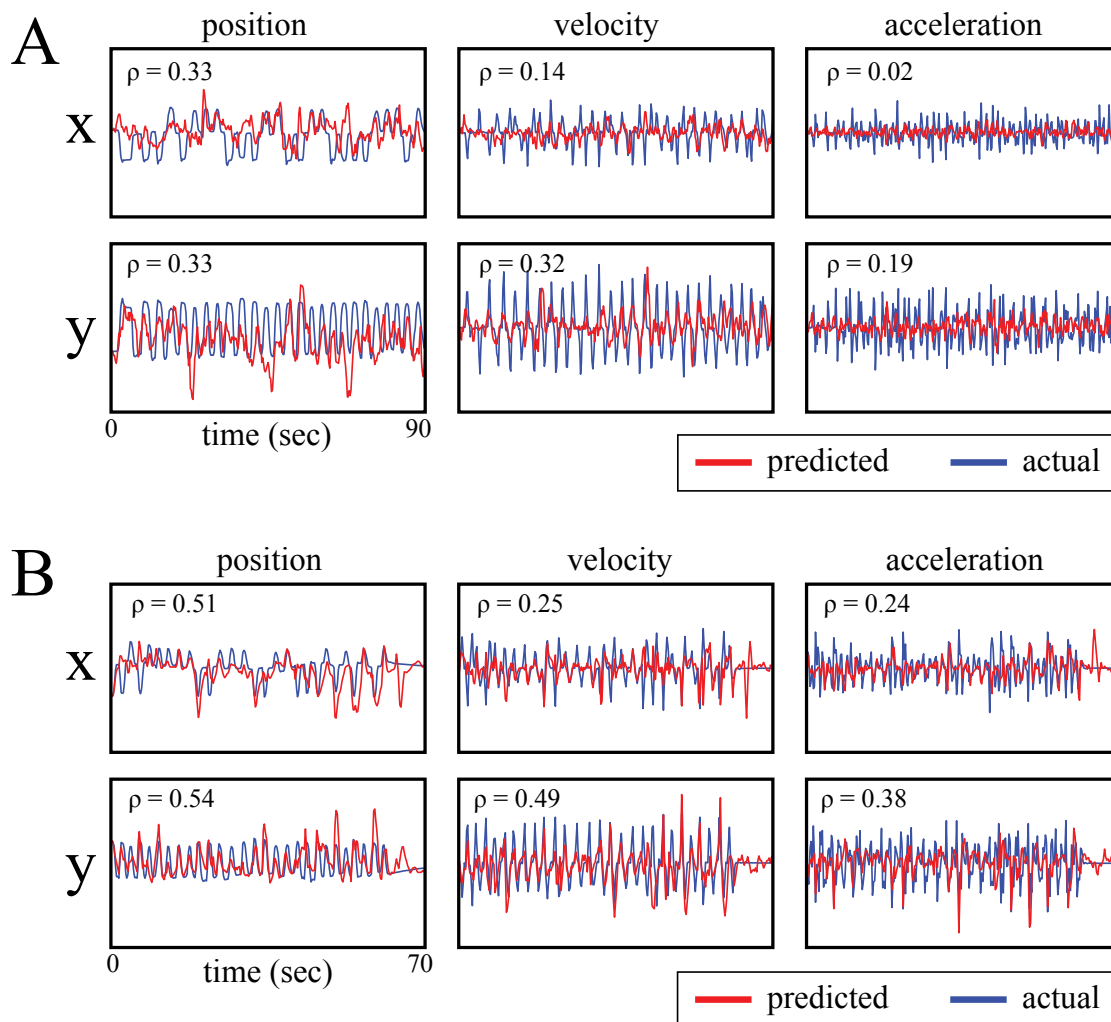


Fig. 5.8. Sample output of the Kalman filter for patients P1 and P2. In Panel A, the Kalman filter was trained on 113 seconds of data recorded during an experimental session with P1, then tested on 90 seconds of data recorded during a subsequent experimental session which began 226 seconds after the first session ended. In Panel B, the Kalman filter was trained on 55 seconds of data recorded during an experimental session with P2, then tested on 70 seconds of data recorded during a subsequent session which began 15 seconds after the first session ended.

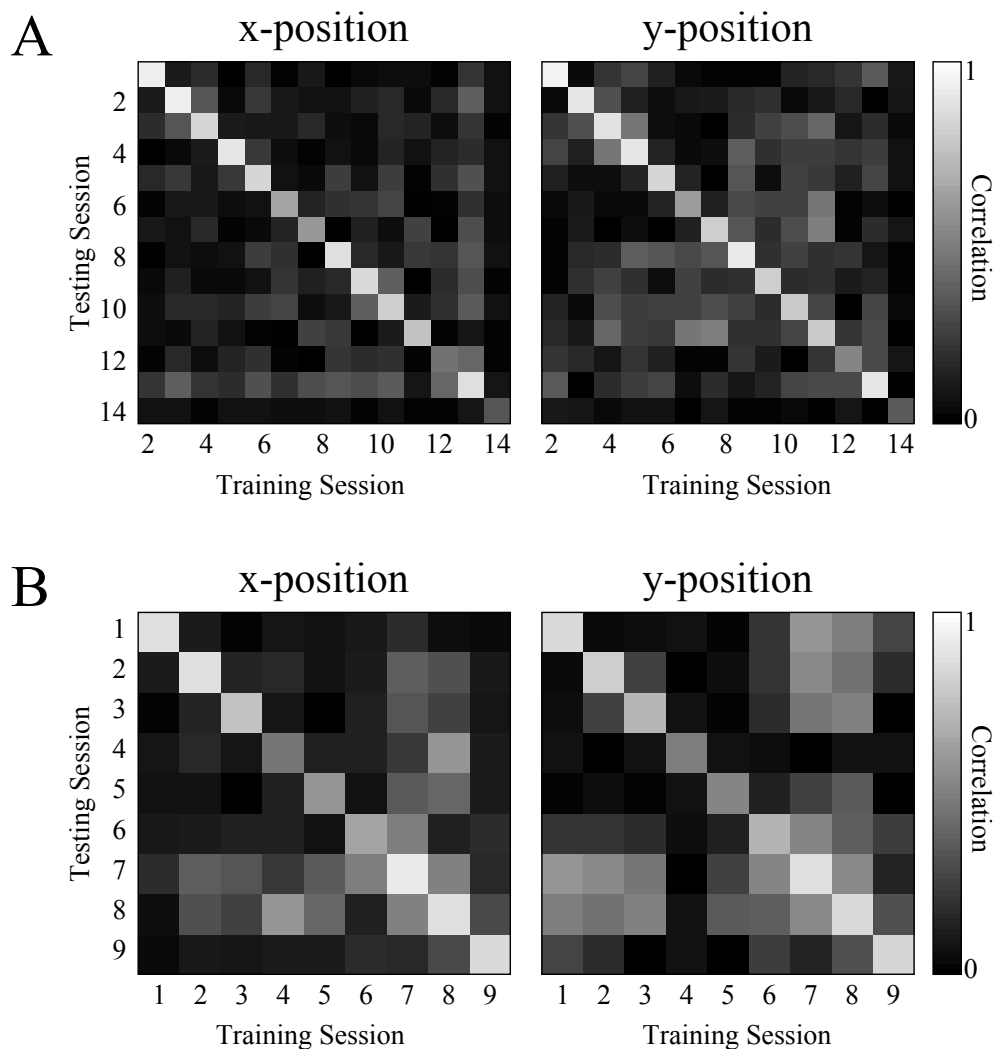


Fig. 5.9. Summary of performance of the Kalman filter for both P1 and P2. Panel A shows results for P1; Panel B shows results for P2. All combinations of experimental sessions were used as training and testing pairs, with the correlation between actual and predicted x and y positions shown in these images. The color scale indicates the magnitude of the correlation between 0 and 1. The diagonal indicates the performance when training and testing on the same data.

were 0.16 ± 0.12 for P1 (65 of 91, or 71.4% above chance) and 0.22 ± 0.19 for P2 (25 of 36, or 69.4% above chance). For P1, 11 of 91 combinations resulted in correlations above the level of chance for all six kinematic variables; 38 of 91 combinations resulted in correlations above the level of chance for just the position variables. For P2, 12 of 36 combinations were above chance for all six kinematic variables, and 20 of 36 combinations were above the level of chance in both dimensions of position.

If the pairs were further constrained such that only consecutive task sessions were used for training and testing, the performance increased: x-position correlations were 0.17 ± 0.13 for P1 and 0.23 ± 0.18 for P2, and y-position correlations were 0.21 ± 0.12 for P1 and 0.25 ± 0.20 for P2. Some pairs demonstrated much higher correlations. The maximums for P1 were 0.39 and 0.49 for x- and y-position, respectively. The maximums for P2 were 0.59 and 0.59, respectively.

To better understand the role of frequency in supporting continuous decodes of hand kinematics, the Kalman filter was run using one feature per channel, which was calculated as the average power in a 10 Hz bin (varied between 0 and 500 Hz). The results from each consecutive pair of task sessions are shown in Fig. 5.10 for both P1 and P2. Both patients' results suggest different responses between the two axes of movement, with strong intertask variation. One trend which appeared fairly consistently was that low frequency content, i.e., <50 Hz, was often important with generally higher correlations than other frequencies. For some pairs, the y-position correlation showed increased performance in the range of frequencies below 200 Hz, and specifically for P1 in the high gamma range, i.e. 80-200 Hz. Fig. 5.8 also indicates that most frequencies between 0 and 500 Hz were important in some subset of results, for either or both of the x- and y-axis movement.

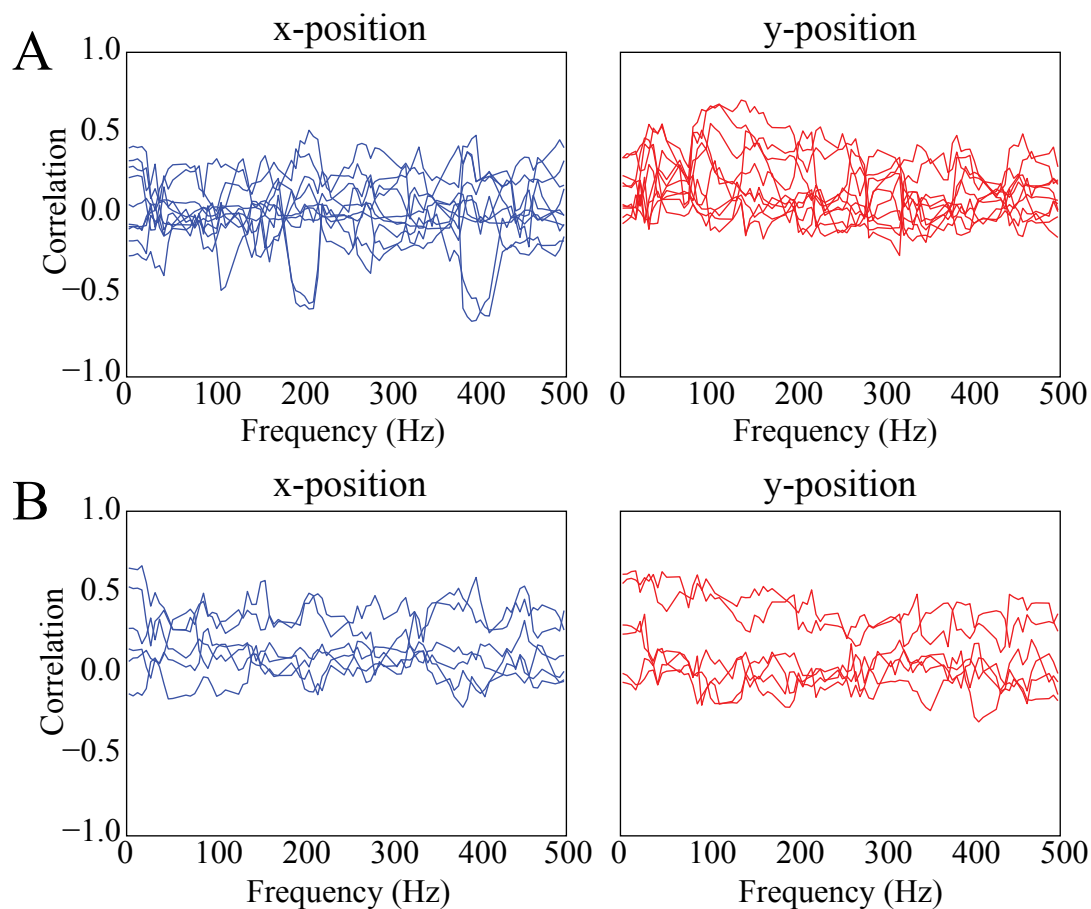


Fig. 5.10. Performance of Kalman filter as a function of frequency for P1 and P2. Results for P1 are shown in Panel A; results for P2 are shown in Panel B. A single feature from each channel, consisting of the average power in a 10 Hz band, was used to perform the prediction. The Kalman filter was executed once for each of 50 nonoverlapping 10 Hz bin between 0 and 500 Hz. For each of these experiments, the correlation between the predicted and actual x and y positions was recorded. These correlations are plotted against frequency in this figure.

Discussion

This study was designed to investigate whether a nonpenetrating microwire device could serve as brain-computer interface (BCI) for a motor neural prosthesis. Neural data recorded during simple motor tasks were examined to understand whether nonpenetrating microwires could acquire neural information potentially useful for decoding motor intentions. Given the known size of human primary motor hand cortex, the microwire grids were designed to allow for the decoding of individual finger and hand movements. As a first assessment, larger and more easily measured arm movements were investigated.

As might be expected from the small size of these devices and the gross motor task chosen, a high degree of interelectrode correlation was found. One would expect that as interelectrode distance increased, the amount of correlation between the signals would decrease. The correlation analysis described previously supported this assumption, with little correlation between nonpenetrating microwires 1 cm apart, whereas those placed 1 mm apart were nearly 90% correlated in the 30–80 Hz frequency ranges. Although the results from this correlation analysis can help direct future array design, the requirements for a BCI device also need be considered.

It is likely that there is significant motor information represented at the scale of single cortical columns. It is possible that a nonpenetrating microwire grid may be capable of acquiring “local field potential-like” signals at this scale. Extracting neural information at this spatial scale may be necessary to provide dexterous intuitive control of a prosthesis. At one extreme, accurate control for fine movements of an external device might require wires with subcolumnar (less than 100 micron) spacing. Such a system could then mimic the level and quality of neural information extracted with penetrating microelectrodes, other than recording action potentials. At another extreme, it is possible that nonpenetrating wires could only accurately measure an “ECoG-like” integrated signal from a broad region of cortex. If the information content available at the pial surface is substantially spatially limited, perhaps to a range of several millimeters, then the best motor decode possible

using a nonpenetrating microwire system may not substantially differ from what is possible through a conventional ECoG grid or possibly epidural electrodes.

The results of this study indicate signal variation can be found even across a spacing of 1–2 mm. This variance in motor neuronal signal pattern differentially noted during a simple reaching task shows that discrete information is being identified. The differential between small-scale signals might be useable for a motor decode [8].

Tuning curves for directional preference of motor cortex cells have been extensively demonstrated in both single unit action potential and also local field potential analysis from penetrating electrodes [9, 10]. It is unknown whether such selectivity will be able to be demonstrated from the neuronal activity derived from nonpenetrating microwires given the discrete size of tuned cortical columns [11]. The data from this study are suggestive that at least a binary classification is possible between two directions, encouraging future studies to more fully define the content of the neuronal signals being recorded.

This study also demonstrated that continuous trajectory decodes are possible using cortical surface potentials recorded over motor cortex with dense grids of microelectrodes. While continuous trajectories have been decoded previously using intracortical field potentials [12, 13], and macroscale surface potentials [13, 14], this is perhaps the first work to demonstrate the concept using surface local field potentials. Significant work remains to improve the accuracy and performance of the trajectory decode. Specifically, adaptive methods could be applied to a number of aspects of the decode process, for example, to update the means and principal components online, and to update the parameters A , H , W , and Q to reflect changing relationships in the neural data over time. Furthermore, although the linear models used for this work were sufficient for demonstration, the true nature of the relationship between motor output and neural activity is likely to be nonlinear. As these issues continue to be explored, the extended Kalman filter, which allows for nonlinear models, may become more appropriate.

Conclusion

The primary finding of this study is that a nonpenetrating microwire platform allows for the recording of human neocortical neuronal activity with spatial resolution better than that available with standard ECoG grids, and that activity recorded at this scale supports motor-BCI applications. The signals recorded from a nonpenetrating microwire array placed over human motor cortex contained sufficient information that discrimination in gross direction could be identified during a simple motor task in the gamma band frequency range. By providing high spatial resolution electrophysiological recordings of human neocortical activity, nonpenetrating microwire arrays may be able to serve as an interface that provides dexterous intuitive control of a limb prosthesis. Additionally, this technology may serve as a novel research tool for studying spatially local neocortical phenomena in health and disease.

References

- [1] G. Schalk, K. J. Miller, N. R. Anderson, J. A. Wilson, M. D. Smyth, J. G. Ojemann, D. W. Moran, J. R. Wolpaw, and E. C. Leuthardt, "Two-dimensional movement control using electrocorticographic signals in humans," *J. Neural Eng.*, vol. 5, pp. 75-84, Mar. 2008.
- [2] E. C. Leuthardt, G. Schalk, J. R. Wolpaw, J. G. Ojemann, and D. W. Moran, "A brain-computer interface using electrocorticographic signals in humans," *J. Neural Eng.*, vol. 1, pp. 63-71, 2004.
- [3] J. J. Van Gompel, S. M. Stead, C. Giannini, F. B. Meyer, W. R. Marsh, T. Fountain, E. So, A. Cohen-Gadol, K. H. Lee, and G. A. Worrell, "Phase I trial: safety and feasibility of intracranial electroencephalography using hybrid subdural electrodes containing macro- and microelectrode arrays," *Neurosurg. Focus*, vol. 25, p. E23, Sep 2008.
- [4] P. J. Uhlhaas and W. Singer, "Neural synchrony in brain disorders: relevance for cognitive dysfunctions and pathophysiology," *Neuron*, vol. 52, pp. 155-168, Oct. 2006.
- [5] G. A. Worrell, A. B. Gardner, S. M. Stead, S. Hu, S. Goerss, G. J. Cascino, F. B. Meyer, R. Marsh, and B. Litt, "High-frequency oscillations in human temporal lobe: simultaneous microwire and clinical macroelectrode recordings," *Brain*, vol. 131, pp. 928-937, Apr 2008.

- [6] S. S. Kellis, P. A. House, K. E. Thomson, R. Brown, and B. Greger, "Human neocortical electrical activity recorded on nonpenetrating microwire arrays: applicability for neuroprostheses," *Neurosurg. Focus*, vol. 27, p. E9, 2009.
- [7] W. Wu, Y. Gao, E. Bienenstock, J. P. Donoghue, and M. J. Black, "Bayesian population decoding of motor cortical activity using a kalman filter," *Neural Comput.*, vol. 18, pp. 80-118, 2006.
- [8] C. Brunner, R. Scherer, B. Graimann, G. Supp, and G. Pfurtscheller, "Online control of a brain-computer interface using phase synchronization," *IEEE Trans. Biomed. Eng.*, vol. 53, pp. 2501-2506, Dec. 2006.
- [9] M. D. Serruya, N. G. Hatsopoulos, L. Paninski, M. R. Fellows, and J. P. Donoghue, "Instant neural control of a movement signal," *Nature*, vol. 416, pp. 141-142, Mar 2002.
- [10] J. Rickert, S. C. Oliveira, E. Vaadia, A. Aertsen, S. Rotter, and C. Mehring, "Encoding of movement direction in different frequency ranges of motor cortical local field potentials," *J. Neurosci.*, vol. 25, pp. 8815-8824, Sep. 2005.
- [11] A. P. Georgopoulos, H. Merchant, T. Naselaris, and B. Amirkian, "Mapping of the preferred direction in the motor cortex," *Proc. Nat. Acad. Sci.*, vol. 104, pp. 11068-11072, Jun. 2007.
- [12] Z. Jun, W. Truccolo, C. Vargas-Irwin, and J. P. Donoghue, "Decoding 3-D reach and grasp kinematics from high-frequency local field potentials in primate primary motor cortex," *IEEE Trans. Biomed. Eng.*, vol. 57, pp. 1774-1784, 2010.
- [13] L. Srinivasan, U. T. Eden, S. K. Mitter, and E. N. Brown, "General-purpose filter design for neural prosthetic devices," *J. Neurophysiol.*, vol. 98, pp. 2456-2475, Oct. 2007.
- [14] T. Pistohl, T. Ball, A. Schulze-Bonhage, A. Aertsen, and C. Mehring, "Prediction of arm movement trajectories from ECoG recordings in humans," *J. Neurosci. Meth.*, vol. 167, pp. 105-114, 2008.

CHAPTER 6

DECODING SPOKEN WORDS USING LOCAL FIELD POTENTIALS RECORDED FROM THE CORTICAL SURFACE

Amyotrophic lateral sclerosis (ALS) and other pathological conditions can damage the brainstem, leaving patients aware but significantly paralyzed and unable to speak, in a condition known as “locked-in syndrome” [1]. In some cases, patients can continue to communicate using residual movements and selection tasks at a few words per minute [2]. Other patients are unable to perform even limited movements [3, 4]. In these situations, directly interfacing with language centers of the cortex may provide more intuitive communication [5].

Penetrating microelectrodes are widely used for brain-computer interfaces (BCIs) because of their ability to record single-unit activity (SUA) as well as local field potentials (LFPs). These electrodes have been used to perform rapid decoding of continuous motor movements from neuronal activity in the primary motor area of human neocortex (e.g., [6]). However, risks associated with impaling the cortex in such fundamental areas motivate the search for alternative methods of acquiring the relevant neural signals. This study used nonpenetrating microwire grids to record neural activity from the cortical surface with high spatiotemporal resolution.

Most studies of speech BCIs using invasive recording techniques have focused on the challenging task of decoding continuous, dynamic speech from the neural representations of formant frequencies [7-9]. In contrast, this study formulated a classification problem with finite sets of words from cortical surface LFPs [10, 11]. Although the potential breadth of

decoded language is therefore inherently limited, this approach has the potential to restore functional and rapid communication with greatly reduced complexity.

This work investigated the trial-by-trial classification of individually articulated words using LFPs recorded on the same micro-ECoG grids evaluated in Chapters 3-5. General performance of the classifier was evaluated. To give a sense of the scale of the underlying cortical processing, the ability to distinguish words from the features of individual microelectrodes was also explored. Recorded data supported accuracies well above the level of chance in classifying up to 10 individual words. Variation in the classification accuracy of individual microelectrodes suggests local, distributed processing for the generation of complex speech articulations.

Methods

Subject and experiment

One male patient who required extraoperative ECoG monitoring for medically refractory epilepsy gave informed consent to participate in an Institutional Review Board-approved study. In addition to the clinical ECoG array, two nonpenetrating microelectrode arrays (PMT Neurosurgical, Chanhassen, MN), each consisting of 16 channels of 70- μ m wire terminating in a 4x4 grid with one-millimeter spacing (Fig. 6.1a), were placed beneath the dura mater, closely approximated to the cortical surface over face motor cortex (FMC) and Wernicke's area (Fig. 6.1b). These arrays were characterized electrically in Chapter 4. The in situ location of clinical and research electrodes on a rendered brain were calculated according to the methods described in [12]. Clinical requirements determined placement of the arrays and duration of the implantation.

During the experiments, the patient rested sitting or reclining in a hospital bed. Researchers verbally instructed the patient to articulate a word multiple times, with approximately one-second intervals between repetitions. A visual cue indicated when the patient should begin speaking, with a visual reference indicating progress through the

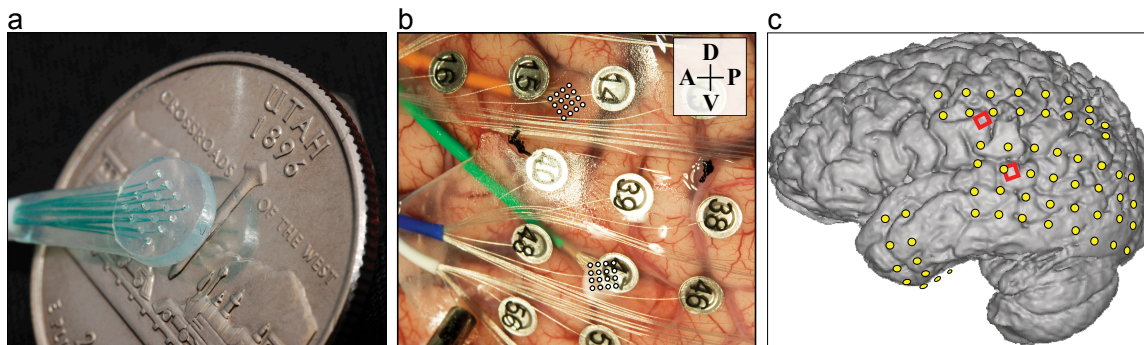


Fig. 6.1. The micro-ECoG grids and surgical placement. These images have appeared in earlier chapters, but are repeated here for convenience. a, A single 16-electrode 4x4 micro-ECoG grid shown next to a U.S. quarter-dollar coin. b, Photograph of micro-ECoG surgical placement; the green wire bundle leads to the array over Wernicke's area; the orange wire bundle leads to the array over face motor cortex. c, Electrode positions in situ; micro-ECoG grids in red and clinical ECoG electrodes in yellow.

repetitions. This process occurred at least once during each session for each of ten words (Table 6.1), with extra trials processed for the words “yes” and “no” to ensure adequate data for preliminary analysis of the data. Sessions lasted approximately one hour and occurred on four consecutive days. For each word, a subset of 45 adjacent trials (30 for training and 15 for decode) containing stereotypical articulation was selected for further analysis. Trials were determined to be stereotyped judging each one on inflection, pitch, and duration. For some words, e.g., “yes” and “hot,” the pronunciation of words varied enough that more than half of the trials were discarded.

Data acquisition and display

Audio data from a microphone and 32 channels of neural data from two 16-channel microelectrode arrays were recorded by a Neuroport system (Blackrock Microsystems, Salt Lake City, UT), with reference tied to the clinical reference lead, during these experiments. The data were amplified, bandpass filtered with cutoff frequencies at 0.3 Hz and 7500 Hz, and digitized at 30,000 samples per second.

Spectrograms were generated using the open-source Chronux package software (chronux.org) with 400-msec windows and 100-msec step size; tapering parameters were

Table 6.1. Listing of words used and numbers of recorded and stereotyped trials.

Word	Trials recorded	Stereotyped repetitions
Yes	166	81
No	160	96
Hot	65	31
Cold	65	48
Hungry	67	48
Thirsty	65	53
Hello	69	34
Goodbye	65	35
More	65	49
Less	67	52

set to a time-bandwidth product of 5 and 9 leading tapers. Spectrograms were smoothed using a mean filter over four 0.9-Hz bands and six 100-msec time steps. Time-series data for the spectrograms were selected from portions of the sessions in which patient–researcher verbal interactions were interspersed between the verbal tasks.

The mean power between 70 and 200 Hz was calculated for data recorded over FMC and Wernicke’s area. The raw data were bandpass filtered (70-200 Hz, Chebyshev Type-I bandpass filter), and then the moving average of the instantaneous power was calculated for each channel. The mean and standard error were calculated across these data separately for FMC and Wernicke’s area.

Feature extraction and classification

Previous studies have used principal component analysis (PCA) [13] to separate frequency-domain features in neural signals [14]. These methods were adapted to perform PCA on features from each microelectrode and trial simultaneously (Fig. 6.2). This updated method was used to explore the incorporation of features across time, frequency, and space.

For the initial results, recorded data from each microelectrode were re-referenced by subtracting the common average of electrodes in the same array. For each spoken word,

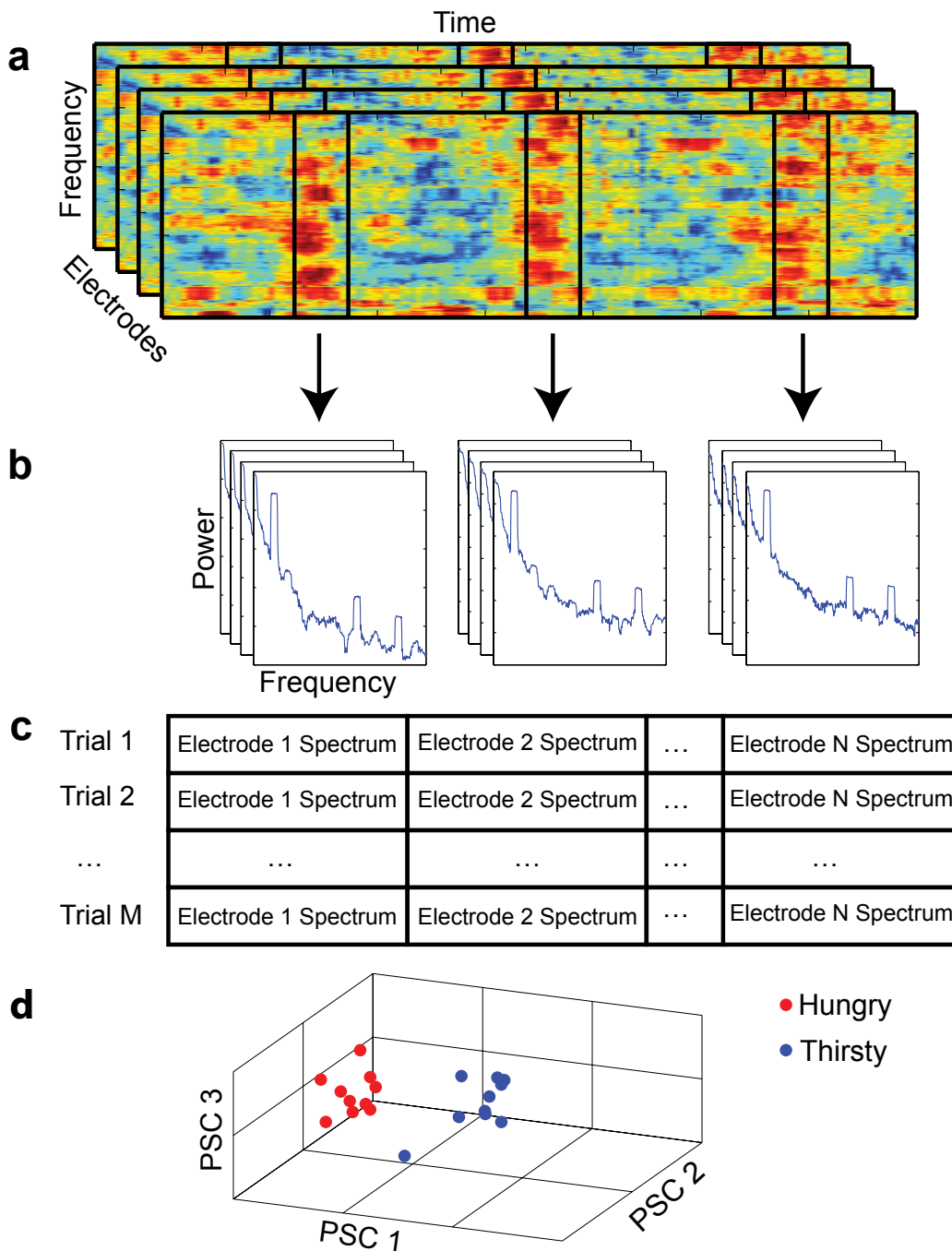


Fig. 6.2. Using frequency-domain structure to decode simultaneously from multiple channels. a, 500-msec windows temporally aligned to spoken words contain frequency-domain structure in a spectrogram of neural data recorded by a single microelectrode over face motor cortex. Axis labels indicate that data from multiple microelectrodes and trials will be used. b, Power spectra were calculated for each trial and each microelectrode. c, For each trial, power spectra from all micro-electrodes were concatenated. Trials were stacked to form a large two-dimensional matrix of microelectrode and trial information. d, Performing principal component analysis on this matrix generated a cluster for each word that allowed nearest-centroid classification.

0.5 seconds of data aligned to the articulation were extracted from all microelectrodes and windowed by a Hann window. The power spectra of these data were calculated by applying a fast Fourier transform (FFT), then multiplying by the complex conjugate of the FFT. Data for frequencies above 500 Hz were discarded, and the remaining power spectra were log-normalized across trials for each microelectrode. At the end of this process, each articulation was represented by 250 frequency-domain features, i.e., the power in 2-Hz bands between 0.3 and 500 Hz, per microelectrode.

Features collected from all microelectrodes for a given articulation were concatenated to form a row vector. Row vectors from multiple articulations were stacked vertically to form a two-dimensional matrix of all available features from multiple microelectrodes and trials. This matrix could be customized by including only features from a subset of microelectrodes or trials. During the training phase, PCA was performed on a matrix consisting of features collected from 15 “training” trials per word. A center of mass, or centroid, was calculated for each word as the mean Euclidean coordinates of all relevant trials’ feature-vectors projected into the principal component space. During the decode phase, projected feature-vectors from 15 additional trials were classified according to their proximity to one of the centroids.

Separately, the data were further analyzed to explore the impact of incorporating temporal dynamics in addition to space and frequency. For this new investigation, recorded data from each microelectrode were re-referenced by subtracting the common average of electrodes in the same array. For each spoken word, a segment of data aligned to the articulation was extracted from all microelectrodes. The raw voltage series covered -0.25 sec to 0.5 sec (relative to the articulation) and were resampled to 100 samples/sec by lowpass filtering and downsampling. Multitapered spectral analysis was performed on 0.5 sec of data aligned to the speech using Chronux. Power spectra were estimated for frequencies between 0-1000 Hz, with 5 leading tapers, and time-bandwidth parameter 9. The spectral data were log-normalized across trials for each microelectrode; the voltage time series were

normalized across trials for each microelectrode. Thus, two sets of data were available to use for features: the downsampled voltage time series (temporal dynamics) and the power spectra (frequency-domain dynamics).

Multidimensional data were unwrapped into a two-dimensional matrix so that each row contained all the included features from all channels for a single trial (Fig. 6.3). Datasets could be merged to include both voltages and power spectra. PCA was again used to decorrelate the data, and a sufficient number of leading principal components were retained to preserve 90% of the variance in the data, regardless of how many variables were originally present in the feature matrix. In this way, biasing of performance due to differences in the distribution of variance between the time and frequency domains was mitigated. Classification proceeded as previously described.

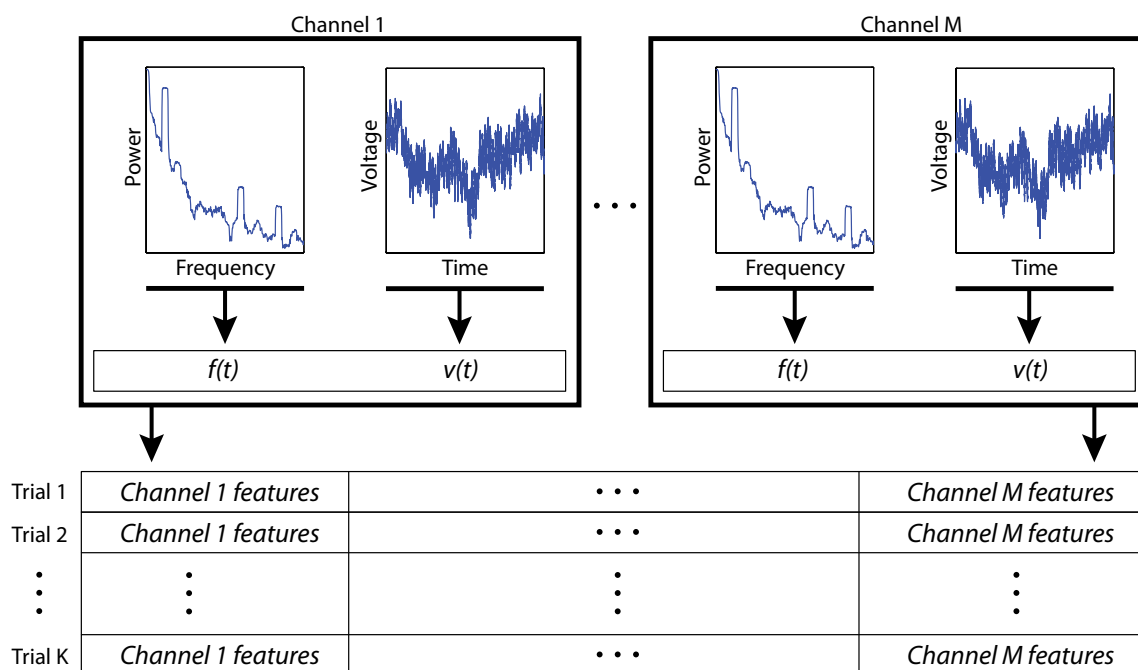


Fig. 6.3. Using time- and frequency-domain structure to decode simultaneously from multiple channels. Power spectra were calculated for each trial and each microelectrode, and were concatenated with downsampled voltage time series. Trials were stacked to form a large two-dimensional matrix of microelectrode and trial information. This figure is analogous to panels a-c in Fig. 6.2, and illustrates that both frequency domain data and voltage data were incorporated from multiple channels in order to capture dynamics in time, space, and frequency.

Evaluation

The classification process was performed using features from combinations of two through ten words. In this case, the term combination refers to the selection of k unordered outcomes from n possibilities where $n=10$ and k ranges between two and ten. When k and n are equal, only one unordered outcome exists and the standard descriptive statistics were not applicable. Otherwise, for each set of outcomes, the mean, median, and standard deviation were computed for the accuracies of the classification results. The performance of the PCA classifier was also evaluated using features from subsets of microelectrodes.

In addition to evaluating the general accuracy of the PCA classifier, the ability of individual microelectrodes to discriminate individual words was also evaluated. Features were selected from single microelectrodes for all two-word combinations and processed by the classifier. The accuracies of all classifications involving a given word were averaged to determine the ability of each microelectrode to discriminate individual words against other possible class assignments.

Classification accuracy was measured against the level of chance for all evaluations. This level was determined by assuming equal likelihood of assignment to any class included in the training process (i.e., the uniform distribution applied to class assignment). For example, if two words were being classified, the level of chance was 0.5 since both potential class assignments were equally likely to be assigned to each trial. Classification accuracies consistently above the level of chance would indicate the exploitation of relevant features from what could otherwise be completely stochastic physiological data.

Results

Activity during task and conversation

Initial observations of neural signals recorded over FMC revealed frequency-domain structure aligned to the individual words during the speech task (Fig. 6.4 through 6.7). Conversely, Wernicke's area was predominantly active during conversation and

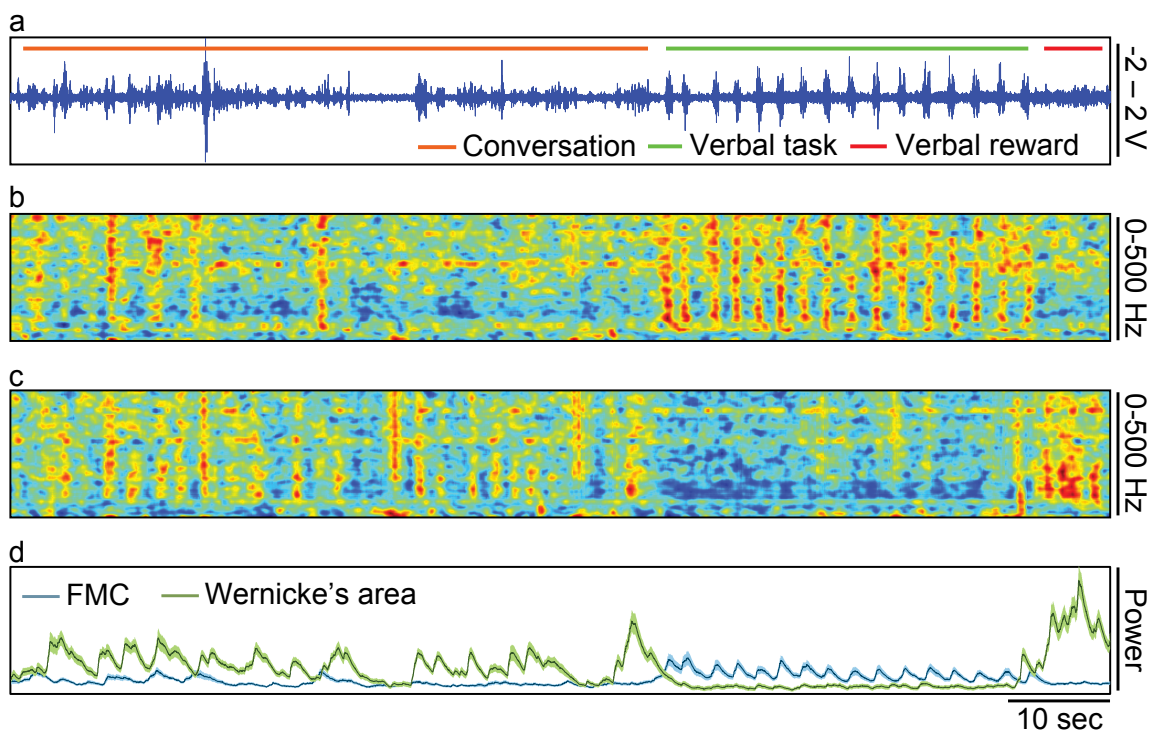


Fig. 6.4. Raw data, spectrogram, and mean power during conversation and task. a, Audio waveform of conversation and verbal task in which the patient repeated the word “yes.” b, Normalized spectrogram of neural data recorded from a single electrode over face motor cortex during the same time period shown in (a). c, Normalized spectrogram of neural data recorded from a single electrode over Wernicke’s area during the same time period shown in (a). d, Mean power and standard error between 70 and 200 Hz for the 16 electrodes over FMC and the 16 electrodes over Wernicke’s area.

while receiving verbal rewards after completing an experiment and was less active during the repeated word experiments. For these figures, data were chosen corresponding to times during the experiments in which patients were performing the verbal task as well as interacting with researchers so as to examine differences between FMC and Wernicke’s area during these different paradigms. Variability in the task-correlated power was present between sessions, and may be due to several factors including medication, arousal, or attention, which could result in the patient varying the strength of articulation; or device-related issues such as micromotion of the electrodes relative to the cortex due to seizure activity.

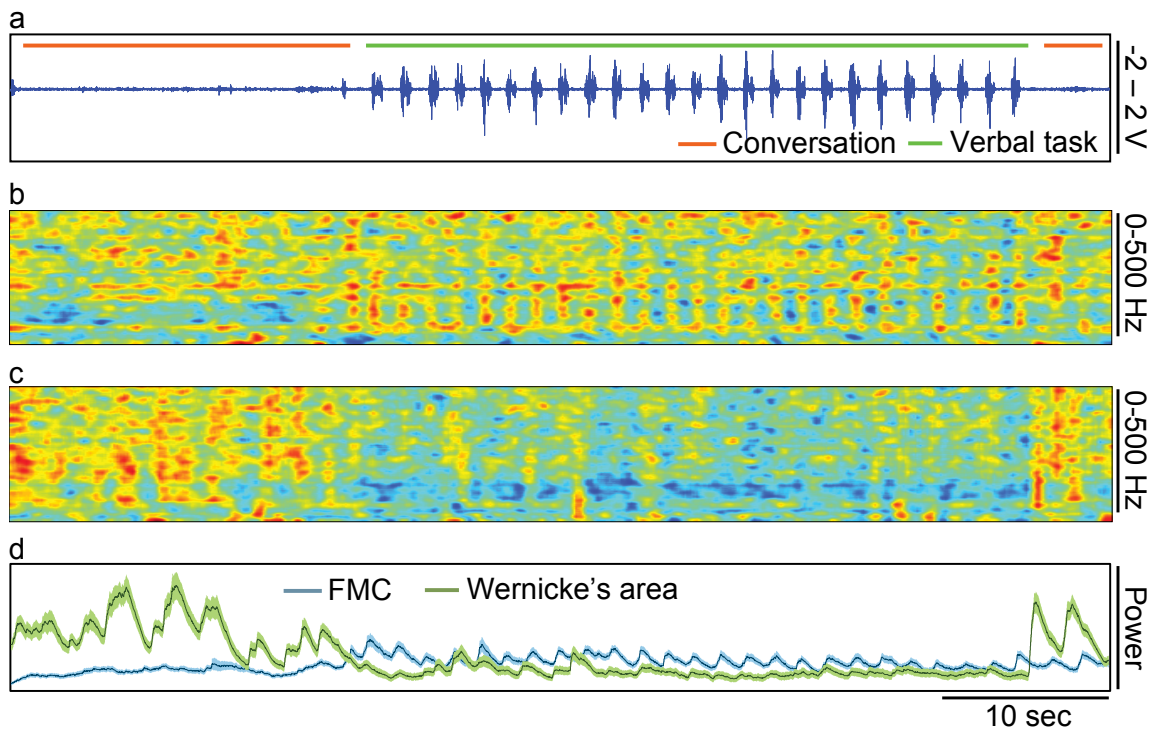


Fig. 6.5. Raw data, spectrogram, and mean power during conversation and task on day 2. a, Audio waveform of conversation and verbal task. b, Normalized spectrogram of neural data recorded from a single electrode over face motor cortex during the same time period shown in (a). c, Normalized spectrogram of neural data recorded from a single electrode over Wernicke's area during the same time period shown in (a). d, Mean power and standard error between 70 and 200 Hz for the 16 electrodes over FMC and the 16 electrodes over Wernicke's area.

Classification better for FMC than Wernicke's area

Classification was performed both separately and jointly for surface LFP data recorded over FMC and over Wernicke's area (Fig. 6.8). Data from microelectrodes over FMC offered the best classification performance with $85.0 \pm 13.1\%$ (mean \pm s.d.) average accuracy over 45 two-word combinations (median performance was 83.3%). Data recorded over Wernicke's area were less classifiable with $76.2 \pm 15.0\%$ average accuracy over the same 45 two-word combinations (median 76.7%) (Fig. 6.8). Joint classification did not improve performance over the level achieved by FMC electrodes alone (0.40 ± 0.43 percentage-point difference in the accuracy of two- through ten-word combinations).

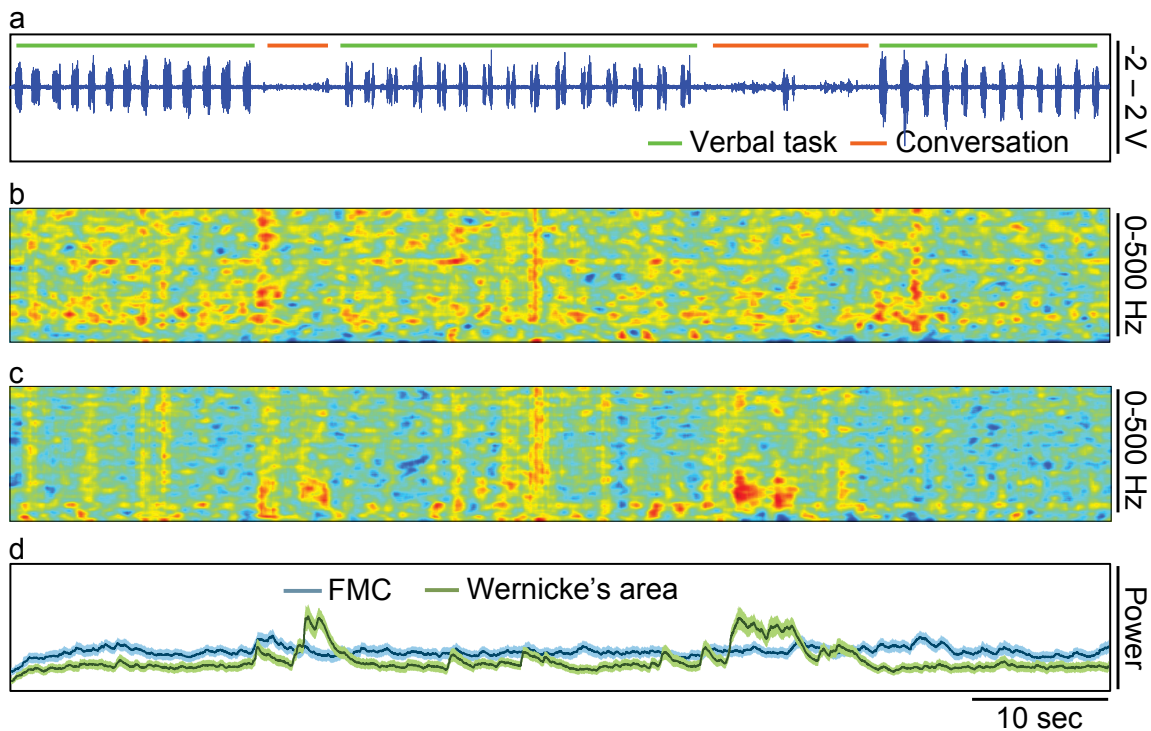


Fig. 6.6. Raw data, spectrogram, and mean power during conversation and task on day 3. a, Audio waveform of conversation and verbal task. b, Normalized spectrogram of neural data recorded from a single electrode over face motor cortex during the same time period shown in (a). c, Normalized spectrogram of neural data recorded from a single electrode over Wernicke's area during the same time period shown in (a). d, Mean power and standard error between 70 and 200 Hz for the 16 electrodes over FMC and the 16 electrodes over Wernicke's area.

Performance from the best five microelectrodes

Selecting the five electrodes over FMC with best overall accuracy improved average classification accuracy compared with using all 16 electrodes. This improvement was consistent in all combinations of words and ranged from 4.0 percentage points ($89.6 \pm 10.8\%$ accuracy, median 90.0, for two-word combinations) up to 20.0 percentage points (48% for the ten-word combination), with 13.5 ± 5.2 percentage points difference on average (Fig. 6.8). Classification accuracies were 16.1 ± 2.3 percentage points higher, on average, when using features from the best five microelectrodes over FMC simultaneously versus using features from these same microelectrodes independently. In contrast, selecting the five highest-performing electrodes over Wernicke's area did not substantially improve

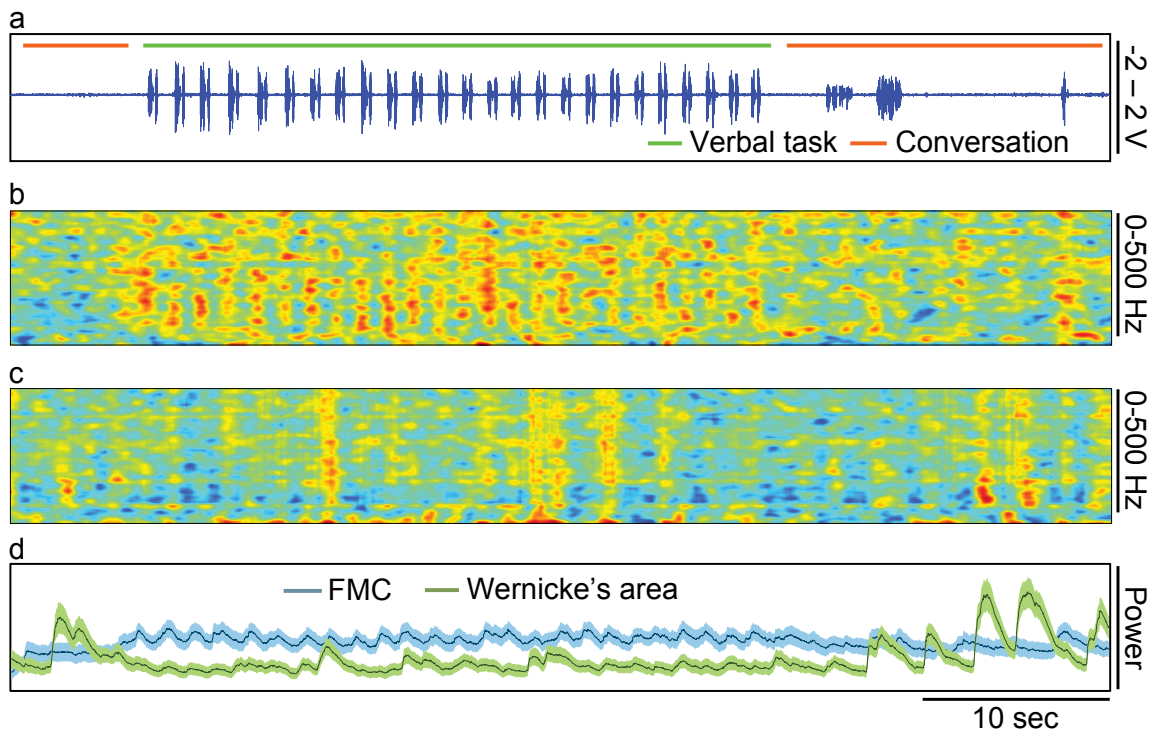


Fig. 6.7. Raw data, spectrogram, and mean power during conversation and task on day 4. a, Audio waveform of conversation and verbal task. b, Normalized spectrogram of neural data recorded from a single electrode over face motor cortex during the same time period shown in (a). c, Normalized spectrogram of neural data recorded from a single electrode over Wernicke's area during the same time period shown in (a). d, Mean power and standard error between 70 and 200 Hz for the 16 electrodes over FMC and the 16 electrodes over Wernicke's area.

performance (1.3 ± 0.7 percentage-point increase on average). Using features from the best five electrodes over Wernicke's area simultaneously resulted in classification accuracies 5.0 ± 0.3 percentage points higher than using features from the same electrodes independently.

To further investigate the importance of time and frequency parameters to the classification process, two additional analyses were performed. Classification accuracy was evaluated using each of the features individually for the two-word classification case. This analysis revealed that at 20 Hz, accuracy began to rise above chance, peaking at 110 Hz and remaining above chance through 500 Hz. Classification accuracy was also evaluated using varying time windows for the two-word classification case. Comparing windows of 0.1, 0.25, 0.5, and 0.75 seconds, we observed median accuracies of 74.0%, 81.2%, 89.6%, and 88.1%, respectively, using the best five channels.

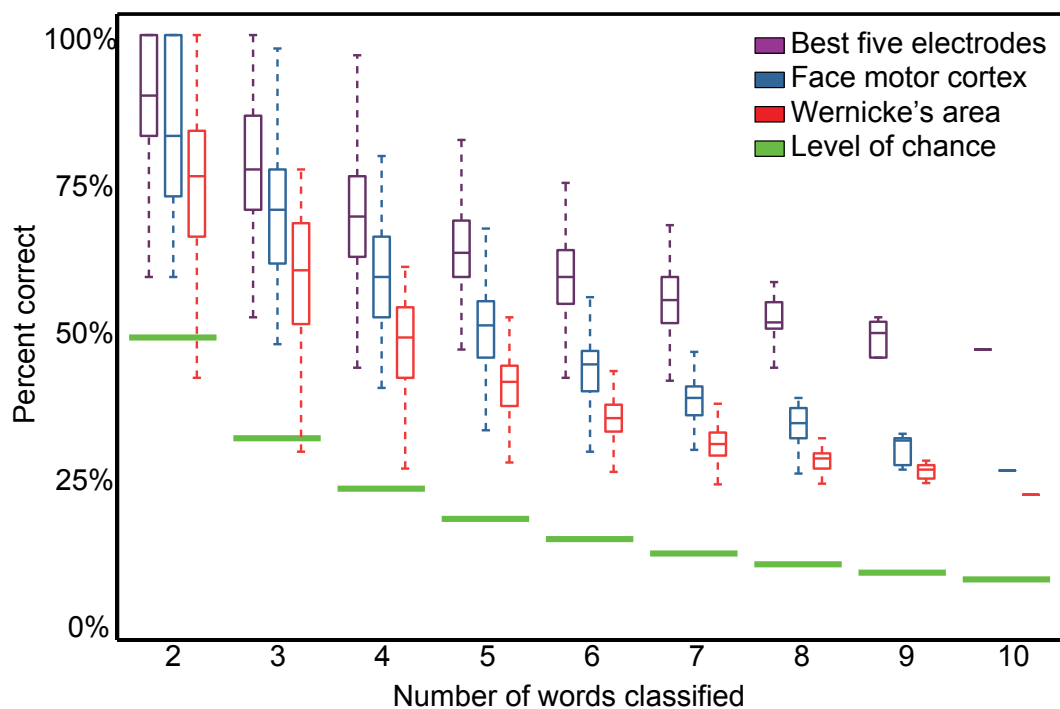


Fig. 6.8. Classification accuracy for combinations of two through ten words. The distribution of classification accuracies from performing each combination of two through ten words is shown. Results are shown using features from all 16 electrodes over FMC; features from all 16 electrodes over Wernicke's area; and features from the best 5 electrodes over FMC.

Word-by-word analysis

To illustrate general ability to discriminate word pairs, decodability matrices were constructed for microelectrodes over FMC (Fig. 6.9a) and over Wernicke's area (Fig. 6.9b). In these figures, the classification accuracy for a pair of words is indicated at the intersection of the two words' row and column indices. Data were obtained from classification using features from the best five electrodes over each area. Over FMC, classification accuracy ranged from 53% ("hello" vs. "more") to 100% accuracy ("yes" vs. "no," "hot" vs. "hungry," and others). While a few of these word pairs were not easily distinguished by the classifier, 40 of the 45 possible pairs had 80% classification accuracy or better. Over Wernicke's area, classification accuracy ranged from 36.7% ("hot" vs. "goodbye") to 100% ("yes" vs. "hot," "no" vs. "hot," and others), and 15 of the 45 word pairs had 80% classification accuracy or better.

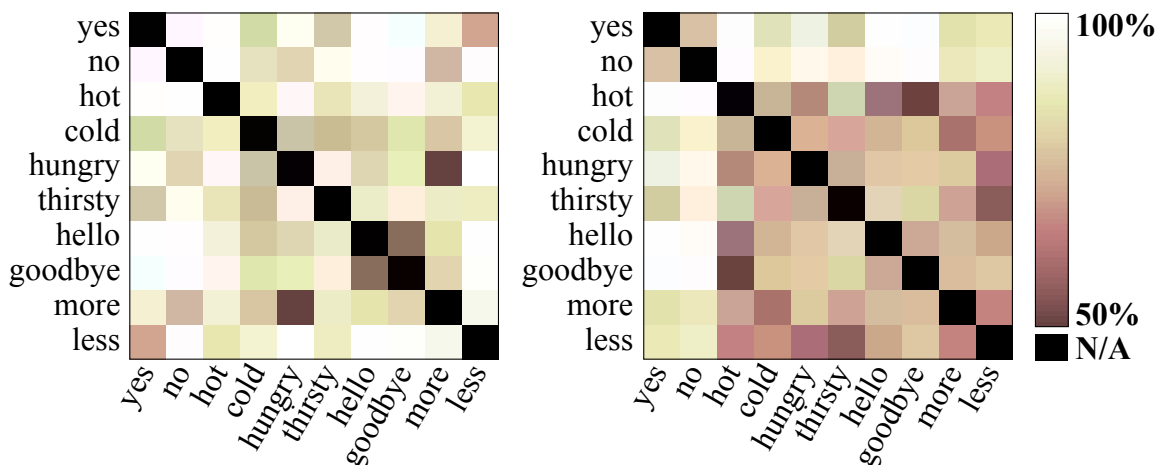


Fig. 6.9. Decodability matrices for FMC and Wernicke's area. The classification accuracies of all word pairs are shown for FMC (left) and Wernicke's area (right) using features from the best five electrodes over each area. In each square plot, the intersection of a row and column indicates the classifier's accuracy for that word pair. The diagonal is marked with black squares indicating the irrelevant case of classifying a word against itself.

Topography and scale

Neighboring electrodes classified different words most accurately. For example, one electrode over FMC classified the word “no” with 89.3% average accuracy (average of all two-word classifications involving the word “no”), while a neighboring electrode just 1 mm away classified the word “less” with 87.8% average accuracy (Fig. 6.10a, middle two electrodes in the top row). Of the 16 electrodes over FMC, 15 had a neighboring electrode within 1.4 mm (including diagonally situated neighbors) whose most accurately classified word, with at least 75% accuracy, was different. Fourteen of the 16 electrodes over Wernicke's area met the same criterion (Fig. 6.10b for reference).

Conversely, neighboring electrodes classified the same word differently. For example, one electrode over FMC classified the word “hot” with 84.4% average accuracy while a neighboring electrode 1 mm away classified the same word with only 56.7% average accuracy (second column, top two electrodes). Eight out of 16 electrodes over FMC and five out of 16 electrodes over Wernicke's area classified their most accurate word at least 15 percentage points higher than a neighboring electrode classified the same word.

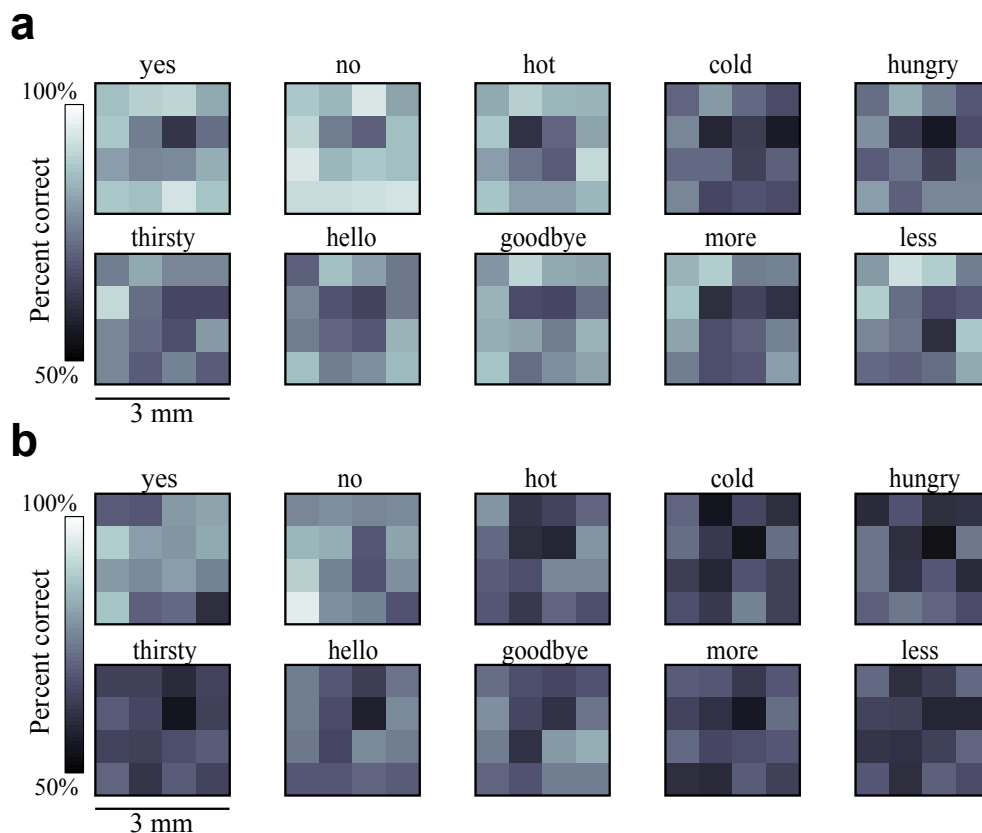


Fig. 6.10. Topography of performance by individual electrode and word. a, The topography of classification accuracy is shown for the microelectrodes resting over FMC. b, The topography of classification accuracy is shown for the microelectrodes resting over Wernicke's area.

Features in time and frequency

In a separate analysis, the performance of the classifier was evaluated using dynamics in space, time, and frequency (Fig. 6.11). With features from all channels included, the average two-word classification accuracy using only the power spectra without temporal dynamics was 88.7%, and using only the voltage time-series it was 90.8%. The same metric for the ten-word classification was 54.7% and 74.0% respectively. Combining features from these individual datasets improved performance relative to the individual case: incorporating both the voltage time series and the power spectra as features, the two- and ten-word classification accuracies were 95.3% and 86.0%.

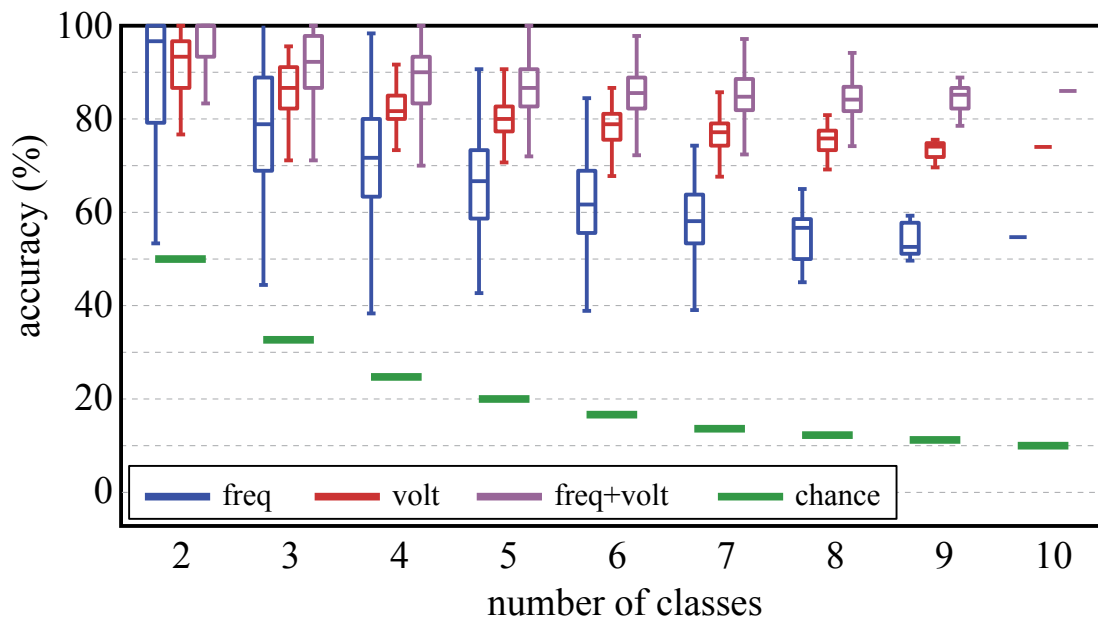


Fig. 6.11. Comparing frequency and voltage as features in the classification. The speech classification was performed using only frequency domain features, only voltage features, and with combined voltage and frequency features. In each case, the features were decorrelated using PCA, and the same number of principal components was retained. This figure shows the performance, for combinations of two through ten words simultaneously classified, for each of these three cases.

The classification was also performed with single features from the voltage and power spectra datasets to understand where in time and frequency the most useful information resided. In the frequency domain, peak performance occurred in very low frequencies between 3-8 Hz, and between 80 and 100 Hz, with a broad bolus of generally higher performance between approximately 50 Hz and 180 Hz (Fig. 6.12). In the case of the voltage time series, peaks occurred at 0 msec, and between 130-180 msec (Fig. 6.13).

Discussion

Surface LFPs support fast, accurate BCI

These results demonstrate that classification of articulated words from surface LFPs recorded on micro-ECoG grids can be performed both rapidly, i.e., within 500 msec of the start of articulation, and with accuracy well above the level of chance. No patient training

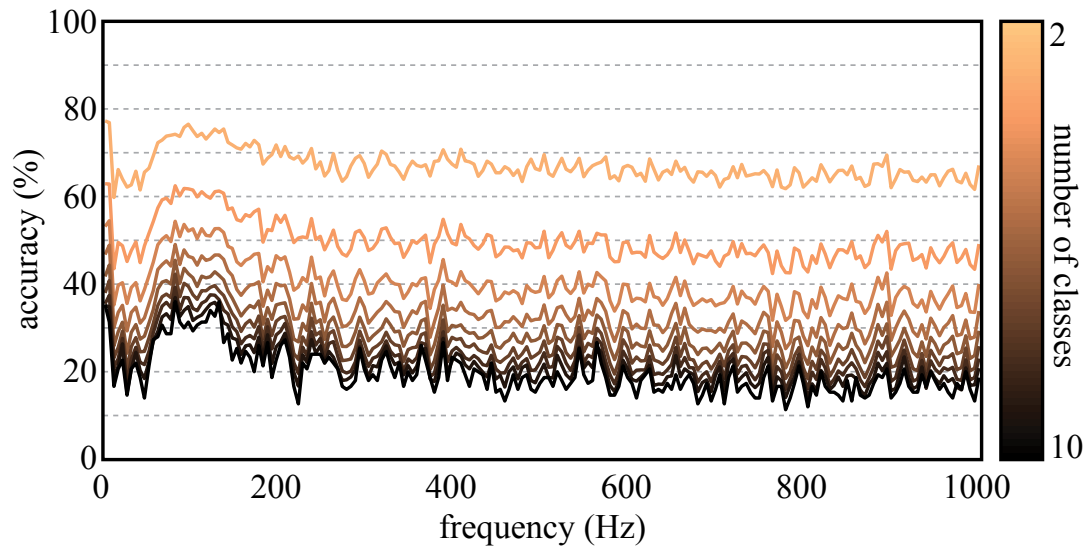


Fig. 6.12. Performance of the speech classification as a function of frequency. The speech classification was performed using a single feature from each channel of data, consisting of a single bin of power in the frequency domain for frequencies between 0 and 1000 Hz. The average accuracy for two through ten words classified simultaneously was recorded, and plotted here against frequency. The color indicates the number of words simultaneously classified.

preceded the initial experimental session, so that classification was performed on features likely representing intuitive language processes. These results demonstrate the potential of using microelectrodes designed to match the scale of cortical information processing in BCI applications.

Studies of ECoG signals have shown that gamma band modulation is correlated to motor actuation and occurs in more localized fashion, both temporally and spatially, than is evident in lower oscillatory bands [15-20]. A common electrophysiological explanation for this behavior is that gamma oscillations represent the synchronizing (or synchronous) interactions of neuronal assemblies, perhaps cortical columns or macrocolumns, engaged in the parallel processing of common stimuli [21-26]. The coincidence of gamma-band event-related synchronization with motor tasks and the evidence for temporally discrete and topographically consistent modulation suggest this neural source is important to BCI operation. Recording these modulations at the appropriate scale requires grids of microelectrodes approximated to the underlying spatiotemporal processing scale.

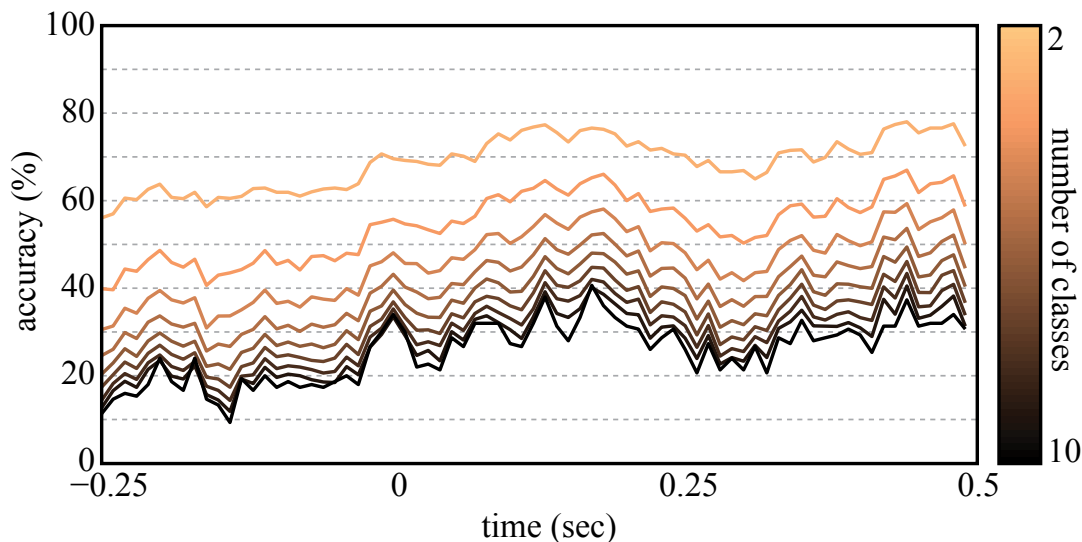


Fig. 6.13. Performance of the speech classification as a function of time index. The speech classification was performed using a single feature from each channel, consisting of a voltage value at a single time index between -0.25 sec and 0.5 sec. The average accuracy for two through ten words classified simultaneously was recorded, and plotted here against frequency. The color indicates the number of words simultaneously classified.

Using microelectrodes approximated to the scale of cortical processing, we found variation of nearly 30% in the classification accuracies (for the same word) of individual electrodes spaced 1 mm apart. Within a 9-mm² space over FMC, almost every electrode had a neighbor within 1.4 mm whose most accurately classified word was not the same. This result suggests that in many cases electrodes recorded activity associated with features not as strongly represented in the data recorded by other nearby microelectrodes. Recoding LFPs at the spatial scale of cortical processing assemblies appears to yield a broad set of relevant, discriminatory features that could serve as the underpinnings of an intuitive and rapid BCI for communication. While optimal parameters of spacing and electrode count are the subject of recent and ongoing studies [27, 28], our findings motivate continued investigation into using micro-ECoG for BCI applications.

Differences in results from Wernicke's area and FMC

While the placement of the microelectrode arrays depended entirely on clinical requirements, specific locations of the grids were chosen to evaluate the potential for deciphering activity from two diverse components of cortical language processing. Classical models of cortical language processing have interpreted aphasic evidence to suggest a conduction path from Wernicke's area to sensorimotor cortex [15, 16], with more recent studies confirming the correlation between superior temporal and inferior frontal regions of cortex [17].

The FMC is known to be involved in controlling the musculature of speech [18, 19], and gamma-band oscillations have been shown to modulate during speech tasks [20]. The considerable range of muscles involved in speech [21] could mean that similar patterns of such neural activity in FMC correspond to similar articulations. The parallel consequence of this relationship, however, is that vocal dynamics such as pitch or inflection may be the result of dissimilar cortical representation and therefore present a potential confound to the classification process. Regardless, the ability of the classifier to distinguish words particularly well from data recorded over FMC may be due to the wide range of cortical representations needed to control the musculature of speech. The varying accuracies of proximal microelectrodes for different words suggest that subunits within FMC may process unique features of articulation, which allowed the classifier to differentiate cortical responses between words.

Wernicke's area has been identified as an important element in high-level cortical language processing [22-25]. Recent studies have shown that distinct subsystems of Wernicke's region activate separately during reception and processing of speech [25, 26] and that Wernicke's area is involved in word and sentence repetition [29, 30]. From the Wernicke's area recordings, substantial broadband spectral power was observed during conversation and while receiving verbal feedback, but less during word repetitions. However, the Wernicke's data recorded during word repetitions still supported classification

accuracies above the level of chance, albeit with less accuracy than was achieved from FMC. Given that the neural signals used in the classification analysis were recorded during the actual vocalization of words, the usefulness of neural signals from Wernicke's area in classification may result from the patient comprehending his own voice [31, 32].

There was less variation in classification accuracies achieved using individual microelectrode over Wernicke's area compared with FMC. As described earlier, selecting the best five microelectrodes did not change accuracy significantly compared with using all 16 microelectrodes, and testing those five microelectrodes individually also did not change accuracy. This finding was opposite that of microelectrodes over FMC, which presented a certain amount of variety across the array. These contrasting observations suggest a more concrete mapping of the neural signal onto patterns of speech articulation in the FMC and a more distributed and abstract encoding of speech in Wernicke's area.

The results of this study suggest that neural activity in FMC is a good candidate for interfacing to communication prostheses. The relatively straightforward mapping of neural activity to motor output suggests that other speech motor and premotor areas, such as Broca's area, may also be good candidates for communication BCIs. In the context of the present experimental paradigm and classification Wernicke's area did not perform as well as FMC in the classification task. However, it is likely, given a more cognitive experimental paradigm and different classification schemes, Wernicke's area would perform as well as or better than FMC.

The importance of features in time, space, and frequency

Including dynamics in dimensions of time, space, and frequency provided better classification performance than when features from only one of those dimensions were used. That temporal dynamics in particular were important is unsurprising given the importance of timing in much of what the brain must do. In particular, the timing of speech-related processing to communicate by formulating vowels, consonants, words, sentences,

and concepts is crucial. The spatial distribution of processing is also unsurprising given the organization present in the cortex at scales ranging from cortical columns to Brodmann areas. Various frequency bands have demonstrated linkage to certain mechanisms of cortical operation [33-35]. Thus, considering that all three dimensions play important roles for neural information processing, it is reasonable to expect that monitoring dynamics in all three dimensions would provide the most information for an algorithmic classification of neural signals.

Limitations

The patient involved in this study suffered from medically refractory epilepsy for many years. While there are many consequences of this condition, one particularly relevant potential outcome is the remapping of language-relevant cortical areas. Insofar as it has been possible to determine using evidence from pre- and post-surgical x-rays and photographs, the anatomical labels indicated in this study are correct; however, such re-mapping could affect conclusions about the functional differences in the activity recorded from electrodes believed to rest over FMC and Wernicke's area.

The nature of the experimental paradigm was such that the patient repeated a few words many times over several consecutive days. It is possible that cognitive language processes gave way to memory-based language processes after many repetitions. While difficult to confirm or disprove, such a change in cortical function could affect cortical representations of speech and could be responsible for less accuracy in the classification of words. This line of reasoning may be especially true for neural activity recorded over Wernicke's area which is involved in more semantic processing. The low cognitive effort required to perform the experimental task likely did not engage Wernicke's area. Verb generation, picture labeling, and other more cognitive tasks have been shown to elicit cortical processing rhythms which may be useful in speech classification contexts [36].

Disregarding the limitations of the dictionary size temporarily, the 500 msec delay between cortical processing and classifier output may be too slow to support conversational speech. Other work has demonstrated a fast 30 msec delay from action potential firing from single units to first audible output [7] for a trajectory-based decode system—a different problem than the decision-based algorithm presented in this study. Furthermore, the nature of a realtime decode mandates rapid sensory feedback for online control, whereas such rapid feedback is not as important for discrete word classification.

Future work

The results of the current study were obtained without any significant patient training. With some preparation, patients could adapt their neural processes to the performance of the classifier and learn to stereotype word articulation. More sophisticated classification algorithms could take advantage of stereotyped articulation to adapt to subtle differences in the cortical representations of different words. More sophisticated feature selection could improve performance as well.

The highest-performing classifications in these results were obtained from cases where classification discriminated between just two words. Although more advanced methods could likely improve accuracy when more words are present, a system performing binary classification could employ straightforward algorithms and require minimal patient training. For example, a method of hierarchical selection, e.g., [37], could provide simple patient control. Investigation into increasing accuracy for larger dictionaries could also provide sufficiently enhanced patient experience to justify the extra effort.

The invasiveness of the microelectrode grids could be further reduced with epidural placement, as has been shown for similar recording devices [27, 38]. Furthermore, a wireless implementation of the system might be practical given the relatively low bandwidth required to capture cortical surface LFPs. A wireless system able to record high-resolution cortical surface potentials could provide a reasonable balance of invasiveness and performance and

improve the quality of life for locked-in patients and others unable to communicate on their own.

The tight interelectrode spacing and small number of electrodes limited the spatial coverage of the microelectrode grid. An optimized grid design with more electrodes would likely cover a larger number of relevant neural signals and allow better decoding accuracy. Optimal interelectrode spacing and coverage is an important area for future research that will have wide implications in feature selection and classification algorithms.

Conclusion

In sum, this work has demonstrated the capabilities of cortical surface LFPs recorded on micro-ECoG grids in classifying spoken words. Having micro-ECoG grids designed to approximate the columnar scale of cortical information processing is a key element in acquiring a rich set of features upon which a communications BCI can operate. The classification of speech using micro-ECoG appears to be a viable approach to restoring limited but useful communication to those suffering from locked-in syndrome.

References

- [1] E. Smith and M. Delargy, "Locked-in syndrome," *BMJ*, vol. 330, pp. 406-409, Feb. 2005.
- [2] P. Majoranta and K.-J. R  ih  , "Twenty years of eye typing: systems and design issues," in *Proc. Symp. Eye Tracking Research and Application*, New Orleans, LA, 2002.
- [3] G. Bauer, F. Gerstenbrand, and E. Rimpl, "Varieties of the locked-in syndrome," *J. Neurol.*, vol. 221, pp. 77-91, Aug. 1979.
- [4] J. Leon-Carrion, P. van Eeckhout, R. Dominguez-Morales Mdel, and F. J. Perez-Santamaria, "The locked-in syndrome: a syndrome looking for a therapy," *Brain Inj.*, vol. 16, pp. 571-582, Jul. 2002.
- [5] N. Birbaumer, "Breaking the silence: brain-computer interfaces (BCI) for communication and motor control," *Psychophysiol.*, vol. 43, pp. 517-532, Nov. 2006.

- [6] L. R. Hochberg, M. D. Serruya, G. M. Friehs, J. A. Mukand, M. Saleh, A. H. Caplan, A. Branner, D. Chen, R. D. Penn, and J. P. Donoghue, "Neuronal ensemble control of prosthetic devices by a human with tetraplegia," *Nature*, vol. 442, pp. 164-171, Jul. 2006.
- [7] F. H. Guenther, J. S. Brumberg, E. J. Wright, A. Nieto-Castanon, J. A. Tourville, M. Panko, R. Law, S. A. Siebert, J. L. Bartels, D. S. Andreasen, P. Ehirim, H. Mao, and P. R. Kennedy, "A wireless brain-machine interface for real-time speech synthesis," *PloS one*, vol. 4, p. e8218, 2009.
- [8] T. Blakely, K. J. Miller, R. P. Rao, M. D. Holmes, and J. G. Ojemann, "Localization and classification of phonemes using high spatial resolution electrocorticography (ECoG) grids," in *Proc. IEEE Engineering in Medicine and Biology Conf.*, 2008, pp. 4964-4967.
- [9] F. H. Guenther, S. S. Ghosh, and J. A. Tourville, "Neural modeling and imaging of the cortical interactions underlying syllable production," *Brain Lang.*, vol. 96, pp. 280-301, 2006.
- [10] S. Kellis, K. Miller, K. Thomson, R. Brown, P. House, and B. Greger, "Classification of spoken words using surface local field potentials," in *Proc. IEEE Engineering in Medicine and Biology Conf.*, Buenos Aires, Argentina, 2010.
- [11] S. Kellis, K. Miller, K. Thomson, R. Brown, P. House, and B. Greger, "Decoding spoken words using local field potentials recorded from the cortical surface," *J. Neural Eng.*, vol. 7, p. 056007, 2010.
- [12] D. Hermes, K. J. Miller, H. J. Noordmans, M. J. Vansteensel, and N. F. Ramsey, "Automated electrocorticographic electrode localization on individually rendered brain surfaces," *J. Neurosci. Meth.*, vol. 185, pp. 293-8, Jan. 2010.
- [13] I. T. Jolliffe, *Principal Component Analysis*, 2 ed. New York: Springer, 2002.
- [14] K. J. Miller, S. Zanos, E. E. Fetz, M. den Nijs, and J. G. Ojemann, "Decoupling the cortical power spectrum reveals real-time representation of individual finger movements in humans," *J. Neurosci.*, vol. 29, pp. 3132-3137, 2009.
- [15] L. Lichtheim, "On Aphasia," *Brain*, vol. 7, pp. 433-484, 1885.
- [16] C. Wernicke, *Der aphasische Symptomenkomplex*. Breslau: Cohn und Weigert, 1874.
- [17] H. Karbe, K. Herholz, G. Weber-Luxenburger, M. Ghaemi, and W. D. Heiss, "Cerebral networks and functional brain asymmetry: evidence from regional metabolic changes during word repetition," *Brain Lang.*, vol. 63, pp. 108-121, Jun. 1998.

- [18] K. Murphy, D. R. Corfield, A. Guz, G. R. Fink, R. J. Wise, J. Harrison, and L. Adams, "Cerebral areas associated with motor control of speech in humans," *J. Applied Physiol.*, vol. 83, pp. 1438-1447, 1997.
- [19] W. Penfield and E. Boldrey, "Somatic motor and sensory representation in the cerebral cortex of man as studied by electrical stimulation," *Brain*, vol. 60, pp. 389-443, 1937.
- [20] N. E. Crone, L. Hao, J. Hart, Jr., D. Boatman, R. P. Lesser, R. Irizarry, and B. Gordon, "Electrocorticographic gamma activity during word production in spoken and sign language," *Neurology*, vol. 57, pp. 2045-2053, Dec. 2001.
- [21] A. Smith, "Speech motor development: integrating muscles, movements, and linguistic units," *J. Commun. Disord.*, vol. 39, pp. 331-349, Sep.-Oct. 2006.
- [22] J. E. Bogen and G. M. Bogen, "Wernicke's region--where is it?," *Ann. New York Academy Sci.*, vol. 280, pp. 834-843, 1976.
- [23] N. T. Sahin, S. Pinker, S. S. Cash, D. Schomer, and E. Halgren, "Sequential processing of lexical, grammatical, and phonological information within Broca's area," *Science*, vol. 326, pp. 445-449, Oct. 2009.
- [24] G. A. Ojemann, "Cortical organization of language," *J. Neurosci.*, vol. 11, pp. 2281-7, 1991.
- [25] V. L. Towle, H.-A. Yoon, M. Castelle, J. C. Edgar, N. M. Biassou, D. M. Frim, J.-P. Spire, and M. H. Kohrman, "ECoG gamma activity during a language task: differentiating expressive and receptive speech areas," *Brain*, vol. 131, pp. 2013-2027, 2008.
- [26] R. J. S. Wise, "Separate neural subsystems within 'Wernicke's area'," *Brain*, vol. 124, pp. 83-95, 2001.
- [27] M. W. Slutzky, L. R. Jordan, T. Krieg, M. Chen, D. J. Mogul, and L. E. Miller, "Optimal spacing of surface electrode arrays for brain-machine interface applications," *J. Neural Eng.*, vol. 7, p. 26004, Apr. 2010.
- [28] M. W. Slutzky, L. R. Jordan, and L. E. Miller, "Optimal spatial resolution of epidural and subdural electrode arrays for brain-machine interface applications," in *Proc. IEEE Engineering in Medicine and Biology Conf.*, 2008, pp. 3771-3774.
- [29] O. A. Selnes, D. S. Knopman, N. Niccum, and A. B. Rubens, "The critical role of Wernicke's area in sentence repetition," *Ann. of Neurol.*, vol. 17, pp. 549-557, Jun. 1985.
- [30] M. A. Naeser, A. Gaddie, C. L. Palumbo, and D. Stiassny-Eder, "Late recovery of auditory comprehension in global aphasia. Improved recovery observed with subcortical temporal isthmus lesion vs Wernicke's cortical area lesion," *Arch. Neurol.*, vol. 47, pp. 425-432, Apr. 1990.

- [31] S. Hirano, H. Kojima, Y. Naito, I. Honjo, Y. Kamoto, H. Okazawa, K. Ishizu, Y. Yonekura, Y. Nagahama, H. Fukuyama, and J. Konishi, "Cortical processing mechanism for vocalization with auditory verbal feedback," *Neuroreport*, vol. 8, pp. 2379-82, Jul 1997.
- [32] P. K. McGuire, D. A. Silbersweig, and C. D. Frith, "Functional neuroanatomy of verbal self-monitoring," *Brain*, vol. 119 (Pt 3), pp. 907-917, Jun. 1996.
- [33] R. T. Canolty, E. Edwards, S. S. Dalal, M. Soltani, S. S. Nagarajan, H. E. Kirsch, M. S. Berger, N. M. Barbaro, and R. T. Knight, "High gamma power is phase-locked to theta oscillations in human neocortex," *Science*, vol. 313, pp. 1626-1628, Sep 2006.
- [34] R. T. Canolty and R. T. Knight, "The functional role of cross-frequency coupling," *Trends Cogn. Sci.*, vol. 14, pp. 506-515, 2010.
- [35] P. Fries, "Neuronal gamma-band synchronization as a fundamental process in cortical computation," *Annu. Rev. Neurosci.*, vol. 32, pp. 209-224, 2009.
- [36] E. Edwards, S. S. Nagarajan, S. S. Dalal, R. T. Canolty, H. E. Kirsch, N. M. Barbaro, and R. T. Knight, "Spatiotemporal imaging of cortical activation during verb generation and picture naming," *Neuroimage*, vol. 50, pp. 291-301, Mar. 2010.
- [37] N. Birbaumer, N. Ghanayim, T. Hinterberger, I. Iversen, B. Kotchoubey, A. Kübler, J. Perelmouter, E. Taub, and H. Flor, "A spelling device for the paralysed," *Nature*, vol. 398, pp. 297-298, 1999.
- [38] E. C. Leuthardt, K. J. Miller, G. Schalk, R. P. Rao, and J. G. Ojemann, "Electrocorticography-based brain computer interface--the Seattle experience," *IEEE Trans. Neural Syst. Rehabil. Eng.*, vol. 14, pp. 194-198, Jun 2006.

CHAPTER 7

CONCLUSION

Brain-computer interfaces are at the frontier of modern technology. The challenges of sensing brain activity, interpreting the brain's commands, and controlling an external device together form a compelling application of engineering and science, requiring the most advanced capabilities in electronics, sensors, and signal processing. Even more motivating is the potential to change lives for the better, with direct applications for paralyzed, locked-in, and traumatically injured patients, and potential impact for many others with pathologies such as epilepsy or Parkinson's disease. Yet, BCIs face significant challenges before their benefits may be realized by actual patients. The most fundamental of these is the challenge to engineer a safe, chronic, and useful interface to the biological tissue of the cortex. The activity of the brain may be sensed in a variety of ways, and selection of the physical interface requires an informed decision balancing the needs of the application and the extent of invasiveness of the recording electrodes. A physical interface which captures cortical surface potentials would be attractive since it could be located close to the signal source, but would not damage the tissue by penetrating into the cortex.

This dissertation has examined surface local field potentials, recorded at high spatiotemporal resolution by dense grids of nonpenetrating microwires, to determine whether useful information could be derived from the surface of the human cortex for BCI applications. One of the most important results of this work was to confirm that field potentials at the cortical surface contain millimeter-scale dynamics which would be averaged away with more traditional macroscale electrocorticography. Dense microelectrode grids

of the style used in this work represent an important step forward for capturing useful information from the cortical surface.

This dissertation further demonstrated that surface LFPs can support real BCI applications. The motor and speech studies described in Chapters 5 and 6 illustrate that information is present in the signal. Much of the effort in developing these applications was spent on the details of the signal processing, i.e., understanding which features were important to decode and how to appropriately process the acquired neural data to produce these features. Importantly, this work showed that information is represented across space, time, and frequency in the neural data, and that incorporating dynamics from each of these dimensions is essential to providing the highest performance in decoding brain activity.

Other aspects of BCI research were also described in this dissertation, namely techniques for low-power digital processing, and an electrical characterization of the nonpenetrating micro-electrodes. These contributions are representative of the spectrum of issues important to BCI research. In the case of electronics, BCI systems will almost certainly need to be implemented as mixed-signal VLSI integrated circuits in order to be implantable, and processing high-bandwidth data in low-power systems is a challenging area of research. In the case of electrode characterization, the relationships between tissue, electrode, and recording electronics must be well understood in order to understand how neural signals are sensed and digitized.

From electronics to signals to electrodes to applications, the work described in this dissertation represents a comprehensive investigation of surface LFPs as an interfacing medium between man and machine. This research developed through deep collaborations in both concept and practice between engineering and science. It is in this same spirit that this work will continue, with scientific and engineering advances driving the development of useful BCI systems.

Challenges and future work: subjects and data

For this work, and indeed for almost all BCI work involving intracranially-derived brain signals in the U.S. and around the world, the only available patient population is made up of people suffering from severe, medically refractory epilepsy. Because these patients already require implantation of macro-ECoG grids for diagnostic monitoring, they present an opportunity to also implant research grids, within the constraints of approval by Institutional Review Boards and informed consent of the patients themselves. Considering the difficult circumstances in which these patients find themselves, confined to hospital bed after brain surgery, it is something of an understatement to say they have been generous in agreeing to participate in this research, and their participation has been sincerely appreciated.

One challenge associated with this patient population, however, is that the full impact of epilepsy on brain function is unknown. Thus, it is entirely possible, however unlikely, that results derived from epilepsy patients will not translate directly to other subjects. Perhaps more likely is that the pathology of epilepsy might cause some remapping of cortical functional areas, or that epileptic discharges might interfere with more relevant signals recorded during experimental tasks. Where possible in this work, the data have been manually reviewed to avoid periods of inter-ictal discharge or seizure activity. Grid placement was always decided with the best information available.

There is at least one clinical trial at present in the United States exploring BCI work in paralyzed human subjects [1]. Because of regulatory overhead and other complexities, it has been an expensive but scientifically valuable endeavor. As has been the case with those clinical trials, the most directly applicable testing of BCI systems for paralyzed patients will need to occur in paralyzed patients. Despite this imperative, there is no clear path toward expanding BCI research to more relevant patient populations in more centers around the world. This issue remains one of ethics, policy, and funding, rather than technology, and will likely to continue to govern BCI research efforts for many years to come.

It is something of a contradiction that the very pathology which enables access to the research may also confound it to some degree. However, the pathology itself should not be forgotten: high-quality recordings of neural activity during pathological conditions are valuable in their own right from the perspective of studying etiology and symptomatic phenomena. In this same vein, a variety of other topics could easily be explored in parallel with these neural data, including sleep, anesthesia, effects of other medicines, interactions between cortical areas, and many other fundamental topics in neuroscience and medicine. Given the unique nature of intracranial recordings, these research programs should be conducted in a manner that maximizes the benefits derived from the neural recordings.

Often, parallel research efforts means sharing data between labs and institutions, and several challenges are immediately relevant. Patient rights, including privacy, must be protected first, regardless of the potential benefits of the research. Uses of the data must be approved by IRBs. Data formats, including the marking of experimental events and other potentially relevant metadata, can vary drastically between researchers. At times, these issues can mean the overhead to sharing data is somewhat prohibitive. However, the data are simply too valuable not to make every effort to pursue as many avenues of research as possible from each data set.

Challenges and future work: electronics

Whereas modern neural recording systems typically consist of multiple computers and technicians, the ideal BCI product should be implantable and largely self-contained. The primary vehicle for achieving such a system is integration of analog and digital circuitry in mixed-signal VLSI integrated circuits. The integration of such large systems can be challenging. Certainly, significant investment in man-hours and expense will be necessary. Further complicating the design of electronics for BCIs are the numerous tradeoffs which must be considered, such as determining how many channels to support for processing and off-chip communication while remaining within a power budget which would allow

chronically sustained operation. It is likely that making informed decisions about these issues will require more information about the signal processing which must occur for each channel and for the combined feature set.

Off-chip communications represent another significant challenge for BCI electronics. For BCI operation specifically, the only information needed on a continuous basis is that which programs the prosthetic output. However, for scientific research and for clinical validation, both of which will be essential components of this field for the foreseeable future, access to full-bandwidth data is a necessity. Actually, a system which can stream raw data from intracranially implanted electrodes will have many applications beyond BCI research, not the least of which is diagnostic monitoring for epilepsy. While a variety of options have been presented in the literature, particularly as discussed in Chapter 1, ultra low-power wireless communication of high-bandwidth data remains an open and challenging area of research.

A third challenge associated with electronics for BCI systems is that of packaging and managing physical connections to the electrodes. Packaging itself is a complicated task with many constraints like biocompatibility, longevity, and providing a good barrier between electronics and biological matter. Another specific challenge in packaging is that without any electronic signal amplification and muxing on the electrode grid itself, one wire is needed to physically connect each electrode to the analog frontend on a VLSI chip. The limited surface area available on a small VLSI chip for such connections immediately limits the number of channels such a system could support. On-grid electronics present a separate set of challenges dealing with noise and power delivery. With ever expanding needs for higher channel counts and more expansive coverage of the cortex, these kinds of challenges will continue to drive technological innovations in how electrodes connect to recording electronics, and how BCI systems are packaged.

Challenges and future work: electrodes

Because devices implanted in human subjects in the U.S. must have approval from the U.S. Food and Drug Administration, the grids used for this study had to be manufactured commercially by companies which had obtained these approvals. These commercial grids were sometimes several millimeters thick, and uniformity among electrode sites was often poor due to the application of macroscale manufacturing processes to microscale electrodes. Thickness is an important issue in intracranial electrode arrays because pressure on the cortex can constrict blood vessels and cut off blood flow to a portion of cortex. Flexibility is important because the gyri and sulci of the human neocortex together present a highly uneven surface. Uniformity among electrodes is important because, for example, differences in metal surface area can contribute to differences in the signal acquired by different electrodes within a grid. These kinds of differences can lead to some difficulties in signal processing.

While the commercial products used for this work have provided an important starting point for recording surface LFPs, significant opportunity remains in the area of manufacturing thin, flexible arrays of micro-electrodes which conform to the cortical surface. Research is needed to find materials that are thin, flexible, durable, and bio-compatible, and to determine the best manufacturing processes to ensure good uniformity among electrodes within and across grids. Physical features, such as the silicone sheath around each electrode site in some grids discussed in Chapter 4, may also play a role in improving the recording properties of the electrode grids. New electrode designs are forthcoming (e.g., [2]), but the FDA approval process can be long and expensive and it will likely be some time before they can be widely used in humans.

Challenges and future work: signal processing

Whereas relationships between neural signals and motor outputs were often assumed to be linear and static in the algorithms developed for this work, it is likely that they are in fact

nonlinear and dynamic. The dynamic nature of cortical processing suggests that parameters learned during classifier training will either need to be frequently relearned, or will need to be updated online. Adaptation is a well-studied field in engineering. The application of adaptive filtering techniques to brain-signal processing will likely have substantial impact on the performance and longevity of BCI systems. In addition to change-adaptation, these techniques may also be useful for improving scientific understanding of cortical plasticity and learning. The interplay between adaptation in the signal processing and adaptation of the brain as subjects learn to use the BCI system remains open for innovation and study.

Relationships between field potentials and motor and speech outputs are probably also nonlinear, i.e., a simple matrix transformation of one will not fully describe the other. The nature of these relationships is complicated by a number of factors, including that information is distributed across multiple dimensions in the neural signals—at least across space, time, and frequency—and that multiple distributed cortical areas are likely to be involved in complex networks of neuronal populations involved in processing stimuli and producing outputs. Until these relationships are better understood, finding and processing features in the neural data will require, at worst, some form of pseudo-blind searching whether exhaustive, Monte Carlo, or semiguided (e.g., genetic algorithms). Feature selection is one area of this work where the collaboration between neuroscientists and engineers was crucial, as the science was used to intelligently guide the engineering application to look for useful information in the brain signals. In general, however, this issue presents a substantial area of opportunity well suited to continued scientific research. Advances in this area will drive the most significant improvements in BCI performance since they will lead to properly defined models which are fundamental to the formulation of most decode and classification problems.

Conclusion

The primary contribution of this dissertation is the finding that field potentials at the cortical surface, recorded by dense grids of microelectrodes, are an attractive candidate for motor and speech BCIs. These signals may be recorded with high spatiotemporal resolution without penetrating the cortex, although implantation will require surgical access to the intracranial space. In addition to this primary contribution, methods were presented for characterizing the energy usage of VLSI digital logic, and for improving the efficiency of operating on large amounts of data within a limited power budget. A characterization of the electrical impedance of currently available, FDA-approved microwire grids was performed to better understand potential requirements for amplification and recording electronics. These collected studies as a whole represent a comprehensive exploration of surface local field potentials for BCI applications. The findings of this dissertation provide strong motivation for continued interdisciplinary work to explore the capabilities of surface LFPs for safe, chronic, and useful BCI systems.

This dissertation has been devoted to better understanding the nature of surface LFPs for BCIs, and yet many challenges and opportunities remain in almost every aspect of this field of research. BCI systems need to be explored and validated in their target population, i.e., amputees or paralyzed patients. Better electrodes are needed to increase surface area coverage and channel counts, and to improve longevity and safety. Advances in electronics are needed to support massive data throughput with small power budgets. The nature of the brain's information processing needs to be better understood so that signal processing can be designed with more intelligent feature selection and adaptation. In short, sustained progress in this field will continue to be characterized by close collaborations between science, medicine, and engineering. The techniques and findings of this dissertation, and the close working relationships formed between science, medicine, and engineering have set a foundation for this research which will lead to new and exciting technologies for safe, useful brain-computer interfaces.

References

- [1] L. R. Hochberg, M. D. Serruya, G. M. Friehs, J. A. Mukand, M. Saleh, A. H. Caplan, A. Branner, D. Chen, R. D. Penn, and J. P. Donoghue, "Neuronal ensemble control of prosthetic devices by a human with tetraplegia," *Nature*, vol. 442, pp. 164-71, Jul 2006.

- [2] J. Viventi, D.-H. Kim, L. Vigeland, E. S. Frechette, J. A. Blanco, Y.-S. Kim, A. E. Avrin, V. R. Tiruvadi, S.-W. Hwang, A. C. Vanleer, D. F. Wulsin, K. Davis, C. E. Gelber, L. Palmer, J. Van der Spiegel, J. Wu, J. Xiao, Y. Huang, D. Contreras, J. A. Rogers, and B. Litt, "Flexible, foldable, actively multiplexed, high-density electrode array for mapping brain activity in vivo," *Nat. Neurosci.*, vol. 14, pp. 1599-1605, 2011.